UNIVERSITÉ DE NEUCHÂTEL

Analysis and Improvement of the Spectral Properties in Mid-Infrared Semiconductor Quantum Cascade Lasers

Thèse présentée à la Faculté des Sciences pour l'obtention du grade de Docteur ès Sciences par:

Lionel Tombez

Ing. Dipl. EPFL en Microtechnique

acceptée le 21.01.2014 sur proposition du jury:

Prof. Thomas Südmeyer	Directeur
Prof. Jérôme Faist	Rapporteur
Dr. Saverio Bartalini	Rapporteur
Dr. Stéphane Schilt	Rapporteur

Neuchâtel, 2014

UNIVERSITÉ DE
NEUCHÂTEL

Faculté des sciences
Secrétariat-décanat de Faculté
Rue Emile-Argand 11
2000 Neuchâtel - Suisse
Tél: + 41 (0)32 718 2100
E-mail: secretariat.sciences@unine.ch

IMPRIMATUR POUR THESE DE DOCTORAT

La Faculté des sciences de l'Université de Neuchâtel autorise l'impression de la présente thèse soutenue par

Monsieur Lionel TOMBEZ

Titre:

Analysis and Improvements of the Spectral Properties in Mid-Infrared Semiconductor Quantum Cascade Lasers

sur le rapport des membres du jury composé comme suit :

- Prof. Thomas Südmeyer, Université de Neuchâtel, directeur de thèse
- Dr. Stéphane Schilt, Université de Neuchâtel
- Prof. Jérôme Faist, ETH Zürich
- Dr Saverio Bartalini, LENS, Université de Florence, Italie

Neuchâtel, le 20 février 2014

Le Doyen, Prof. P. Kropf

Keywords - Mots clés

Keywords

semiconductor, quantum cascade, lasers, intersubband transitions, mid-infrared, mid-IR, distributed feedback, DFB, single mode, linewidth, flicker, $1/f$, frequency noise, phase noise, frequency stability, electronic noise, active stabilization, low noise, noise reduction, frequency modulation, thermal dynamics

Mots clés

semiconducteur, cascade quantique, lasers, transition intersousbande, infrarouge moyen, réseau de Bragg distribué, DFB, mono mode, largeur de raie, flicker, $1/f$, bruit de fréquence, bruit de phase, stabilité de fréquence, bruit éléctronique, stabilisation active, réduction de bruit, faible bruit, modulation de fréquence, dynamique thermique

Abstract

Quantum Cascade Lasers (QCLs) are semiconductor lasers based on intersubband transitions in semiconductor heterojunctions. Unlike conventional laser diodes, the emission wavelength of QCLs is not defined by the energy gap between the conduction and valance bands of the semiconductor material, but by the energy spacing between the discrete states of quantum wells, which enables the realization of compact semiconductor lasers in the mid-infrared and far-infrared spectral regions. The mid-IR spectral region contains the fundamental vibration bands of many molecular species, such as carbon dioxide (CO_2) and methane (CH_4), and enables high precision analysis of chemical species. Thanks to the use of well-known semiconductor fabrication techniques widely developed for optical telecommunication applications in the near-IR, QCLs are compact and suitable for mass-production, and therefore constitute a very interesting candidate for the development of portable and highly sensitive and selective trace-gas sensors by absorption spectroscopy in the mid-infrared.

In this thesis, the spectral properties of InGaAs/InAlAs distributed-feedback (DFB) QCLs emitting in the mid-IR spectral region were studied, with the aim of assessing and improving the spectral purity of these devices. Low frequency-noise and narrow-linewidth coherent light sources emitting in the mid-IR spectral region are indeed of prime interest for the future development of high-resolution spectroscopy systems. First of all, this thesis presents the frequency-tuning and thermal dynamics in DFB-QCLs, which are important to understand the underlying mechanisms of frequency noise generation. A simple thermal model is used to explain the observed thermal dynamics. In a second phase, the frequency-noise properties of different QCLs were studied upon operating conditions and devices parameters. The effect of the processing of the lasers active region, namely in ridge waveguide or buried-heterostructure was in particular investigated. The design of a low-noise power supply to provide a stable injection current as well as the impact on the spectral properties of QCLs is also presented.

Then, the noise properties at the electrical level in the semiconductor laser chips were investigated. A particularly interesting outcome of the experiments is a clear link between instabilities of the emission frequency and electrical power fluctuations due to the electronic transport in the laser chip. The results enabled the demonstration of a novel and extremely simple method for assessing the spectral properties of QCLs from electrical measurements only. Finally, a novel and innovative active method for frequency-noise reduction and linewidth narrowing of QCLs without using any optical frequency reference was developed and yielded a 90% reduction of the frequency-noise power spectral density.

Résumé

Les lasers à cascade quantique (QCL) sont des lasers à semiconducteur basés sur des transitions inter-sous-bandes. Au contraire des diodes lasers traditionnelles, la longueur d'onde d'émission de ce type de laser n'est pas définie par la bande interdite (bandgap) du matériau semiconducteur, mais par l'écart d'énergie entre les niveaux discrets de plusieurs puits quantiques, ce qui permet la réalisation de sources laser compactes émettant dans l'infrarouge moyen (mid-IR) et dans l'infrarouge lointain (far-IR). Le moyen infrarouge comporte les bandes fondamentales de vibrations d'un grand nombre d'espèces moléculaires telles que le dioxide de carbone (CO_2) ou le méthane (CH_4), et permet la détection d'éspèces chimiques avec grande précision. Grâce à l'utilisation de techniques de fabrication standards et bien connues des lasers à semiconducteur utilisés pour les télécommunications optiques dans l'infrarouge proche, le laser à cascade quantique est un dispositif extrêmement compact et productible en masse, et constitue par conséquence un excellent candidat pour la réalisation de capteurs de gaz portables et extrêmement sensibles utilisant des techniques de spectroscopie par absorption dans le moyen infrarouge.

Dans cette thèse, les propriétés spectrales des lasers à cascade quantique à base d'InGaAs/InAlAs émettant dans l'infrarouge moyen et utilisant un réseau de Bragg distribué pour garantir une émission mono-mode ont été étudiées, avec pour but d'en évaluer et d'en améliorer la pureté spectrale. Les sources de lumière cohérentes à largeur de raie étroite et faible bruit de fréquence sont en effet d'une grande importance pour le dévelopement de nouveau systèmes de mesure et d'instruments de haute précision dans la gamme spectrale du moyen infrarouge. Dans un premier temps, la dynamique de l'ajustement de la fréquence optique et des propriétés thermiques des lasers à cascade quantique, qui est essentielle à la compréhension du mécanisme de formation des instabilités de fréquence, a été étudiée et est présentée. Dans un deuxième temps, l'impact des conditions d'opération et de divers paramètres des lasers à cascade quantique

sur leur bruit de fréquence a été évalué. L'impact du type de fabrication de la région active des lasers a notamment été étudié. Pour ce faire, une alimentation à faible bruit de courant a dû être développée afin de fournir un courant d'injection aussi stable que possible. Le bruit électrique dans les lasers à cascade quantique a également été étudié, et nous montrons un lien particulièrement intéressant entre les instabilités de fréquence du laser et les fluctuations de la puissance électrique dissipée dans ce dernier. Ces résultats ont permis la démonstration d'une nouvelle approche particulièrement simple visant à évaluer la pureté spectrale des lasers à cascade quantique à partir uniquement de mesures électriques. Finalement, une nouvelle méthode innovante de réduction active du bruit de fréquence et de diminution de la largeur de raie sans avoir recours à aucune référence de fréquence optique a été développée dans le cadre de cette thèse et a permis d'obtenir une réduction de 90% de la densité spectrale de puissance du bruit de fréquence.

Contents

List of Figures

List of Tables

Publications

Parts of this thesis are published in the following journal papers, book chapters and conference proceedings.

Journal publications

1. L. Tombez, S. Schilt, D. Hofstetter, T. Südmeyer, "Active frequency-noise reduction of a mid-IR quantum cascade laser without optical frequency reference", Opt. Letters 38, 5079-5082 (2013)

2. L. Tombez, F. Cappelli, S. Bartalini, S. Schilt, G. Di Domenico, D. Hofstetter, "Wavelength-tuning and thermal dynamics in continuous-wave mid-infrared quantum cascade lasers", Applied Physics Letters 103(3), 031111-031111 (2013)

3. L. Tombez, S. Schilt, J. Di Francesco, T. Fhrer, B. Rein, T. Walther, G. Di Domenico, D. Hofstetter, P. Thomann, "Linewidth of a quantum cascade laser assessed from its frequency noise and impact of the current driver", Applied Physics B, 109(3), 407-414 (2012)

4. L. Tombez, S. Schilt, J. Di Francesco, P. Thomann, D. Hofstetter, "Temperature dependence of the frequency noise in a mid-IR DFB quantum cascade laser from cryogenic to room temperature", Opt. Express 20 (7), 6851-6859 (2012)

5. S. Schilt, N. Bucalovic, L. Tombez, V. Dolgovskiy, C. Schori, G. Di Domenico, M. Zaffalon, P. Thomann, "Frequency discriminators for the characterization of narrow-spectrum heterodyne beat signals: application to the measurement of a sub-hertz carrier-envelope-offset beat in an optical frequency comb", Rev. Scient. Instr. 82 (12), 123116 (2011)

6. L. Tombez, J. Di Francesco, S. Schilt, G. Di Domenico, J. Faist, P. Thomann, D. Hofstetter, "Frequency noise of free-running 4.6 μm distributed feedback quantum cascade lasers near room temperature", Opt. Letters 36 (16), 31093111 (2011)

Book chapter

1. S. Schilt, L. Tombez, G. Di Domenico, D. Hofstetter, "Frequency Noise and Linewidth of Mid-infrared Continuous Wave Quantum Cascade Lasers: An Overview", in The Wonders of Nanotechnology: Quantum and Optoelectronic Devices and Applications, SPIE Press, Bellingham, WA, pp. 261-287 (2013)

Selected conference presentations

1. L. Tombez, S. Schilt, G. Di Domenico, D. Hofstetter, T. Südmeyer, "Active linewidth narrowing of a mid-IR quantum cascade laser without optical frequency reference", Mid-Infrared Coherent Sources, Paris, France, Oct. 26 - Nov. 1, 2013, oral MTh4B.3

2. L. Tombez, S. Schilt, G. Di Domenico, S. Blaser, A. Muller, T. Gresch, B. Hinkov, M. Beck, J. Faist, D. Hofstetter, "Physical Origin of Frequency Noise and Linewidth in Mid-IR DFB Quantum Cascade Lasers", CLEO-2013, San Jose, USA; June 9-14, 2013, oral CM1K.3

3. L. Tombez, S. Schilt, J. Di Francesco, D. Hofstetter, "Frequency noise of free-running mid-IR DFB quantum cascade lasers", IQCLSW-2012, Vienna, Austria; September 2-6, 2012, oral presentation

4. L. Tombez, S. Schilt, J. Di Francesco, P. Thomann, D. Hofstetter, "Temperature dependence of the frequency noise and linewidth of a DFB quantum cascade laser", CLEO-2012, San Jose, USA; May 6-11, 2012, oral CF2K.5

5. L. Tombez, J. Di Francesco, S. Schilt, G. Di Domenico, D. Hofstetter, P. Thomann , "Frequency noise of free-running room temperature quantum cascade lasers", CLEO-Europe 2011, Munich, Germany; May 22-26, 2011, oral CB4.3 TUE

6. L. Tombez, J. Di Francesco, S. Schilt, G. Di Domenico, D. Hofstetter , P. Thomann, "Frequency noise of free-running room temperature CW quantum cascade lasers", 40th Freiburg Infrared Colloquium, Freiburg, Germany, February 17-18, 2011, oral presentation

7. L. Tombez, J. Di Francesco, S. Schilt, G. Di Domenico, D. Hofstetter, P. Thomann, "Low-noise room temperature quantum cascade lasers", Optical Clock Workshop, Torino, Italy, December 1-3, 2010, oral presentation

Chapter 1

Introduction

Would you expect a portable, inexpensive and widespread device such as a cell phone to be capable of performing medical diagnostics, testing whether food is safe for human consumption, or monitoring air quality? It would undoubtedly better fit in a bad sci-fi movie. However, the tremendous developments in quantum optics of the last decades could very well move such futuristic applications closer to a not-so-distant reality.

The advent of quantum mechanics combined to the technological developments in semiconductor fabrication techniques have allowed scientists to play with electrons and photons at the scale of the atom, and develop revolutionary nanostructures aiming at overcoming physical boundaries. The emergence of semiconductor lasers emitting in the mid-infrared (mid-IR) spectral region cannot better illustrate the foregoing statements. Recent advances in quantum optics enabled the development of compact and efficient coherent light sources in this portion of the electromagnetic spectrum.

The mid-IR spectral region of the optical spectrum extends from wavelengths of 2 µm up to 30 µm, and is also often referred to as the molecular fingerprint region. This latter designation reveals of lot about its importance in numerous different application fields. Indeed, a countless number of molecular species, among them molecules attracting very high media coverage such as carbon dioxide (CO_2), have their fundamental vibrational resonance bands in this spectral region. The exact location of these resonances in the spectrum as well as their strengths depend on the constituents and amount of molecules in a given sample, and are governed by quantum mechanics selection rules. Mid-IR radiation can therefore be used to probe these molecular resonances and record absorption spectra, which are literally the fingerprints of the molecules and can be compared to reference data

in order to establish whether a particular molecular specie is present in an unknown sample, and quantify its concentration. The ability to identify and quantify low levels of specific chemical compounds in the air opens the way to an infinite number of potential real-world applications. Air quality and greenhouse gases monitoring, detection of toxic agents and explosives, and exhaled air analysis for medical diagnostics are only a few examples of applications that have the potential to transform environmental sciences and modern medicine.

However, the realization of robust, efficient and compact laser sources at mid-IR wavelengths has been challenging and it is only since the advent of the quantum cascade laser (QCL), which was demonstrated for the first time at AT&T Bell Labs in 1994 [1] that the development of highly sensitive and portable chemical sensor has emerged. Unlike conventional semiconductor laser diodes, quantum cascade lasers are semiconductor lasers based on intersubband transitions and do not rely on electron-hole recombination between the conduction and valence bands. In interband transitions, the energy of the emitted photons $E = h\nu$, depends on the gap between these two energy bands. The composition of the semiconductor compounds defines the energy bandgap, and therefore the emission wavelenghts -or color- of the laser. In intersubband transitions, the picture is fundamentally different and the transition takes place in the conduction band itself, between two discrete energy levels of a quantum well. Quantum wells are nanostructures made of extremely thin layers of semiconductor materials, as shown in Figure 1.1, in which electrons can be confined.

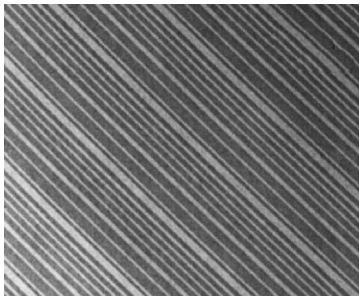

Figure 1.1: Periodic nanostructure of thin layers of two different semiconductor materials enabling quantum confinement effects. The narrowest layers measure 1 nm, or one billionth of a meter. Image from [2].

The first important implication is that the emission frequency does not rely any more on the bandgap of the material, but is instead defined by the physical thickness of the layers. With such transitions, it is therefore

possible to overcome the bandgap limitation and precisely design the emission of quantum cascade lasers for different mid-IR wavelengths in a same material system using quantum effects.

Since the first demonstration of a QCL in 1994, which was carried out in pulsed mode and at cryogenic temperature, tremendous advances were achieved and devices operating in continuous wave at room-temperature are nowadays commercially available. This evolution was made possible notably through several key achievement such as the demonstration in 1996 of room-temperature operation in pulsed mode [3], single-mode operation in 1997 [4, 5] and of the first continuous-wave QCL working at room-temperature in 2002 [6]. Since then, relatively low electrical power consumption below 1 W [7] as well as high-power QCLs with optical powers beyond 4 W at 4.6 μm [8] were more recently disclosed.

Despite all these important advances, the spectral properties of QCLs were not extensively investigated and the focus was mostly directed towards improving the efficiency, lowering threshold currents and electrical power consumptions, and extending the wavelength coverage. This is even more true compared to interband semiconductor lasers emitting in the near-infrared and visible spectral regions, for which spectral properties were deeply explored and many narrow-linewidth systems demonstrated. Whereas the width of molecular resonances in the mid-IR is of a few gigahertz at atmospheric pressure, high spectral purity light sources are of prime interest in the field of high-resolution spectroscopy in order to follow the tracks of precision optical metrology, which was mainly developed in the visible and near-infrared spectral regions. Moreover, the potential development of high-speed free-space coherent communication systems using mid-IR QCLs in the so-called atmospheric windows (3-5 μm and 8-14 μm) as well as the future development in solid-state optical frequency comb would very likely benefit from low-noise mid-IR lasers.

The work carried out in this thesis unifies two research fields having strong ties in the scientific landscape of Neuchâtel, namely frequency-metrology and mid-IR quantum cascade lasers. The work encompassed the study of the performance of InGaAs/InAlAs mid-IR QCLs as frequency-stable light sources in the mid-IR spectral region, the study of the noise generation mechanisms and the development of compact active noise-reduction techniques.

This thesis is organized as follows. First of all, a general introduction on the fundamental concepts of QCLs and optical frequency metrology is presented in Chapter 2.

In Chapter 3, the wavelength-tuning and temperature dynamics in QCL chips were investigated and a thermal model was developed and validated. The thermal dynamics are of prime importance for the study of frequency-noise generation processes in QCLs and the results will be used in the following chapters.

In Chapter 4, the spectral purity of mid-IR QCLs emitting at 4.6 μm was investigated using absorption spectroscopy. We reported at that time the lowest frequency-noise and narrowest linewidth of 550 kHz of a free-running QCL in the 4-5 μm range, while operating the device at room-temperature. To achieve these results, low-noise electronics were developed to drive the lasers and are presented in this chapter. Despite the challenging design due to the high voltage required to bias QCLs, very low current-noise levels were achieved, and remain state-of-the-art today. The impact of the driving electronics upon the spectral properties of mid-IR QCLs was also studied in detail, and we show that great care must be taken if narrow-linewidth emission is desired.

Chapter 5 presents the impact of QCLs designs and operating parameters upon the frequency-noise. Different QCLs using either ridge waveguides or buried-heterostructures were characterized, across a range of structural design parameters. A particularly interesting dependence of the frequency noise over temperature was found in buried-heterostructure QCLs at 4.6 μm and a clear correlation between frequency noise and electrical noise measured directly across the devices was shown. The origin of frequency-instabilities was linked to electrical-power fluctuations in the laser active region. These findings have led to the demonstration of a novel and simple method to assess the spectral properties of QCLs from electrical noise measurements only, which are much more convenient and simpler to implement than optical frequency measurements. The origin of electronic fluctuations will be discussed in this chapter as well.

In Chapter 6, a novel active method for frequency-noise reduction is presented. While an optical frequency-reference is generally required, we demonstrated a linewidth-narrowing technique implemented without measuring the actual laser frequency. The developed scheme employs only the voltage-noise measured across the QCL to generate a correction signal that is fed back to the laser temperature at a fast rate, independently of the injection current. In these conditions, the fluctuations of the optical frequency were reduced by 90% in terms of frequency-noise power spectral density. The scheme has the potential to be completely integrated and could possibly also be applied to other kinds of semiconductor lasers.

Chapter 2

Basics of mid-IR technologies and noise in laser diodes

First of all, this chapter presents an overview of the importance of the mid-infrared (mid-IR) as well as the advances and developments of coherent light sources in this spectral region. Many chemical molecular species that are important in environmental and life sciences have their fundamental vibration bands in the mid-IR spectral region ($\lambda = 2-30$ μm) of the optical spectrum [9]. These strong vibrational resonances allow the realization of chemical analysis of many molecular compounds with extremely high sensitivity and selectivity, provided that coherent and tunable light sources are available in this spectral region.

In a second phase, the fundamentals of phase noise in laser oscillators are presented, including a theoretical basis, an overview of frequency-noise in semiconductor laser diodes, spectral purity characterization techniques, and $1/f$-like noise in physical systems.

2.1 Mid-IR technologies

2.1.1 Mid-IR coherent light sources

Several technologies have been developed to reach the mid-IR region of the optical spectrum. For instance, the operation of a CO_2 gas laser at 10 μm was demonstrated for the first time in 1964 [10].

Regarding low-energy bandgap semiconductors, lead-salt (PbS, PbTe, PbSe) based laser diodes emitting in the 3−30 μm range have been available since the 1960s [11]. However, this kind of mid-IR lasers suffers from limited output power (hundreds of μW), complicated manufacturing process and cryogenic temperature operation. Interband antimonide laser diodes emitting up to 3 μm at room-temperature were also demonstrated [12, 13] as well as interband cascade lasers (ICL) [14, 15] up to 5.6 μm [16].

Alternatively, generation of mid-IR light through non-linear processes based on difference frequency generation (DFG) [17] and optical parametric oscillators (OPOs) tunable from 3.6 to 4.3 μm [18] and 5.5 to 9.3 μm [19] have been demonstrated as well. Although DFG systems can be relatively compact, only limited mid-IR output power can be achieved. On the other hand, OPOs can deliver much higher output powers but are generally large systems with high power consumptions.

2.1.2 Quantum cascade lasers

Quantum cascade lasers are unipolar semiconductor devices based on intersubband transitions, relying on the idea of light amplification in heterostructures proposed in the early 70's [20], and were experimentally demonstrated for the first at Bell Labs in 1994 [1]. In contrast to conventional semiconductor laser diodes, the fundamental mechanism of light emission in intersubband lasers is not based on electron-hole recombinations between the conduction and valance bands of the gain medium, but on the transitions of electrons between discrete states in well-designed quantum wells. Both schemes are compared in Figure 2.1.

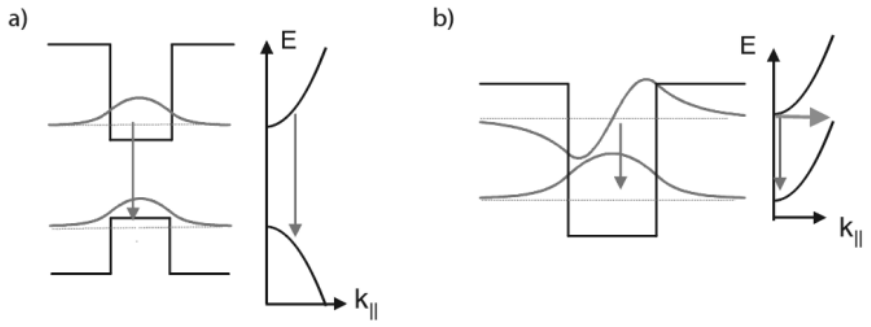

Figure 2.1: (a) Interband transition: recombination of electron-hole pairs. (b) Intersubband transition between two discrete states of a quantum well in the conduction band itself. Reprinted from [21].

A first crucial implication is that the emission wavelength in QCLs is not any more defined by the energy gap of the semiconductor materials, sometimes referred to as "the bandgap slavery". Indeed by engineering the wave functions of the quantum wells, which basically depend on the layers thicknesses, it is possible to precisely tailor the emission wavelength of QCLs and to reach longer values in the mid-IR and even the THz domain [22]. Another interesting aspect of intersubband transitions is that they can be almost naturally cascaded, which enables the electrons to be recycled and improves the quantum efficiency of such devices.

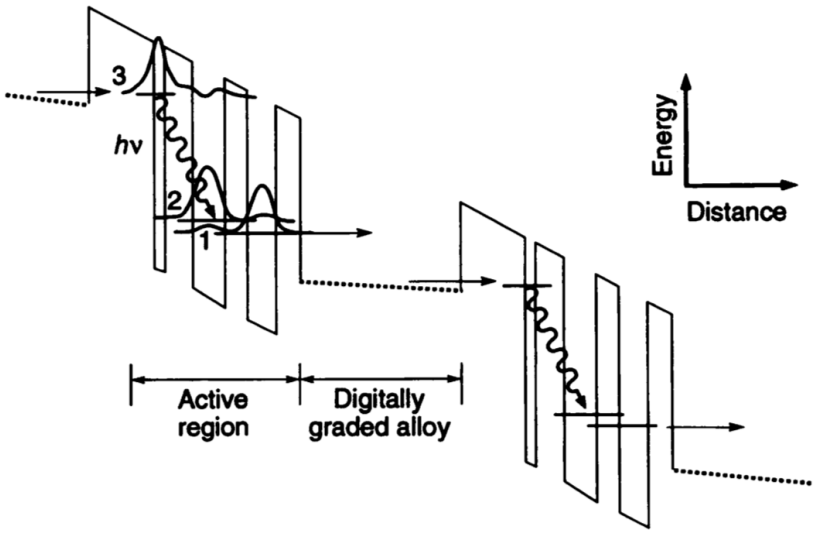

Figure 2.2: Active region design employed for the first demonstration of a QCL in 1994 [1].

An example of a typical QCL period is shown in Figure 2.2. It consists of an injector region, and an active region composed in this particular case of three quantum wells. This design results in a three-level laser system which enables an efficient population inversion between the states defining the laser transition $3 \rightarrow 2$. The spacing of the lower subbands is generally designed so that the $2 \rightarrow 1$ transition matches the energy of the longitudinal optical (LO) phonon energy and enables a fast relaxation of the lower laser level by resonant scattering to the following period. QCLs are generally composed of $\approx 25 - 40$ cascaded periods shown in Figure 2.2.

Since the first QCL demonstration, several key innovations such as the achievement of laser operation above room-temperature in pulsed mode [3], of the bound-to-continuum [23] and two-phonons resonant designs [24], and finally of continuous-wave (CW) operation at room temperature [6] have

led to a fast development of the performances of these devices in terms of wavelength coverage, output power and electrical consumption. For instance, mid-IR QCLs operating at electrical power consumptions below 1 W [7] and high optical output powers beyond 4 W in CW have been recently demonstrated [8].

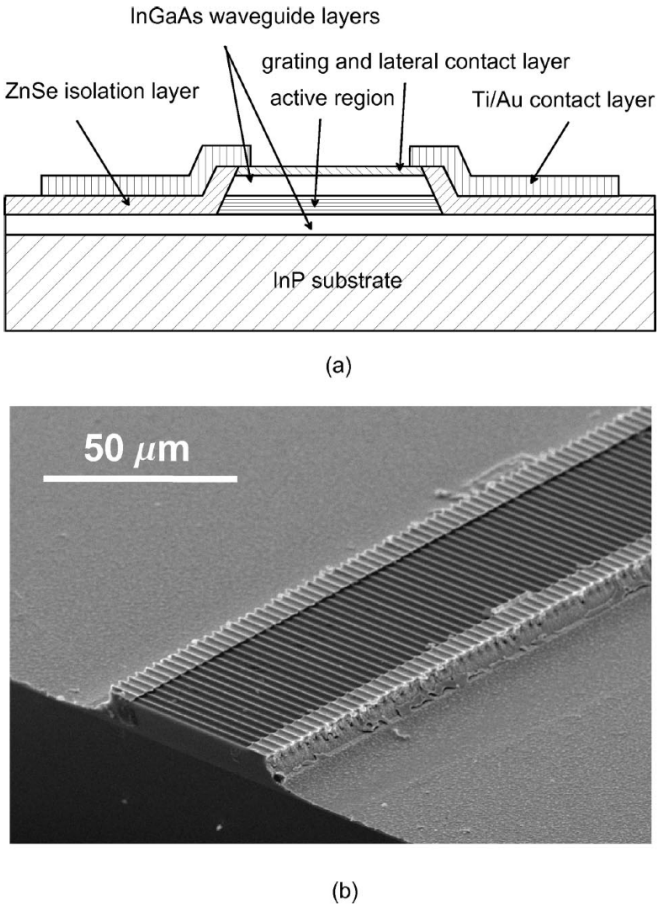

Figure 2.3: (a) Schematic cross-section of a ridge-waveguide QCL. (b) Scanning electron micrograph (SEM) of the distributed-feedback grating etched on top of the device [25].

Another key advance in the field of QCLs was the development of tunable single-frequency devices, especially required in the field of molecular spectroscopy. The first realization of single-frequency QCLs was achieved using a distributed-feedback grating (DFB) etched on top of the device [4] and also directly on top of the active region, before the regrowth of a cladding layer [5]. Other single-frequency QCLs were then demonstrated at

different wavelengths [25, 26]. The processing of QCLs with DFB gratings is illustrated in Figure 2.3 (a). Figure 2.3 (b) shows an image of the DFB grating of the QCL of Ref. [25] ($\lambda = 10$ µm) obtained by scanning electron microscopy (SEM). In such a configuration, the distributed-feedback grating acts as an optical filter inducing wavelength-dependent losses in the laser cavity and forces laser operation at a single wavelength, despite the relatively broad gain curve. The lasing wavelength is defined by the Bragg condition:

$$\lambda_B = \frac{2n_{eff}\Lambda}{N} \tag{2.1}$$

where n_{eff} is the effective refractive index, Λ the grating period, and N the order of the grating (integer value). Although the detailed analysis will not be presented here, the coupled-wave theory of distributed-feedback lasers can be found in Ref. [27].

Single-frequency operation of QCLs in extended cavity configuration using external gratings was demonstrated for the first time in 2001 up to 230 K [28], and then in various configurations both in pulsed and CW regimes [29–31]. The main advantage of the external cavity configuration lies in a broader tuning range than DFB QCLs, at the expense of the size of the device. Based on a heterogenous cascade, a tuning range of up to 24% of the central wavelength was obtained [32].

2.1.3 Applications

The mid-infrared (mid-IR) region of the electromagnetic spectrum, also referred to as the fingerprint region, ranges from wavelengths of 2 to 30 µm and is of prime interest for several applications such as chemical sensing and monitoring of atmospheric constituents. Many chemical species such as carbon-dioxide (CO_2), carbon-monoxide (CO), methane (CH_4), ammonia (NH_3) and nitrogen-oxide compounds (NO_x) show strong vibrational molecular resonances in this spectral region [33], which makes mid-IR absorption spectroscopy a very efficient technique for sensitive and selective chemical analysis and trace-gas sensing.

Absorption spectroscopy relies on Beer-Lambert law, which states that the intensity of light $I(\nu)$ at a frequency ν transmitted through a sample of concentration C and absorbance $\alpha(\nu)$ over a distance L, compared to the initial intensity I_0, is given by Eq. 2.2.

$$I(\nu) = I_0 e^{-\alpha(\nu)CL} \tag{2.2}$$

As the absorbance is characteristic of the chemical compounds, the ratio $I(\nu)/I_0$ as a function of ν gives a quantitative and qualitative information about the concentration and composition of the sample. Figure 2.4 shows the transmission spectra of carbon dioxide and methane around 2.7 µm and 3.3 µm, respectively. These features are governed by quantum mechanics selection rules and constitute the fingerprints of molecules.

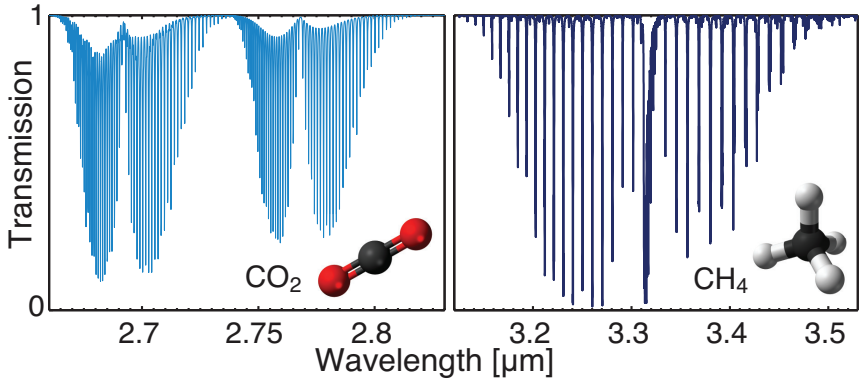

Figure 2.4: Transmission spectra of carbon dioxide (CO_2) and methane (CH_4) in the mid-IR spectral region, which are the equivalent of the fingerprints of molecules.

The advent of QCLs has triggered the development of many absorption spectroscopy techniques and the demonstration of trace-gas sensing with unprecedented precision. Noise-reduction techniques such as wavelength modulation spectroscopy (WMS) [34] and frequency modulation spectroscopy (FMS) [33] as well as signal enhancement methods such as cavity ring-down spectroscopy [35] and quartz-enhanced photoacoustic spectroscopy (QEPAS) [36] have been implemented.

Such systems have been deployed to quantify the concentrations of many of the most important atmospheric greenhouse gases, including carbon dioxide (CO_2) and methane (CH_4) with sensitivities as low as 0.1% of the ambient concentrations [37]. In life sciences, the development of trace-gas sensors for the analysis of exhaled chemical compounds brings promising perspectives for novel and fast medical diagnostics [38]. For instance, ammonia (NH_3) in human breath was studied as a marker for kidney and liver function [39], while carbon-monoxide (CO) could be used for the detection of cardiovascular diseases and diabetes. In both cases,

the exhaled levels of gases are in the sub-ppm range and very sensitive sensors have been developed with detection limits as low as 50 ppb for ammonia [40] and 200 ppb for CO [41].

The advent of optical frequency combs (OFC) enabled high resolution spectroscopy experiments by referencing mid-IR radiation of QCLs to frequency standards [42, 43] and the measurement of radiocarbon (^{14}C) down to parts per trillion (ppt) was achieved at 4.5 µm [44].

Beside spectroscopy applications, mid-IR quantum cascade lasers might be used for optical communications. The atmosphere contains indeed two transmission windows between 3-5 µm and 8-14 µm showing low absorption, and which could be used for free-space data transfers. A few experiments were performed and showed the feasibility of high data rates links based on mid-IR QCLs [45–48].

2.2 Spectral purity of semiconductor lasers

2.2.1 Frequency-noise in semiconductor lasers

The spectral properties of a laser are commonly described by its linewidth, i.e. the full width at half maximum (FWHM) of the optical lineshape. The linewidth of a laser can be experimentally determined from the heterodyne beat with a reference laser source or by self-homodyne/heterodyne interferometry using a long optical delay line [49]. The linewidth is a single parameter widely used to characterize the laser spectral properties, as it allows a simple and straightforward benchmark between different laser sources. However, this specific parameter gives an incomplete picture of the actual frequency stability. In particular, it contains poor information about the spectral distribution of the noise. This is in contrast to the power spectral density (PSD) of the laser frequency fluctuations, which gives a complete picture of the laser frequency noise, showing how the different noise spectral components contribute to the laser linewidth.

The measurement of the frequency noise requires an optical frequency discriminator to convert the laser frequency fluctuations into intensity fluctuations that can be measured with a photodiode. An optical frequency discriminator can be seen as a filter with frequency-dependent transmission in a restricted frequency range, such as a gas-filled cell near an atomic/molecular resonance (Doppler-broadened [50–52] or sub-Doppler [53]), a Fabry-Perot resonator or an unbalanced two-beam interferometer.

As an alternative, the frequency-noise of the beat signal can be measured in the RF domain as well, using RF frequency discriminators [54].

In semiconductor lasers, the frequency-noise spectrum is generally split into two distinct regimes. The ultimate frequency-noise limit achievable in lasers is given by a white frequency-noise floor leading to the intrinsic linewidth, or Schawlow-Townes linewidth, and is due to quantum noise (spontaneous emission) in the gain medium of the laser oscillator. While this fundamental limit can be relatively narrow, the frequency-noise spectrum in real semiconductor lasers is generally governed by excess $1/f$ fluctuations at low frequency that exceed the white noise floor and broaden the emission linewidth at reasonable observation times. Both Schawlow-Townes linewidth and $1/f$ noise in physical systems will be introduced later in this chapter.

2.2.2 Schawlow-Townes linewidth

The intrinsic linewidth, or Schawlow-Townes linewidth $\Delta\nu_{ST}$ represents the ultimate spectral width of a laser oscillator, limited by quantum noise due to spontaneous emission in the resonator gain. The relation can be written as [55, 56]:

$$\Delta\nu_{ST} = \frac{2\pi h\nu_0 \mu (\Delta\nu_{cav})^2}{P} \tag{2.3}$$

where hv_0 is the photon energy, $\mu = N_2/(N_2 - N_1)$ describes the population inversion, $\Delta\nu_{cav}$ is the FWHM linewidth of the passive resonator, and P the output optical power. The intrinsic linewidth $\Delta\nu_{ST}$ of a laser oscillator can therefore be orders of magnitude narrower than the FWHM linewidth of the resonator $\Delta\nu_{cav}$. The intrinsic linewidth of an helium-neon (He-Ne) gas laser at 633 nm with a passive resonator linewidth of 8 MHz and 1 mW output power can be calculated to be narrower than 1 Hz [57].

The expression of the intrinsic linewidth was rewritten by Henry [58,59] for semiconductor lasers in order to take into account the dependence of the refractive index upon the carrier density in semiconductor materials. The intrinsic linewidth of semiconductor lasers is basically enhanced by a factor $(1+\alpha_H)^2$, where α_H is known as the linewidth enhancement factor. These aspects will be discussed in more details in Chapters 3 and 4.

Finally, it is extremely important to highlight the fact that, as stated before, the Schawlow-Townes linewidth represents a fundamental limit and

is most often not reached in real laser systems, which are exposed to additional external perturbations. This is specially the case in semiconductor lasers for which the emission linewidth is broadened by low-frequency $1/f$ fluctuations (see [60, 61] and Chapters 4-5).

2.2.3 Frequency-noise to optical lineshape relation

From the frequency noise PSD, the laser lineshape and the linewidth may be retrieved, but the reverse process (i.e. determining the exact frequency noise spectrum from the lineshape) is not possible. However, the exact determination of the linewidth from the frequency noise spectral density is not always straightforward. This problem has been theoretically addressed for a long time [62–65] and involves a two-step integration procedure as detailed in [56, 62, 66]. The first step consists in calculating the auto-correlation function of the electrical field $\Gamma_E(\tau)$ as an exponential of the integral of the frequency noise PSD $S_{\delta\nu}(f)$ filtered by a sinc^2 function [62]:

$$\Gamma_E(\tau) = E_0^2 e^{i2\pi\nu_0\tau} e^{-2\int_0^\infty S_{\delta\nu}(f)\frac{\sin^2(\pi f\tau)}{f^2}\mathrm{d}f} \tag{2.4}$$

Then, the optical spectrum $S_E(\nu)$ is obtained by Fourier transform of the auto-correlation function $\Gamma_E(\tau)$:

$$S_E(\nu) = 2\int_{-\infty}^{\infty} e^{-i2\pi\nu\tau}\Gamma_E(\tau)\mathrm{d}\tau \tag{2.5}$$

However, only the ideal case of a pure white frequency noise $S_{\delta\nu}^0$ can be analytically solved [63] and yields a Lorentzian lineshape with an FWHM linewidth:

$$\Delta\nu_{\mathrm{FWHM}} = \pi S_{\delta\nu}^0 \tag{2.6}$$

This case corresponds for instance to the well-known lorentzian lineshape described by the Schawlow-Townes linewidth in Eq. 2.3 [55,59]. In all other cases, including real laser frequency noise spectra encountered in practice, the calculation must be performed by numerical integration.

A simple approximation to determine the linewidth of a laser from an arbitrary frequency noise spectrum was demonstrated in Ref. [66]. It was

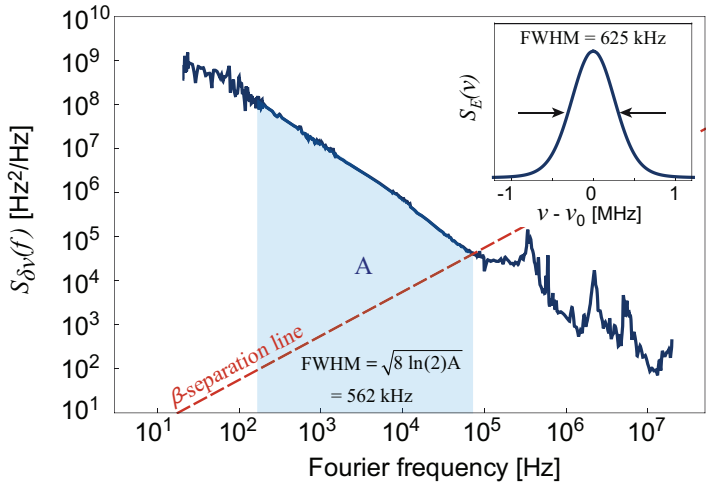

Figure 2.5: Evaluation of the FWHM linewidth from the frequency-noise power spectral density (PSD) of a 4.6 µm QCL using the formalism of Ref. [66]. Inset: laser lineshape obtained through the two-step integration of the experimental frequency-noise PSD.

shown how the frequency noise PSD $S_{\delta\nu}(f)$ can be geometrically separated into slow and fast modulation areas by a single line displayed in Figure 2.5, referred to as the β-separation line, defined as $S_{\beta-line}(f) \approx 0.56f$. Frequency noise in these two areas has a completely different impact on the laser lineshape. Only the slow modulation area, for which $S_{\delta\nu}(f) > S_{\beta-line}(f)$, contributes to the linewidth of the signal. The fast modulation area $S_{\delta\nu}(f) < S_{\beta-line}(f)$ only affects the wings of the lineshape, without contributing to the FWHM linewidth. As a result, the linewidth $\Delta\nu$ can be approximated with a good accuracy (better than 10%) from the integral A of the slow modulation area as introduced in Ref. [66]:

$$\Delta\nu = \sqrt{8\ln(2)A} \tag{2.7}$$

The surface A corresponds to the area under the frequency noise PSD obtained for all Fourier frequencies for which $S_{\delta\nu}(f)$ exceeds the β-line as shown in Figure 2.5. A low-frequency cut-off f_c has to be introduced, which represents the inverse of the observation time τ_0 in which the linewidth is measured ($f_c = 1/\tau_0$), when the frequency noise PSD is affected by $1/f$ noise (A diverges when $f_c \to 0$). Moreover, this observation also shows that the linewidth of lasers broadened by $1/f$ noise depends on the observation time. A linewidth should therefore always be specified with the considered observation time. However, while the observation time has an important

impact when its value is close to the inverse of the crossing point of the frequency-noise PSD with the β-line, the linewidth only slowly diverges and can almost be considered as constant for observation times in the 0.1-10 s range for frequency-noise PSD of typical free-running semiconductor lasers. This formalism was demonstrated to yield a good accuracy of the calculated linewidth with different laser systems [67] and will be used many times along this thesis in order to estimate QCL linewidths from frequency-noise measurements.

2.3 $1/f$ fluctuations in physical systems

$1/f$ noise, also sometimes referred to as flicker noise, or pink noise, describes a stochastic process in which the power spectral density $S(f)$ follows a power law in the form:

$$S(f) = \frac{Constant}{f^{\alpha}} \tag{2.8}$$

where f is the frequency and α generally takes a value comprised between 0.5 and 1.5. In other words, such noise phenomena are characterized by equally distributed fluctuations of relatively high magnitude at low-frequencies, or long time scales, and small fluctuations at higher frequencies, or short time scales. This behavior is illustrated in Figure 2.6, which shows the power spectral density of fluctuations characterized by a dependence in $1/f^{\alpha}$ ($\alpha = 1$ in this case).

$1/f$ noise is often associated to semiconductors where it plays an important role on the performances of electronic devices. However, since the first observation of $1/f$ fluctuations in vacuum tubes by Johnson during the 30's [68, 69], it is interesting to point out that this form of fluctuations was reported in many physical systems. It is for instance the case in geophysical systems, where $1/f$-like power spectra were reported for undercurrents measured over 152 days at a depth of 3100 m in the middle of the Pacific Ocean [70] (see Figure 2.6), as well as for the fluctuations of sea level at Bermuda measured over 8 years [71]. The interplanetary magnetic field was also shown to follow a similar power law [72].

Fluctuations of audio power in music was investigated in different radio stations of various music styles and showed $1/f$-like power spectra [73, 74]. A same behavior was reported for the shots structure in Hollywood

movies [75]. These two additional examples of $1/f$ fluctuations lead to similar observations made in biological systems. Fluctuations in the human heart beat rate [76], neural activity [77, 78] and even human cognition [79] were shown to follow $1/f$ power laws.

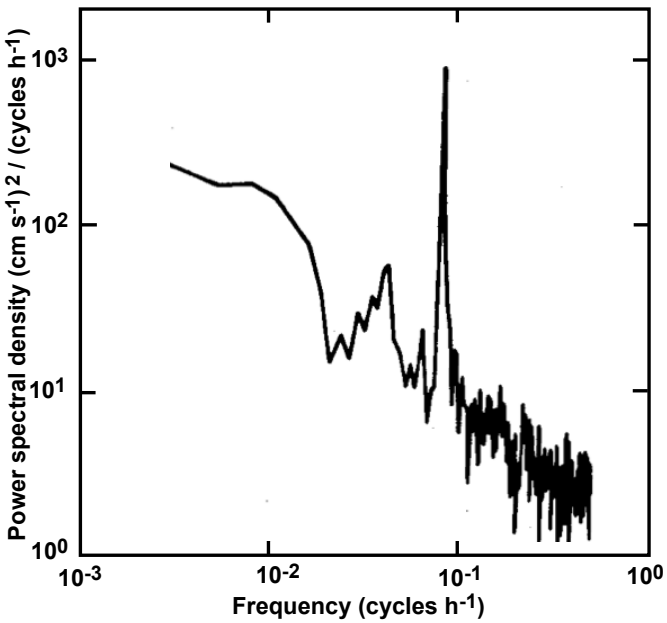

Figure 2.6: Power spectral density of east-west undercurrents velocity at a depth of 3100 m at 1°02'S,149°50'W, reproduced from [70].

Beside the somehow universal character of $1/f$ fluctuations observed in many different physical systems, another puzzling aspect relates to divergence of the power spectral density at low frequencies. A few experimental attempts aiming at assessing the continuity of $1/f$ noise processes were carried out with for instance thin-film resistors, and showed almost perfect $1/f$ spectra over six frequency decades [80]. Noise measurements of an array of operational amplifiers were even performed during a few months and down to Fourier frequencies as low as 0.5 μHz [81], but did not show any flattening of the noise spectra.

At low frequency, the power spectral density of $1/f$ noise diverges and could lead to infinitely large fluctuations. This was expressed jokingly in the review on flicker noises of Ref. [82] as "If you postpone your Bermuda vacation for too long, the island may be underwater!". However, a relatively simple argument was given in Ref. [83] in order to put in perspective the magnitude of low frequency fluctuations. For a pure $1/f$ spectrum, the

integrated fluctuations of each frequency decade are equal to each others, and the total fluctuation is given by:

$$\int_{f_0}^{f_1} \frac{1}{f}\,\mathrm{d}f = \ln\left(\frac{f_1}{f_0}\right) \tag{2.9}$$

Considering the lowest observable frequency as the inverse of the universe lifetime ($\approx 10^9$ years $\approx 3 \cdot 10^{16}$ s) and the inverse of Plank's time ($5 \cdot 10^{-44}$ s) as the highest observable frequency, the total fluctuation would be approximately only $\ln(10^{60})/\ln(10) = 60$ times the integrated fluctuation of one frequency decade, e.g. from 1 to 10 Hz. This simple approximation shows that the mathematical divergence of $1/f$ noise has no real impact on physical systems in reasonable time scales.

$1/f$ fluctuations in electronic devices were of course extensively investigated and have occupied scientists' mind for a long time. Low-frequency fluctuation showing $1/f$ power spectra were already reported a long time ago in vacuum tubes [68, 84], p-n germanium junctions and carbon resistors [84], as well as in metallic thin-films [85–87] and semiconductor homogenous samples [88]. A few models were proposed in order to explain $1/f$ noise in homogenous semiconductor and MOS transistors, and generally confront mobility fluctuations $\Delta\mu$ to carrier numbers fluctuations ΔN, which are associated either to bulk or surface effects, respectively. McWorther proposed a model involving trapping et detrapping of carriers at the Si-SiO_2 interface of MOS transistors and explained $1/f$ fluctuations by changes of the number of carriers [89]. The idea behind this model is a sum of spectra with a wide distribution of relaxation times, the probability that an electron reaches a trap in the oxide being $\tau = \tau_0 e^{x/d}$, where x is the distance between the traps and the interface, and d is a characteristic of the tunneling process.

On the other hand, Hooge proposed in 1969 the following empirical relation for the power spectral density S of flicker noise in homogenous semiconductors [90]:

$$\frac{S_R}{R^2} = \frac{S_I}{I^2} = \frac{S_V}{V^2} = \frac{\alpha}{fN} \tag{2.10}$$

where f is the Fourier frequency, N is the total amount of carriers in the sample, and α is a parameter that was first believed to be constant. α values on the order of $2 \cdot 10^{-3}$ were indeed measured in several III-V semiconductors such as p-type and n-type InSb, GaSb, GaAs and GaP [88].

Later, it was demonstrated that α strongly depends on the quality of the crystal as well as on the scattering processes determining the mobility [91].

Despite some attempts at unifying the two theories [92] and recursive discussions about the effect of carriers number and mobility fluctuations in MOS transistors [93], various experimental results support so far both bulk and surface-state effects [94] and it seems difficult at this point to conclude on the supremacy of one of these models. In the light of the universal character of $1/f$ fluctuations in physical systems, it is also important to emphasize that the underlying physical mechanisms might very well be different from a system to another, despite the manifestation of similar $1/f$-like power laws [95].

The investigation of low-frequency noise processes in solid-state devices is nowadays still of prime interest for the realization of low-noise electronic devices for telecommunications, consumer electronics and sensors. It is particularly the case of semiconductor lasers, which will be discussed in Chapters 4 and 5. Low-frequency fluctuations were also more recently studied in GaN/AlGaN high electron mobility transistors [96,97] and graphene solid-state devices [98], in which $1/f$ noise was even used as a signal for sensing applications [99].

2.4 List of QCLs used in this work

Different distributed-feedback QCLs provided by Alpes Laser SA emitting around $\lambda = 4.55$ µm were used throughout this work. Optical powers ranging from 5 to 15 mW were obtained at room-temperature. The devices are listed along with their manufacturing number in Table 2.1.

Device	Processing	Mounting	i_{th}[1]	Used in
sbcw2689	Ridge-waveguide	epi-side up	300 mA	Chap. 3, 4, 5
sbcw2694	Ridge-waveguide	epi-side up	355 mA	Chap. 4, 5
sbcw3661	Buried-heterostructure	epi-side up	140 mA	Chap. 5
sbcw4210	Buried-heterostructure	epi-side up	200 mA	Chap. 5, 6

[1] at 283 K

Table 2.1: List of QCLs used in this work.

Chapter 3

Wavelength tuning and thermal dynamics of CW QCLs

In this chapter, the dynamic behavior of the optical frequency and temperature in continuous wave (CW) mid-IR DFB-QCLs under direct current modulation is presented. Frequency modulation of single-mode semiconductor lasers is important for several applications, such as optical communications [100], and also for advanced enhancement techniques in absorption spectroscopy for trace-gas sensing [101]. In the framework of this thesis, two other main interests motivate the study of the frequency-modulation response of QCLs:

- Narrow linewidth sources of coherent light in the mid-IR, required to push the limits of high-resolution spectroscopy and metrology, can be achieved by active stabilization of DFB-QCLs to optical references with high-bandwidth servo-loops. The frequency-modulation bandwidth can affect the feedback loop bandwidths and therefore limit the ultimate achievable performances in terms of linewidth narrowing [102].
- The dynamic response of the optical frequency is of prime interest to gain a deeper insight in the origin of frequency instabilities in QCLs. The study of the dynamic response gives access to the thermal dynamics in the QCL structure and allows the identification of the different thermal mechanisms involved in the appearance of frequency instabilities and frequency noise in DFB-QCLs.

Despite the fact that the thermal resistance and the heat extraction in pulsed QCLs have been deeply investigated [103–105], this chapter also enables the dynamics of thermal effects in CW DFB-QCLs under direct current modulation to be discussed.

3.1 Basics of frequency-modulation

Let us consider pure frequency-modulation of the light field, whose instantaneous frequency is given by Eq. 3.1 where $\Delta\nu$ is the frequency excursion and f_m the modulation frequency. The modulation index β is defined in Eq. 3.2 as the ratio of the frequency excursion to the modulation frequency.

$$\nu(t) = \nu_0 + \Delta\nu \cos(2\pi f_m t) \tag{3.1}$$

$$\beta = \frac{\Delta\nu}{f_m} \tag{3.2}$$

The electrical field can be expanded as a series of Bessel functions of the first kind $J_n(\beta)$ [56, 106], and its explicit development is shown in Eq. 3.4.

$$E(t) = E_0 \sum_{n=-\infty}^{\infty} \Re\left\{ J_n(\beta) e^{2\pi i(\nu_0 + n f_m)t} \right\} \tag{3.3}$$

$$\begin{aligned} E(t) = E_0 \{ & J_0(\beta)\cos(2\pi\nu_0) \\ & + J_1(\beta)[\cos(2\pi(\nu_0 + f_m)t) - \cos(2\pi(\nu_0 - f_m)t)] \\ & + J_2(\beta)[\cos(2\pi(\nu_0 + 2f_m)t) + \cos(2\pi(\nu_0 - 2f_m)t)] \\ & + J_3(\beta)[\cos(2\pi(\nu_0 + 3f_m)t) - \cos(2\pi(\nu_0 - 3f_m)t)] \\ & + J_4(\beta)[\cos(2\pi(\nu_0 + 4f_m)t) + \cos(2\pi(\nu_0 - 4f_m)t)] \\ & + ... \} \end{aligned} \tag{3.4}$$

Eq. 3.4 shows that the spectrum of a frequency-modulated electrical field is composed of an infinity of equally spaced sidebands at integer multiples nf_m of the modulation frequency. Moreover, for a given modulation index β, the relative amplitude of the n^{th} sidebands with respect to the carrier can be simply deduced from the ratio of the corresponding Bessel functions $J_n(\beta)$ to $J_0(\beta)$.

3.2 Frequency modulation of DFB lasers

3.2.1 Interband semiconductor lasers

Frequency-modulation (FM) of interband DFB laser diodes under direct current modulation was extensively investigated in devices emitting in the near-IR [107, 108], at 1.3 μm [108, 109] and at 1.5 μm [110–112]. Two main mechanisms are responsible for frequency-tuning in semiconductor lasers based on interband transitions, namely a thermal effect and a carrier density effect.

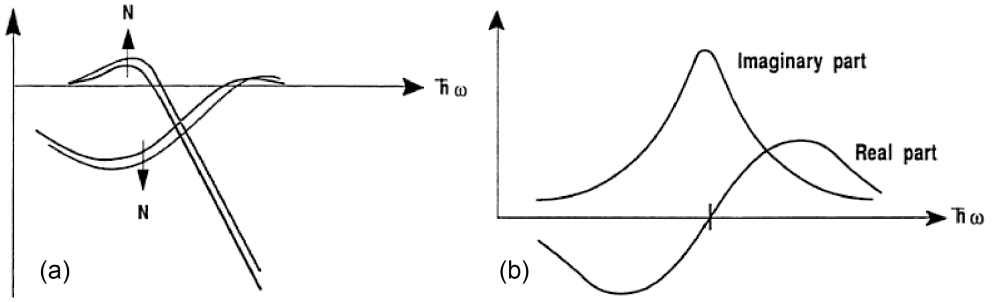

Figure 3.1: Real and complex part of the refractive index in (a) interband and (b) intersubband transitions as a function of the photon energy. Reproduced from [113].

Thermal effect

The temperature-dependent refractive index of the semiconductor materials forming the laser cavity is directly linked to the effective optical length of the resonator and is the main contributor to frequency tuning. The relative change in optical frequency is given by:

$$\frac{1}{\nu}\frac{d\nu}{dT} = -(\alpha_n + \alpha_L) \tag{3.5}$$

where α_n is the relative refractive index temperature coefficient and α_L is the linear expansion coefficient. The relative change in refractive index of InP with respect to temperature is on the order of $5.5 \cdot 10^{-5}$ K^{-1}, whereas the linear expansion coefficient is one order of magnitude smaller [114]. From Eq. 3.5, typical frequency tuning coefficient of 12 GHz/K can be calculated for DFB lasers at 1.5 μm. This effect is relatively slow since it is limited by the thermal time constant required to change the temperature in the laser chip.

The thermal contribution to the frequency modulation was experimentally investigated and analytical models of the heat conduction in simplified laser structures were developed [107, 115]. The bandwidth of this effect depends on the laser structure and is limited to frequencies below 1 MHz [116].

Carrier density

The refractive index of the laser resonator and its emission frequency depend on the carrier density N, and therefore on the injection current. Indeed, the gain curve is not symmetric in interband semiconductor lasers and its peak shifts towards higher photon energies when the carrier density increases. As a result, the real part of the refractive index, and therefore the emission frequency, depends on the carrier density as shown in Figure 3.1 [113].

This effect is usually quantified using the α parameter (α_e or α_H are sometimes used), which is defined as the ratio of the change of the real part n_r to the imaginary part n_i of the refractive index with respect to the carrier density N:

$$\alpha = \frac{dn_r}{dN} \Big/ \frac{dn_i}{dN} \tag{3.6}$$

The dynamic of this effect relies on the lifetime of the carriers, which is in the nanosecond range [117], and is much faster than the thermal effect. Typical frequency modulation bandwidths in the GHz regime have been reported in near-IR laser diodes [107, 110]. Multisection devices with multiple electrodes for selective carrier density modulation have been investigated [118], and frequency modulation bandwidths up to 15 GHz [119] have been achieved using such designs.

The combined effects of temperature and carrier density on the frequency modulation of a singlemode AlGaAs DFB semiconductor laser emitting at 840 nm is shown in Figure 3.2 [107]. The dashed line represents the thermal effect, showing a thermal cut-off frequency in the MHz range, while the solid line denotes the effect of charge carriers at higher frequencies.

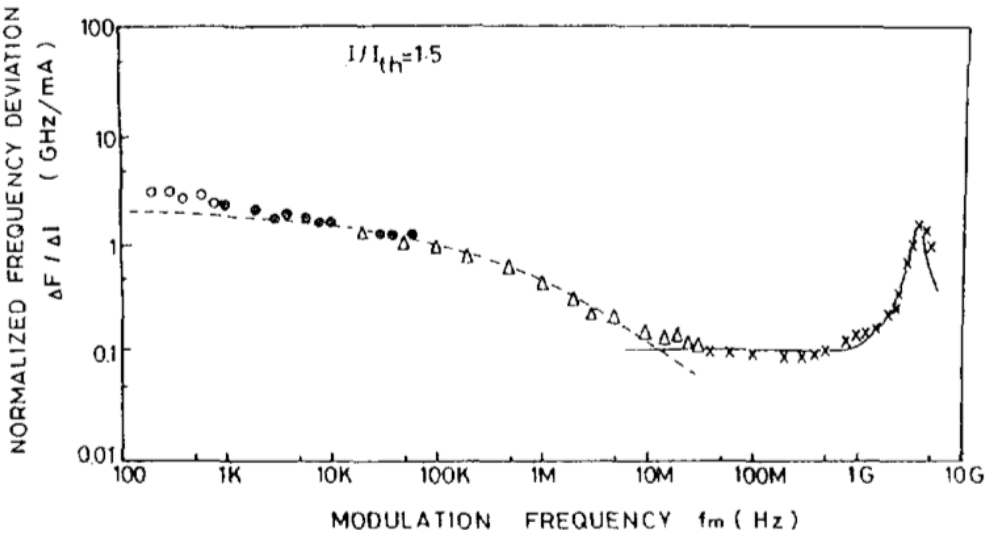

Figure 3.2: Frequency-modulation response of a singlemode AlGaAs DFB laser at 842 nm [107]. At low frequencies, the FM response is mainly governed by thermal effects (dashed line). Above 10 MHz, the solid line denotes the carrier-density effect.

3.2.2 Intersubband semiconductor lasers

In QCLs, the picture is fundamentally different. Unlike interband transitions, the gain curve of intersubband transitions is symmetric. As shown in Figure 3.1, the associated refractive index is independent in that case of the carrier density at the gain peak, which results in a zero, or close-to-zero alpha parameter [120, 121]. The tuning of the optical frequency -or wavelength- of DFB-QCLs is therefore mainly governed by the temperature dependence of the average refractive index of the active region, with a typical tuning-rate on the order of $1/\lambda \; d\lambda/dT = 7 \cdot 10^{-5}$ 1/K [26]. This value leads to temperature tuning coefficients $\beta_T = \Delta\nu/\Delta T$ on the order of 4.5 GHz/K at 4.6 µm and 2.8 GHz/K at 8 µm.

The effect of the injection current on the laser frequency tuning can then be inferred from Eq. 3.7:

$$\Delta\nu = \beta_T \Delta T = \beta_T R_{th} \Delta P \tag{3.7}$$

where R_{th} is the thermal resistance and ΔP is the dissipated electrical power (defined in Eq. 3.8 as a function of the current modulation Δi, bias current i_0, voltage U_0, and differential resistance R_d).

$$\Delta P = (U_0 + R_d i_0)\Delta i + R_d \Delta i^2 \tag{3.8}$$

The current tuning coefficients depends on both the thermal resistance and the electrical characteristics of the QCLs. Typical values are comprised between 200 MHz/mA and 1 GHz/mA.

While the picosecond carrier lifetime in QCLs allows a very fast intensity modulation above 10 GHz [46, 122], the ability to modulate the frequency of a QCL with the drive current is limited by the thermal time constants of the semiconductor structure, i.e. the time required for the temperature to follow the modulation of the dissipated electrical power.

3.3 Frequency-modulation characterization

Several methods can be used to measure the frequency modulation response of a laser such as Fabry-Perot [107] or Michelson [123] interferometers. Here, the frequency response of QCLs under direct current modulation was measured using single-pass direct absorption spectroscopy, as shown in Figure 3.3. The QCL beam passes through a cell filled with a reference gas at low pressure, e.g. carbon dioxide (CO_2) or carbon monoxide (CO). The emission frequency is tuned to the flank of the respective molecular absorption line, which acts as a frequency-sensitive element. At this point, the frequency fluctuations of the laser are converted into intensity fluctuations that are detected with a photodiode.

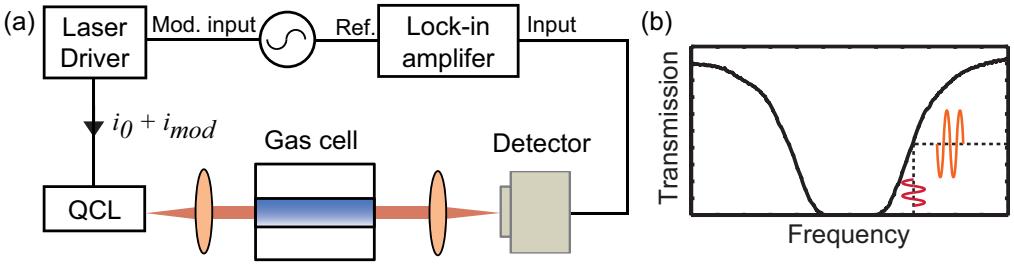

Figure 3.3: (a) FM response measurement setup. The frequency excursion $\Delta\nu$ of the optical carrier at 4.55 µm ($\nu \approx 66$ THz) is measured as a function of the current modulation frequency f_m. (b) Frequency-to-intensity conversion principle.

The conversion factor, or frequency discriminator, is given by the slope of the absorption line. Similar setups were used for frequency-noise char-

acterization of free-running mid-IR [52, 124] and THz [125] QCLs and a complete description can be found in Chapter 4.

For the measurements presented here, the current of the QCLs was modulated from 100 Hz up to several MHz and the associated laser frequency modulation was measured in magnitude and phase using a lock-in amplifier. A small sinusoidal modulation i_{mod} on the order of 0.2 mA peak-to-peak was used in order to keep the laser frequency in the linear range of the molecular absorption line and avoid any distortion of the output signal.

The current driver and the photodiode benefit from bandwidths of several MHz and more than 50 MHz, respectively, and allow the measurement of the frequency modulation response up to several MHz without introducing any additional roll-off. Nevertheless, the laser intensity modulation response measured by detuning the laser out of the resonance was used to scale the magnitude and compensate for the slight phase shift introduced by the current driver at higher frequencies so that it reflects the dynamic response of the laser frequency only, as in Ref. [126].

Two QCLs from different suppliers were characterized and compared. The first one is the same ridge waveguide DFB-QCL used in Ref. [52] and Chapter 4 (epi-side up), emitting at 4.55 µm. The second one is a 4.33 µm ridge-waveguide DFB-QCL from Hamamatsu Photonics (epi-side down). The measurements of this second device were performed in Italy, at LENS (European Laboratory for Nonlinear Spectroscopy). These two devices are labeled QCL1 and QCL2 respectively, and their main characteristics are listed in Table 3.1. QCL1 was mounted in a cryostat and its frequency-response was measured over a broad temperature range, from 283 K down to 95 K. QCL2 was mounted in a sealed package and its frequency response was measured at 285 K.

Device	Supplier	λ	epi-side	i_{th}[1]	i_0[1]	P_0[1]
QCL1	Alpes Lasers	4.55 µm	up	300 mA	350 mA	5 mW
QCL2	Hamamatsu	4.33 µm	down	660 mA	710 mA	5 mW

[1] at 283 K

Table 3.1: QCLs used for FM response measurements.

3.4 Frequency-modulation response

The frequency modulation response of QCL1 and QCL2 under direct current modulation is disclosed in Figure 3.4(a) and Figure 3.4(b), respectively. The two devices show similar a behavior. In the high-frequency region, a clear roll-off of -20 dB/decade and its associated phase shift are observed, in both cases beyond 200 kHz. In the low-frequency region, it is important to note that the frequency-response is not flat and differs from a first order low-pass filter. Indeed, a roll-off of a few dB/decade in the magnitude as well as a non-negligible phase shift are observed above a few hundred Hz already.

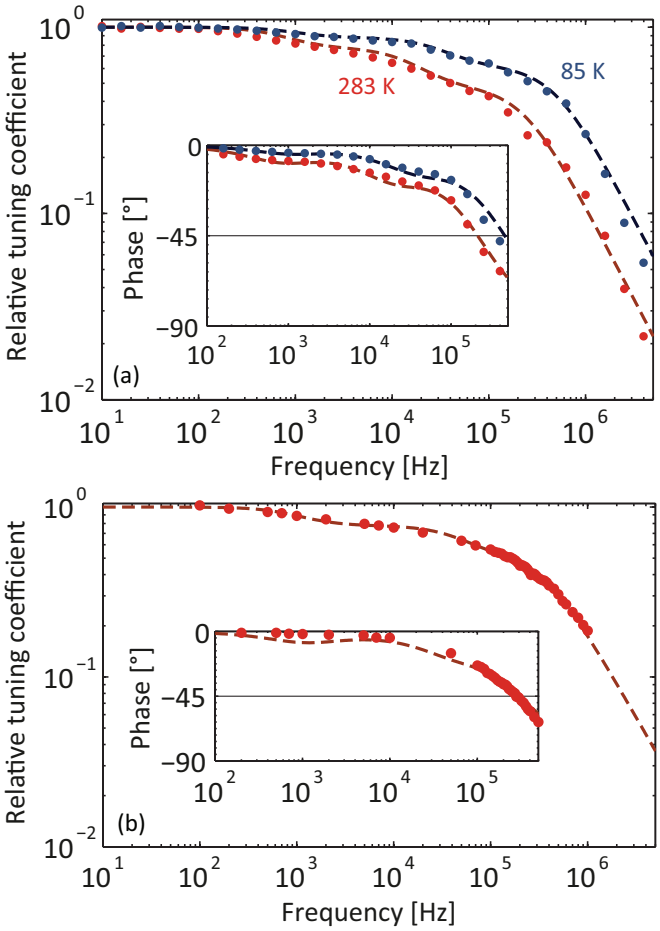

Figure 3.4: Relative frequency-modulation response of (a) QCL1 (at 283 K and 85 K) and (b) QCL2 (at 283 K) under direct current modulation (Δi_{pp} = 0.2 mA) and fitted model (dashed lines). The phase shift between frequency- and current-modulation is shown in the inset.

At room-temperature, the frequency-modulation bandwidth of QCL2 is slightly higher than the one of QCL1. The frequency at which the phase shift reaches -45° is 200 kHz for QCL1 and 300 kHz for QCL2 while the attenuation of the tuning coefficient is pretty strong and reaches a factor of 2 with respect to the DC value already at modulation frequencies lower than 100 kHz. It is important to note that one order of magnitude separates the -45° and -3dB frequencies, which supports the observation that the dynamic-response is not governed by a simple one-pole low-pass filter.

The dynamic response of QCL1 was also measured over a broad temperature range, from 283 K down to 85 K, and is reported in Figure 3.4(a) for these two temperature values. We observe that when the temperature is lowered, the modulation bandwidth increases and both the low-frequency roll-off and phase shift become smaller. The -45° frequency increases from 200 kHz at room-temperature up to 400 kHz at 85 K. Moreover, the dynamic response at 85 K is qualitatively closer to a first order low-pass filter, with a weaker roll-off in the low-frequency range.

3.5 Thermal model

In order to have a deeper understanding of the observed dynamic responses and especially of the roll-off and phase shift at low frequency, a thermal model was used to fit the experimental data in magnitude and phase.

A similar behavior was observed with interband semiconductor DFB lasers (see Figure 3.2), and various analytical models were derived [107, 115, 116] in order to explain the thermal dynamics in these structures. In contrast to previous analytical models, a simple thermal response $R(f)$ (Eq. 3.9) consisting of three cascaded first-order low-pass filters of characteristics frequencies f_i (Eq. 3.10) is considered here. The model is illustrated in Figure 3.5.

$$R(f) = \frac{\Delta T}{\Delta P}(f) = \sum_{i=1}^{3} \frac{R_i}{1 + j\frac{f}{f_i}} \tag{3.9}$$

$$f_i = \frac{1}{2\pi R_i C_i} \tag{3.10}$$

The fitted model is plotted along with the measured frequency modulation responses in Figure 3.4 and shows a good agreement with both the

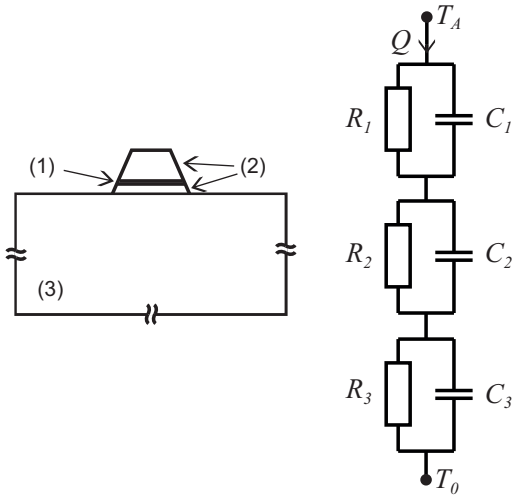

Figure 3.5: Left: simplified cross-section of the QCL: (1) active region, (2) cladding, (3) substrate. Right: Thermal model. T_A is the average temperature of the active region, T_0 the heat-sink temperature, Q the heat flux, R_i the thermal resistances, and C_i the thermal capacitances.

magnitude and phase of the experimental data. Assuming that the output frequency of the laser is a direct image of the average temperature in the active region and that the current modulation induces a proportional variation of the electrical power dissipated in the device, the frequency tuning response therefore also reflects the laser thermal response. The model parameters allow the identification of the different thermal time constants of the system and their relative contributions r_i (Eq. 3.11), defined by:

$$r_i = \frac{R_i}{\sum_{i=1}^{3} R_i} \tag{3.11}$$

The three characteristic frequencies determined from the model (f_1, f_2, f_3) are reported with their respective normalized weights (r_1, r_2, r_3) in Table 3.2 for QCL1 and QCL2 at 283 K. The three characteristic frequencies are higher in QCL2, which is in agreement with the higher overall modulation bandwidth observed in this device.

The highest cut-off frequency, on the order of $f_1 \approx 200$ kHz (time constant shorter than 1 µs) reflects the heat dissipation in the small volume of the active region itself, along the planes of the heterostructure. The second characteristic frequency $f_2 \approx 20$ kHz likely corresponds to the heating

Device	f_1	r_1	f_2	r_2	f_3	r_3
QCL1	200 kHz	0.46	16 kHz	0.31	550 Hz	0.23
QCL2	353 kHz	0.49	46 kHz	0.29	900 Hz	0.22

Table 3.2: Cut-off frequencies f_i and relative contributions r_i of QCL1 and QCL2 at 283K.

due to heat extraction perpendicular to the planes of the heterostructure and through the waveguide layers. Indeed, the lower cross-plane thermal conductivity compared to the in-plane value [104], the additional thermal resistivity of the cladding layers and the larger associated volume contribute to this second longer thermal time constant. Finally, a third characteristic frequency f_3 lying below 1 kHz is attributed to the heat extraction through the substrate and the soldering which represent a relatively high thermal inertia compared to the waveguide and active region.

These three distinct regions are illustrated in the simplified QCL cross section in Figure 3.5. The thermal time constants are on the same order of magnitude as simulated values for pulsed devices [105] and experimental results on THz QCLs [127].

3.5.1 Step response

Figure 3.6 shows the measured time evolution of QCL1 optical frequency when a step of current is applied to the laser. It illustrates the deviation from a single exponential response.

Indeed, whereas the heating of the active region itself ($\tau_1 \approx 1$ µs, which cannot be resolved in the plot) and of the waveguide ($\tau_2 \approx 8$ µs) is pretty fast, it then takes more time ($\tau_3 \approx 400$ µs) to reach the final temperature because of the relatively high thermal inertia of the substrate and possibly of the soldering. The step response corresponding to the thermal model can be written as a sum of exponential growths (Eq. 3.12).

$$\frac{T(t) - T_0}{\Delta T} = \sum_{i=1}^{3} r_i (1 - e^{-\frac{t}{\tau_i}}) \tag{3.12}$$

The theoretical step response is also plotted in Figure 3.6 and shows a good agreement with the experimental data.

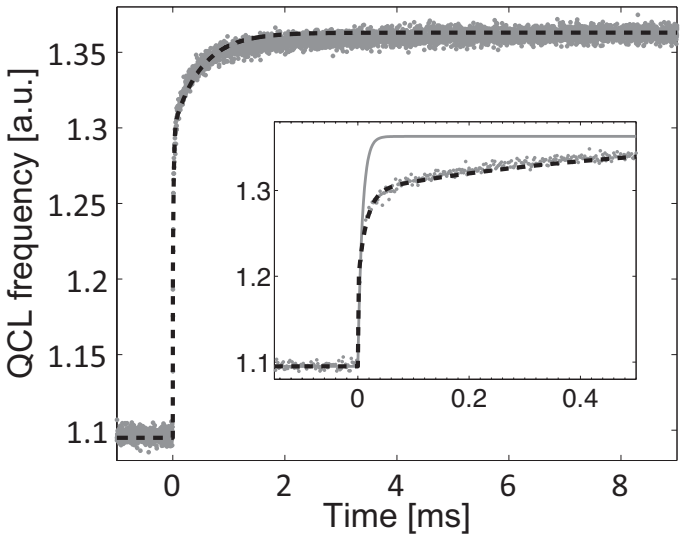

Figure 3.6: Experimental (grey points) and modeled (dashed line) time evolution of the QCL optical frequency when a current step is applied. Inset: zoom over the first 500 µs which shows a significant deviation from a simple 8 µs time constant exponential growth (solid line).

3.5.2 Temperature dependence

From the experimental frequency-modulation response measured at different temperatures for QCL1 between 85 K and 283 K, the different characteristic frequencies f_1, f_2 and f_3 were extracted and are plotted in Figure 3.7 as a function of the laser heat-sink temperature.

We observe that all these thermal cut-off frequencies increase when the device is cooled down over the considered temperature range, e.g. from 200 kHz at 283 K up to 500 kHz at 85K for f_1. This is in qualitative agreement with the fact that both the thermal resistivity and the specific heat of the semiconductor compounds of the QCL structure are monotonously decreasing with decreasing temperature in the considered range [104, 117], leading to higher thermal cut-off frequencies.

The values of R_1, R_2 and R_3 determined from the fit of the normalized frequency responses directly give the relative contributions r_i (Eq. 3.11) of the different thermal resistances of each part of the QCL structure to the total thermal resistance and are shown in Figure 3.8. The contribution of the thermal resistance R_1 of the active region to the total thermal resistance is clearly dominant all over the temperature range. Moreover, whereas it amounts to 45% at room-temperature, the contribution of R_1

reaches almost 70% of the total thermal resistance at low temperature and explains the smaller roll-off observed in the low-frequency range at 85 K in Figure 3.4.

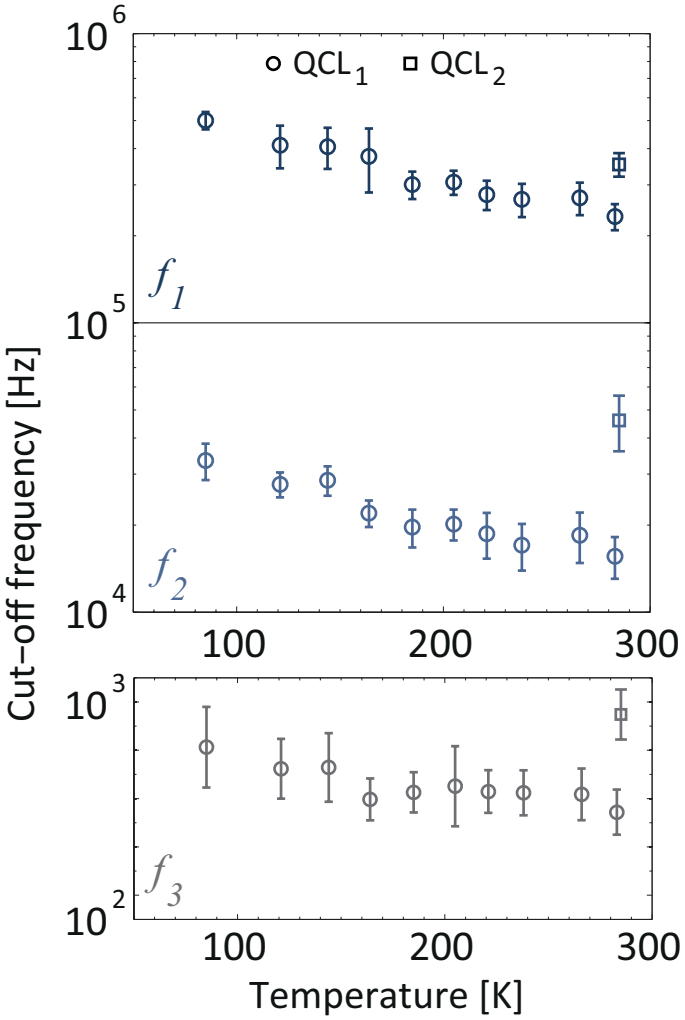

Figure 3.7: Temperature dependence of the cut-off frequencies f_1, f_2 and f_3 extracted from the fit of the thermal model. The error bars represent the standard deviation σ on the fit parameters.

This behavior is attributed to the fact that the thermal resistivity of bulk InP decreases at a faster rate than the thermal resistivity of the heterostructure when the temperature is lowered [104, 128]. The contribution of the thermal resistance of the substrate to the total thermal resistance becomes therefore weaker at low temperature, which increases the weight of the fastest process (active region) in the global thermal behavior. This ob-

servation is in agreement with the dynamic response of the cryogenic QCL of Ref. [126] which shows a relatively flat response in the low-frequency range and qualitatively resembles a first-order low-pass filter.

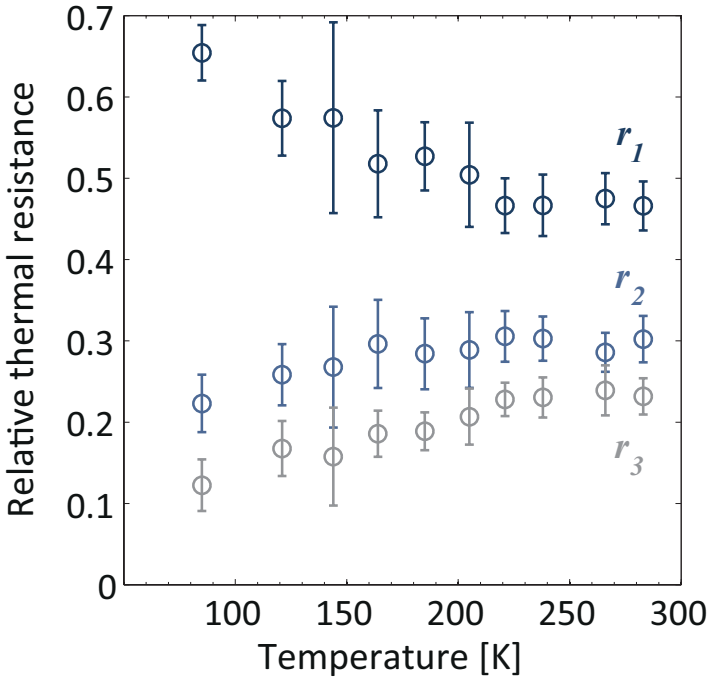

Figure 3.8: Relative contributions r_1, r_2, r_3 of the model thermal resistances to the total thermal resistance (Eq. 3.11) (standard deviation σ given by the error bars).

3.6 Fast electrical modulation

Figure 3.9 shows the power spectrum of the laser field for a current modulation frequency $f_m = 15$ MHz, measured using a scanning Fabry-Perot interferometer.

As discussed in Section 3.1, the ratio of the electrical field amplitude of the carrier to the first sidebands amplitude depends on the frequency modulation index β and can be inferred from Eq. 3.13, where $J_0(\beta)$ and $J_1(\beta)$ are the Bessel functions of the first kind of order 0 and 1, respectively.

$$\frac{E_0}{E_1} = \frac{J_0(\beta)}{J_1(\beta)} \tag{3.13}$$

The amplitude of the current modulation was adjusted in order to achieve a modulation index β=1, which corresponds to a power ratio between the carrier and sidebands of $(E_0/E_1)^2 = (J_0(1)/J_1(1))^2 = 3$ (from Eq. 3.13). In this situation, it can be inferred from Eq. 3.2 that the frequency excursion is equal to the frequency modulation and Δf=15 MHz.

A current modulation amplitude $\Delta i = 2$ mA was found to achieve a modulation index of 1, which corresponds to a modulation efficiency $\Delta f/\Delta i = 7.5$ MHz/mA. This value is in good agreement with the combination of the static current tuning coefficient of ≈ 900 MHz/mA and the frequency-modulation responses measured in Section 3.4.

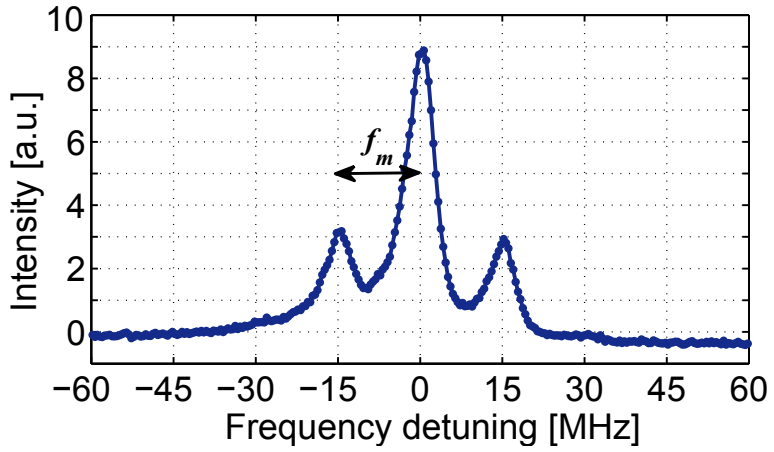

Figure 3.9: Optical spectrum measured through a Fabry-Perot interferometer for a current modulation at $f_m = 15$ MHz and a modulation index $\beta = 1$ (QCL temperature $T = 283$ K).

Fast frequency-modulation ($f_m = 10 - 30$ MHz) is for instance required for frequency-stabilization of lasers to high-finesse reference cavities using the Pound-Drever-Hall scheme, which yields a maximum sensitivity for a modulation index $\beta = 1.08$ [56]. Whereas frequency modulation is often achieved with electro-optical modulators (EOMs) at near-IR wavelengths, these devices are less widespread and less efficient in the mid-IR spectral region, and the measurement shows that sufficient frequency-modulation above 10 MHz can be achieved with a reasonable current modulation amplitude despite the strong thermal cut-off reported in Figure 3.4.

In this case, for a current modulation of $\Delta i = 2$ mA, the modulation of the laser output power is on the order of $\Delta I = 150$ µW and represents an intensity modulation index lower than 2.5% ($I_0 > 6$ mW).

3.7 Conclusion and outlook

To conclude, the frequency-modulation response of two CW mid-IR DFB-QCLs under direct current modulation was presented. Despite a frequency-modulation bandwidth on the order of a few hundreds of kHz, a non-negligible roll-off and a significant phase shift appear above a few hundred Hz already. This behavior was analyzed and linked to the thermal dynamics in the lasers.

Although the general behavior of the two QCLs is very similar, it is important to note that the higher cut-off frequencies measured with the epi-side down device (QCL2) are very likely due to the junction-down mounting of this laser, which reduces the thermal resistance and therefore the thermal time constants. Device mounting might therefore be critical for applications requiring high frequency-modulation bandwidth and could be an important limiting factor for efficient linewidth narrowing.

It is also worth mentioning that the model and method presented in this chapter could be useful for the determination of the thermal physical parameters of the QCL. Indeed, whereas we focused on the dynamic behavior and fitted relative frequency-responses, the use of the absolute frequency-tuning coefficients allows R_i and C_i values of the model to be retrieved and for instance the specific heat of QCL heterostructures to be assessed. From the obtained experimental values r_i and f_i, the total thermal capacity of each portion of the model is indeed given by:

$$C_i = \frac{1}{2\pi f_i r_i R_{th}} \tag{3.14}$$

where R_{th} is the total thermal resistance of the QCL. For QCL1, the thermal capacities of the active region C_1, the cladding layers C_2 and the substrate C_3 calculated from Eq. 3.14 are shown in Table 3.3 ($T = 300$ K, R_{th}=14 K/W).

The theoretical thermal capacities can be calculated from the volume V and the specific heat of InP $c = 0.3$ J/g$\cdot$K at 300 K [117]. For the substrate (cross section of $150 \cdot 150$ µm^2, length of 3 mm), we find a thermal capacity of $C_3 = c\rho V_3 = 9.7 \cdot 10^{-5}$ J/K, which is in excellent agreement with the value obtained from the dynamic measurements of Table 3.3. The same comment applies to the cladding layers. Assuming a cross-section of $\approx$ 200 µm^2, a value of $C_2 = c\rho V_2 = 1 \cdot 10^{-6}$ J/K is found, which is in fair agreement with the value of Table 3.3.

i	f_i	r_i	C_i
1	200 kHz	0.46	$1.2 \cdot 10^{-7}$ J/K
2	16 kHz	0.31	$2.3 \cdot 10^{-6}$ J/K
3	550 Hz	0.23	$8.9 \cdot 10^{-5}$ J/K

Table 3.3: Calculated thermal capacities of QCL1 from the experimental values at 300 K and a total thermal resistance $R_{th} = 14$ K/W.

The specific heat of the heterostructure can now be calculated from the experimental value of C_1. Considering a cross-section of the active region on the order of 15 μm^2, we find a specific heat of $c_{heterostructure} = C_1/(\rho V_1) \approx 0.55$ J/(g$\cdot$ K), which is slightly higher than the value of bulk InP and other III-V semiconductor compounds [117].

Finally, this chapter raises the question of frequency modulation of QCLs at higher frequency (> 100 MHz) when the thermal tuning becomes negligible. Indeed, frequency-modulation spectroscopy at 300 MHz was achieved in Ref. [129], and some frequency modulation due to carrier density could possibly occur, especially if laser operation is not centered at the gain peak.

Chapter 4

Spectral purity of mid-IR QCLs

Although lasers are generally considered as monochromatic light sources, their emission linewidth is at some extent not infinitely narrow. In other words, the frequency -or energy- of the emitted photons fluctuates in time, either because of external perturbations or fluctuations that are intrinsic to the physics of the devices themselves. This chapter treats the spectral purity of continuous-wave mid-IR distributed-feedback QCLs at 4.6 μm.

First of all, the design of a low-noise current source is presented. QCLs are electrically pumped semiconductor lasers and a stable injection current is required for low-noise operation. Different solutions are compared and their limitations are discussed. Secondly, the different methods that were used to access the frequency of the mid-IR radiation (66 THz at 4.6 μm) will be presented. Such a high frequency cannot be indeed directly resolved by any electronic device and frequency-to-intensity conversion was used through interferometric and spectroscopic techniques. In this chapter, the focus is put on a method based on absorption spectroscopy and its optimization. Frequency-noise measurements of room-temperature devices are then disclosed. Finally, the impact of the driving electronics on the spectral purity of QCLs is assessed. This last part shows how the effect of noisy electronics can drastically degrade the spectral properties of QCLs and that great care must be taken in order to achieve narrow linewidths. Finally, the results are compared to the state-of-the-art QCLs and conventional interband semiconductor laser diodes.

4.1 Low-noise electronics for QCLs

This section treats the design and realization of low-noise electronics to drive QCLs. The relatively high operating voltage intrinsic to QCLs, on the order of 10 V to more than 15 V depending on the wavelength and design, imposes several limitations compared to current sources dedicated at driving conventional interband semiconductor laser diodes (U = 1-2 V). Even though commercial solutions reaching reasonable current-noise levels can nowadays be bought off the shelf, their availability was simply inexistent when the first experiments related to the present work were carried out, and a low-noise current source was developed.

4.1.1 Custom and commercial low-noise solutions

A couple of different current drivers have been used all along this work. The first experiments were carried out using a home-made solution based on the Libbrecht-Hall design [130]. As shown in Section 4.1.4, this current driver enabled extremely low levels of current noise to be reached, on the order of 300 pA/Hz$^{1/2}$. This value is still state-of-the-art today, and is only approached but not equaled by the best available commercial solutions. In order to perform the frequency-noise measurements at cryogenic temperature reported in Chapter 5, another current source also based on the Libbrecht-Hall design was used. This solution was provided through a collaboration with TU-Darmstadt (TUD) and mainly enabled reaching a higher compliance voltage. Finally, the stabilization experiments of Chapter 6 were carried out using a commercial solution from Wavelength Electronics (model QCL500). In this case the compliance voltage is even higher and this source can withstand up to 23 V at a drive current of 500 mA, while still delivering a reasonably low current noise of 1 nA/Hz$^{1/2}$.

Driver	Maximum current	Maximum voltage	Current noise density	Modulation bandwidth
Home-made	400 mA	12 V	300 pA/Hz$^{1/2}$	10 MHz
TU Darmstadt	500 mA	15 V	650 pA/Hz$^{1/2}$	3-4 MHz
WE QCL500	500 mA	23 V	1 nA/Hz$^{1/2}$	2-3 MHz

Table 4.1: Overview of the low-noise current drivers.

The main characteristics of the three drivers are reported in Table 4.1. Other solutions -not considered here- are available on the market but tend to show current noise spectral densities up to two orders of magnitude higher than the figures presented in this chapter, and can hardly be considered as low-noise devices.

4.1.2 QCL driver design

The current source design is based on the Libbrecht-Hall circuit [130] which was modified to suit the relatively high compliance-voltage required to drive QCLs. The core of the current driver consists of the output stage shown in Figure 4.1. An operational amplifier in negative feedback configuration controls the gate voltage of a MOSFET, and therefore the current flowing through the transistor so that the negative differential input equals the control voltage V_c. The voltage drop across the sense resistor R_s is a direct image of the current $i_0 = \frac{V_{reg}-V_c}{R_s}$, which is therefore set by the control voltage V_c within the dynamic range of the operational amplifier. The control voltage V_c can be provided in an analog manner using a stable voltage reference and appropriate filtering, or completely digitally via a microcontroller for remote control [131]. A low temperature-coefficient resistor must be used ($\approx$ ppm/K) in order to guarantee a high long-term current stability.

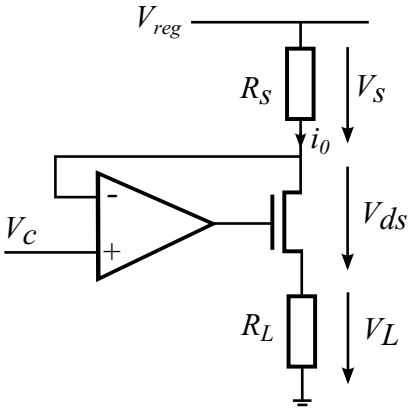

Figure 4.1: Current driver output stage. V_{reg}: regulated voltage, V_c: control voltage, R_s: sense resistor, V_{ds}: drain-source voltage, V_L: load voltage, i_0: drive current.

The main challenge when it comes to driving QCLs is the significantly higher voltage V_L compared to conventional interband semiconductor laser

diodes. The sum of the voltage drops in Figure 4.1 is equal to the regulated voltage V_{reg} (see Eq. 4.1), and this relation sets an upper current limit that cannot be exceeded.

$$V_{reg} = R_s i_0 + V_{ds} + V_L \tag{4.1}$$

Considering $V_{reg} = 18$ V, which is generally the maximum supply voltage for low-noise operational amplifiers, a drive current of 500 mA and a voltage of 15 V, one easily understands that a low value of R_s is required in order to allow a sufficient dynamic voltage range for the QCL and the MOSFET.

4.1.3 Theoretical noise limit

In absence of any technical perturbation, the lowest limit of current-noise achievable by this scheme is defined by the combination of the thermal noise of the sense resistor R_s and the input-referred noise floor of the operational amplifier u_n. The expression of the total current-noise power spectral density (PSD) i_n^2 is given by Eq. 4.2 where k_B is Boltzman constant and T is the temperature.

$$i_n^2 = \frac{4k_B T}{R_s} + \left(\frac{u_n}{R_s}\right)^2 \tag{4.2}$$

Figure 4.2 shows the lowest limit of current-noise PSD as a function of the sense resistor for $u_n = 1$ nV/Hz$^{1/2}$, which is a typical value of input-referred voltage noise for the best low-noise operational amplifiers. It is quite clear from this figure that the highest sense resistor should be used in order to minimize both the thermal noise and the impact of the operational amplifier input noise.

Even though a sense resistor of 50 Ω was used to drive interband laser diodes up to 200 mA with voltage drops of a few volts in the original circuit [130], the picture is completely different when it comes to QCLs since voltages greater than 10 V are required to bias their structure. As explained before (Eq. 4.1) the voltage drop across the sense resistor must be sufficiently low so that a sufficient dynamic is allowed for the voltage drop across the MOSFET V_{ds} and the load V_L. Sense resistors below 10 Ω were used in both the home-made and TUD drivers, which sets a physical limit of current-noise on the order of 200 pA/Hz$^{1/2}$.

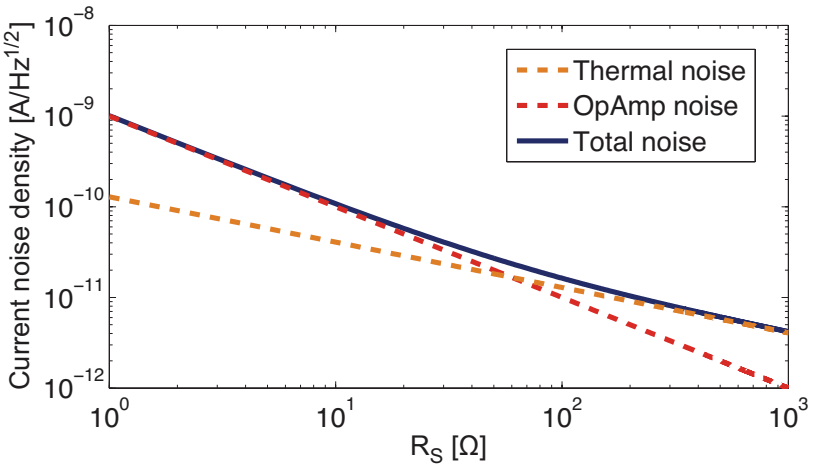

Figure 4.2: Theoretical current-noise limit as a function of the sense resistor R_s for a typical opamp input-referred noise $u_n = 1$ nV/Hz$^{1/2}$.

Another important point that sticks out of the graph is that the input-referred voltage noise of the operational amplifier is the main contributor to the total current noise for low R_s values. In the case of driving high-voltage loads (like QCLs), the role of the operational amplifier is therefore crucial in order to achieve the best performances in terms of current noise.

4.1.4 Current noise

The current noise spectral density of the different QCL drivers is shown in Figure 4.3 for Fourier frequencies ranging from 100 Hz to 100 kHz. In each case it was measured across a 30 Ω resistor at a current of 350 mA, corresponding to a voltage drop of 10.5 V. An FFT spectrum analyzer was used to measure the voltage noise spectral density across the 30 Ω resistor. These measurements are neither limited by the thermal current noise of the resistor, which is $\sqrt{4k_BT/R} = 30$ pA/Hz$^{1/2}$, neither by the FFT spectrum analyzer noise floor.

In each case, the current noise spectral density is relatively flat in the considered frequency range and only a couple of spikes can be observed at low frequencies. In terms of current noise level, the QCL500 driver from Wavelength Electronics meets its specification of 1 nA/Hz$^{1/2}$ and the lowest current noise of 300 pA/Hz$^{1/2}$ was achieved with the home-made QCL driver, which represents an RMS relative stability lower than 1 ppm over a 100 kHz bandwidth. This latter result is in good agreement with the

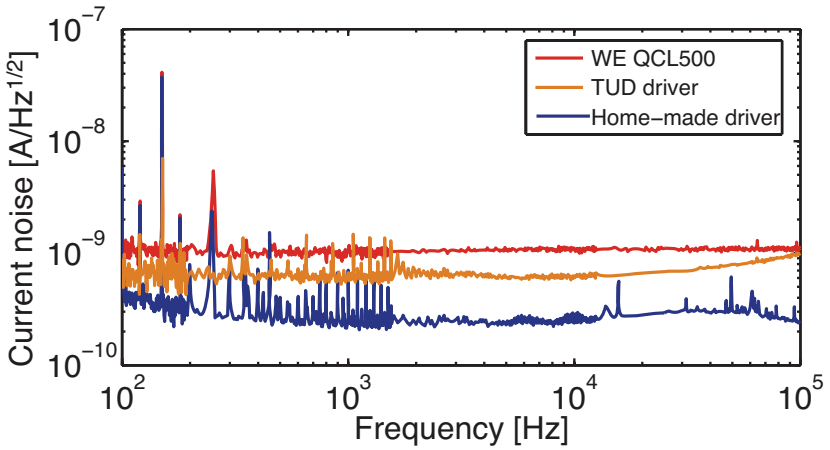

Figure 4.3: Current-noise spectra of the different low-noise QCL drivers ($I_0 = 350$ mA, $U_0 = 10.5$ V).

theoretical limit computed from Eq. 4.2 and Figure 4.2 and shows that the performances of the driver are not limited by any technical contribution. Moreover, the level of current noise is still one order of magnitude lower than recently published values for a low-noise QCL driver [132]. All those current drivers are suitable for low-noise operation of QCLs.

4.1.5 Modulation bandwidth

The ability to modulate the injection current of a QCL in order to generate either intensity or frequency modulation is important in many applications. Intensity modulation can be used for optical communications [45] and frequency modulation is required for advanced techniques in gas-sensing [129]. The current modulation response of the different current drivers was measured using lock-in detection of the voltage across a 30 Ω resistor as a function of the current modulation frequency.

The results are shown in Figure 4.4. Despite their different modulation input coefficient (100 mA/V for QCL500 and 1 mA/V for the others), in each case the current can be easily modulated up to several MHz and the responses do not depend the current modulation amplitudes (assessed from 100 μA_{pp} up to 10 mA_{pp}). However, an important phase-shift between the current and input modulation voltage is observed above 2 MHz. The dip around 200 kHz in the modulation response of the TUD and home-made drivers is attributed to a resonance in the output coupling inductor.

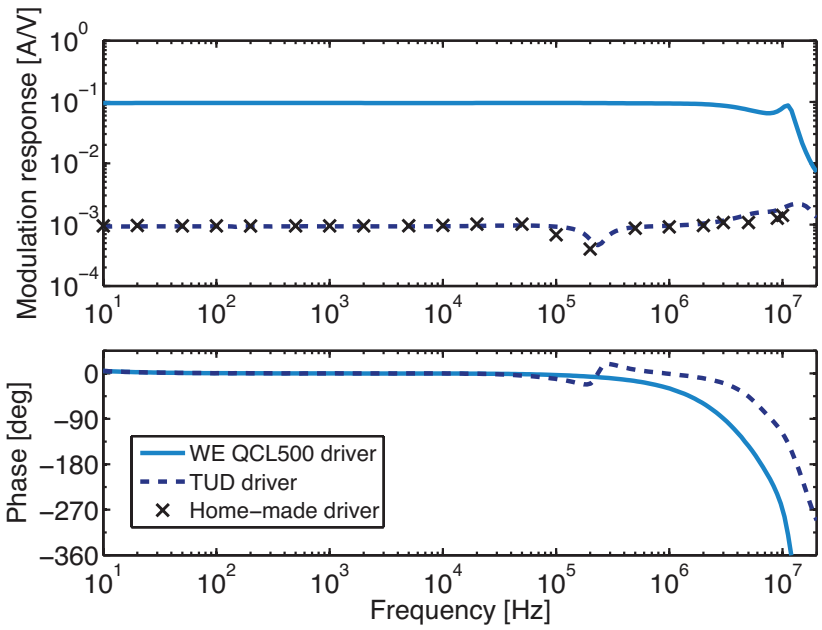

Figure 4.4: Current modulation responses in magnitude and phase of different QCL current controllers.

4.2 Measurement of mid-IR frequencies

4.2.1 Molecular spectroscopy of carbon monoxide

The frequency of the QCLs is measured using a molecular absorption line at low pressure acting as an optical frequency discriminator [49–52]. Carbon monoxide (CO) is used in our set-up as a result of the good spectral overlap between the QCL emission wavelength $\lambda = 4.6$ µm and the fundamental (0-1) vibrational band of CO. With a proper adjustment of the laser temperature, the laser wavelength coincides with the R(14) ro-vibrational transition of CO at 2196.6 cm^{-1}.

Owing to the strong absorption of the CO fundamental vibrational band (the linestrength of the R(14) line is $2.01 \cdot 10^{-19}$ $cm^{-1}/(molecule\ cm^{-2})$), a single pass absorption cell with a pathlength as short as 1 cm is sufficient to produce a large absorption. Figure 4.5 (a) shows a simulation of the transmission through a 1 cm long cell at different CO pressures. Spectroscopic parameters from HITRAN2008 database [133] have been used to compute the CO Voigt lineshape. For faster computation, the analytical approximation of the Voigt profile given by Whiting [134] has been used.

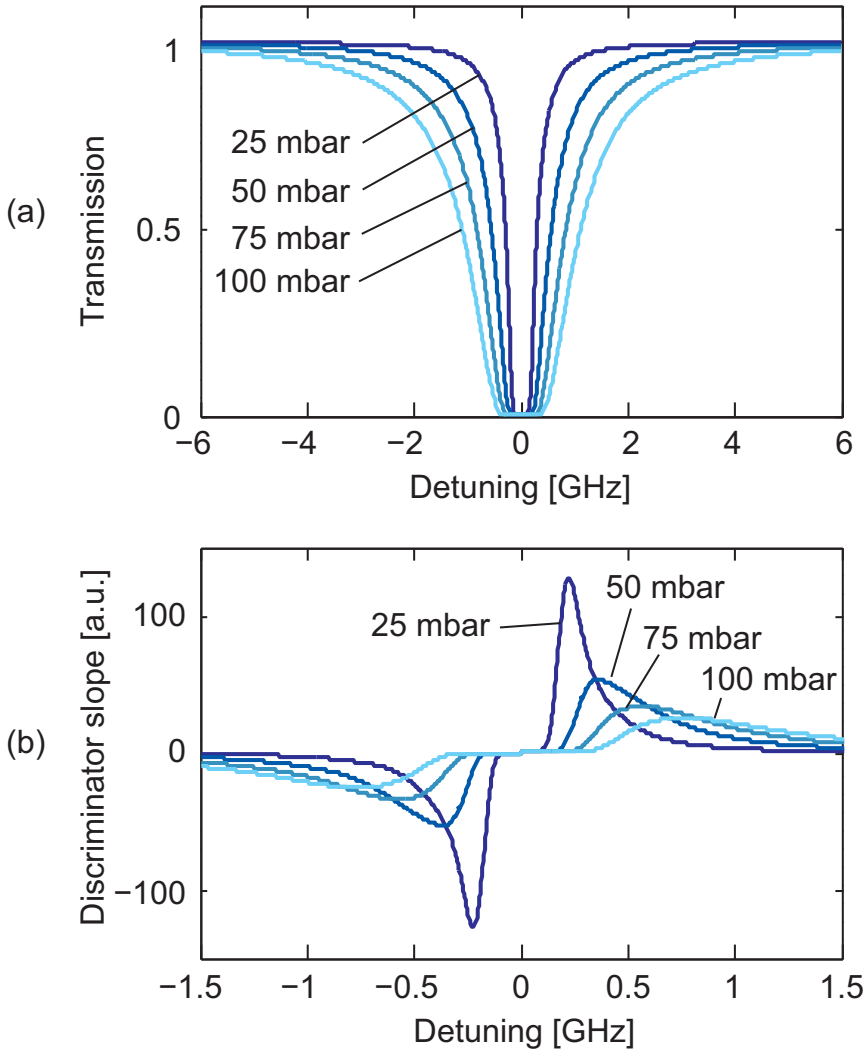

Figure 4.5: (a) Simulated transmission for the R(14) absorption line of CO at 2196.6 cm^{-1} through a 1 cm long cell filled with pure CO for various pressures. (b) Corresponding frequency-to-amplitude conversion factor.

From the computed transmission curves, the frequency-to-amplitude conversion factor, which is also referred to as the discriminator slope, has been determined as a function of the laser detuning (Figure 4.5 (b)). The maximum discriminator slope is achieved in the steepest part of the CO transmission curve. Figure 4.6 (a) shows how the cell filling can be optimized to maximize the discriminator slope. The optimal CO pressure is 6 mbar for a 1 cm long cell.

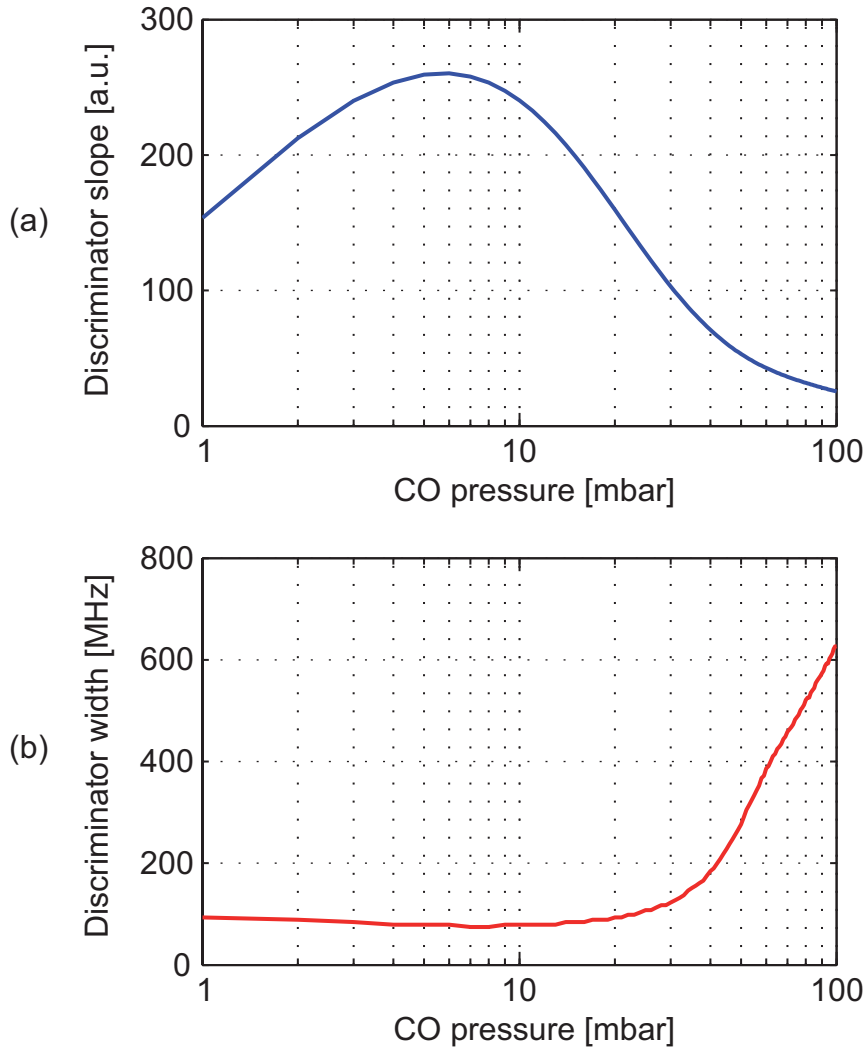

Figure 4.6: (a) Discriminator slope corresponding to the R(14) absorption line of CO as a function of the gas pressure (1 cm gas cell filled with pure CO). (b) Spectral width (defined at 10% of the peak value) of the CO frequency discriminator as a function of the CO pressure.

4.2.2 Frequency-noise measurement setup

The experimental set-up used for the measurement of frequency-noise of QCLs is shown in Figure 4.7. The QCL beam is collimated with an aspheric ZnSe lens and propagates through a 1 cm long gas cell filled with pure CO. The cell pressure was generally on the order of 20 mbar in our experiments. This is larger than the optimal pressure of 6 mbar determined from Figure 4.6 (a). However, the flank of the CO line remains steep enough to

provide a sufficient frequency-to-intensity conversion even at high Fourier frequencies.

The laser is tuned to the flank of the CO absorption profile, where the frequency fluctuations are converted into intensity fluctuations by the frequency-dependent transmission. After the cell, another ZnSe lens focuses the transmitted light onto a low-noise liquid-nitrogen-cooled HgCdTe detector (Kolmar Technologies MPV11, 20 MHz bandwidth). The detector signal, which is a direct image of the QCL frequency variations, is analyzed with an FFT spectral analyzer (Stanford Research System SRS770) for low Fourier frequencies (up to 100 kHz) and with an electrical spectrum analyzer (ESA), model Agilent E4407B, at higher frequencies.

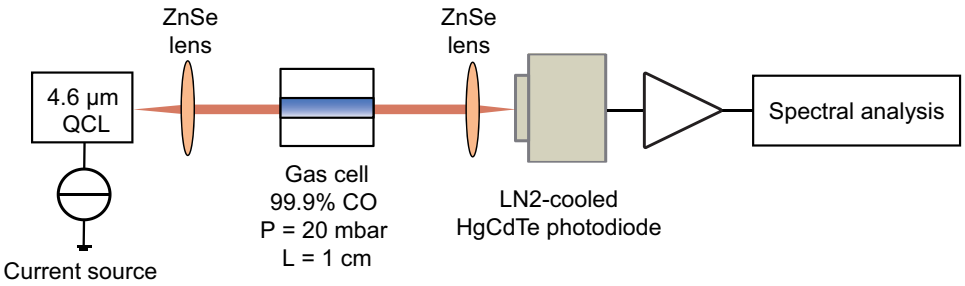

Figure 4.7: Frequency-noise measurement setup based on single-pass absorption spectroscopy of carbon monoxide (CO).

In order to achieve a good spectral resolution over the entire considered frequency range, each measured spectrum is obtained from the combination of several FFT and ESA spectra taken for each frequency decade. The frequency-noise PSD is then obtained using the conversion factor given by the discriminator slope, which is determined from the transmission obtained by scanning the laser through the CO line. Typical values of 20-30 mV/MHz are obtained with this setup.

The measured absorption profile of carbon monoxide when the laser is scanned through the line (here R(14)) is shown in Figure 4.8. The frequency axis was calibrated using a Fabry-Perot (1 GHz FSR) reference cavity in order to assess the frequency excursion of the QCL. The experimental results (solid line) are in very good agreement with the simulated spectrum (crosses) from the HITRAN database. The inset of Figure 4.8 shows a zoom on the linear region of the absorption line as well as a linear fit of the data. An excellent linearity can be observed over more than 100 MHz which guarantees a constant frequency-to-intensity conversion in this frequency range.

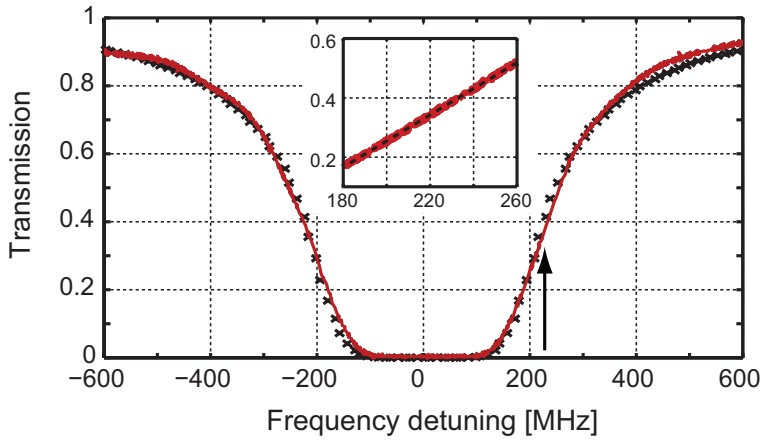

Figure 4.8: Experimental (solid line) and simulated (crosses) absorption profile of carbon monoxide R(14) line (99.9% CO, 20 mbar, 1 cm path length) as a function of the detuning from the line center (2196.6 cm^{-1}). The arrow represents the laser operating point. Inset: zoom on the linear region and linear fit (dashed line).

4.3 Frequency-noise of 4.6 μm QCLs at room temperature

4.3.1 Results from molecular absorption line

The first measurements were carried out with a DFB ridge-waveguide QCL provided by Alpes Lasers SA emitting at 4.6 μm in CW at room temperature (sbcw2689). The QCL was mounted on a thermo-electric cooler and was operated at 278 K with a drive current $i_0 = 350$ mA ($i_{th} = 300$ mA).

The frequency-noise PSD of this device is shown in Figure 4.9. It reveals the presence of $1/f$ (or flicker) noise all the way up to 10 MHz, with a noise level of 10^7 Hz^2/Hz at 1 kHz and below 100 Hz^2/Hz at 10 MHz. The contribution of the laser intensity noise and the contribution of the laser driver are also shown in Figure 4.9.

The contribution of the intensity noise was measured by tuning the laser off resonance and the contribution of the current driver noise was obtained by combining its current noise spectrum with the dynamic response of the laser shown in Chapter 3. Figure 4.9 shows that neither the laser intensity noise nor the laser driver contributions limit the measured frequency noise at Fourier frequencies below 100 kHz, which can thus be attributed to the laser itself. The cut-off observed in the contribution of the laser

driver above 100 kHz corresponds to the bandwidth of the laser frequency dynamic response (see Chapter 3).

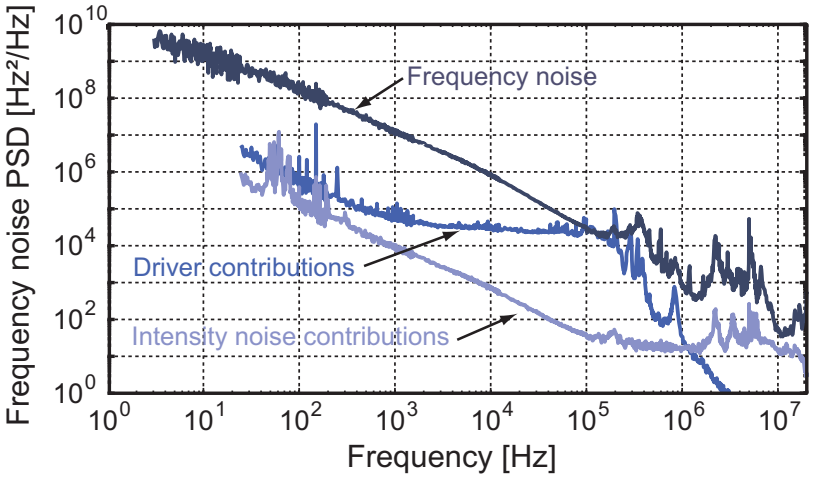

Figure 4.9: Frequency-noise PSD of a 4.6 µm distributed-feedback QCL operated at 283 K in CW. The contributions of the driver current noise and intensity noise are shown as well.

At higher Fourier frequencies, the measurement is affected by additional technical noise, also present in the intensity noise spectrum. This excess noise is very likely induced by the current driver, whose noise contribution was evaluated on a resistive load and can behave differently on the QCL capacitive load. Despite this excess technical noise, the laser frequency noise decreases significantly all the way up to 10 MHz. Moreover, the general trend seems to change from the $1/f$ slope observed at low frequency into a steeper slope above 10 kHz. A transition to $1/f^2$ has been reported as well for a 4.33 µm QCL operated at cryogenic temperature [51] and attributed to the thermal cut-off in the laser structure [126].

Although the measurement is limited by the detector bandwidth of 20 MHz and the white frequency-noise level cannot be clearly observed in the measurement, an upper limit of 100 Hz^2/Hz can be inferred from Figure 4.9. This quantity is directly related to the intrinsic linewidth of the laser, arising from quantum noise, and will be discussed in more details in Section 4.3.4.

A second ridge-waveguide QCL from the same fabrication and operating in slightly different conditions ($i_0 = 400$ mA, $T_0 = -5°\text{C}$) was also characterized and yielded very similar results.

4.3.2 Results from Fabry-Perot interferometer

The frequency-noise spectra obtained through the molecular frequency discriminator were validated using a second measurement method. A 15 cm long Fabry-Perot interferometer (1 GHz FSR) was used as a frequency-to-intensity converter. The inset of Figure 4.11 shows the transmission profile of the interferometer which was measured by scanning the QCL frequency. A 5 MHz full width at half maximum (FWHM) linewidth can be inferred for the Fabry-Perot cavity, which corresponds to a finesse $\mathcal{F} = 200$.

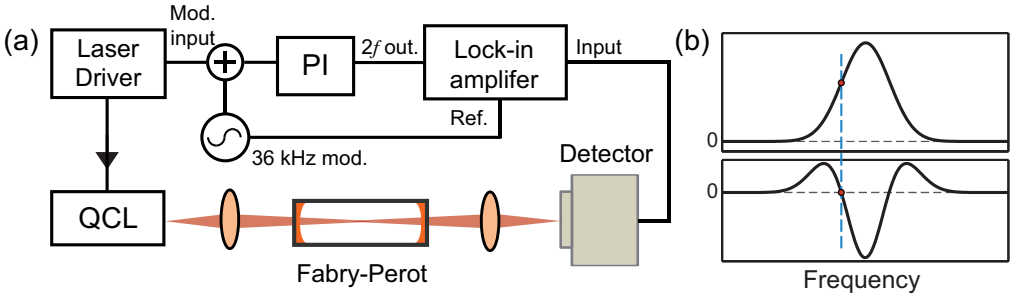

Figure 4.10: (a) Frequency-noise measurement setup with a Fabry-Perot interferometer and $2f$ detection scheme ($f_m = 36$ kHz). (b) Diagram of the Fabry-Perot transmission (top) and $2f$ signal (bottom) showing the locking point (red dot).

Because of the relatively narrow resonance, a slow feedback loop was implemented in order to compensate any temperature drift of the laser relative to the interferometer and keep the QCL frequency tuned to the side of the resonance during the measurement time. This was implemented using wavelength modulation at $f_m = 36$ kHz and demodulation of the 2^{nd} harmonic of the transmitted signal with a lock-in amplifier (1 s time constant). This signal cancels out at the resonance flank and was used as an error signal for the slow stabilization. Side-of-fringe locking could not be used in this case because of the AC-coupling of the detector.

The resulting frequency-noise spectrum is shown in Figure 4.11. Except the peak at 36 kHz, which is due to the modulation applied for the slow stabilization, the experimental results are in very good agreement with the frequency-noise PSD measured with the CO frequency discriminator (Figure 4.9). Below 100 kHz, $1/f$-type noise is dominant and reaches $10^7 \text{Hz}^2/\text{Hz}$ at 1 kHz as well. Above 100 kHz, a transition to a steeper slope is also observed and is very likely due to a thermal filtering of the noise generation processes [126].

The cut-off frequency of the detector (Teledyne Judson J15D) can be observed above 1 MHz and this set of data is not exploitable at high frequencies. Moreover, it is important to point out that the cut-off frequency of the Fabry-Perot cavity is on the order of 2.5 MHz (FWHM/2) and does not affect the frequency-noise measurement in the considered frequency range.

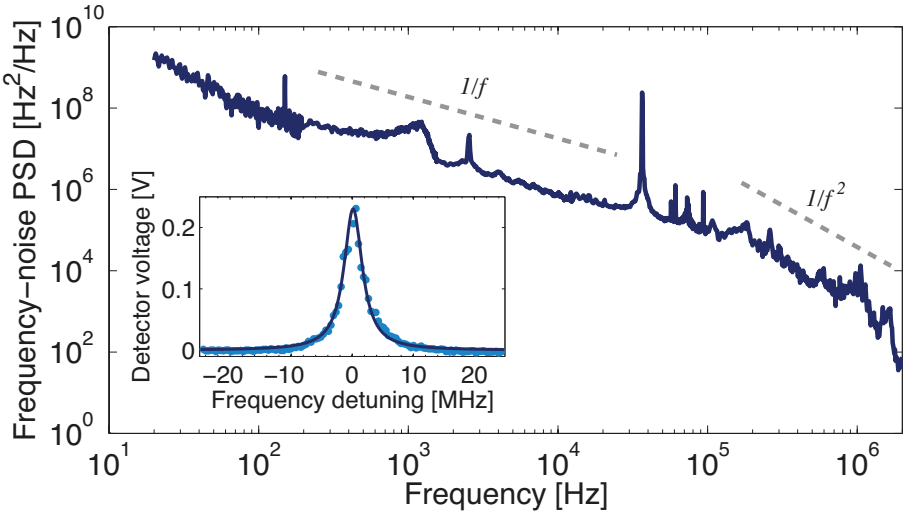

Figure 4.11: Frequency-noise PSD measured with a Fabry-Perot interferometer. Inset: transmitted signal through the Fabry-Perot interferometer (dots) and fit to a Voigt profile (solid line).

4.3.3 Calculated and experimental linewidths

Figure 4.12 shows the heterodyne beat signal between two DFB-QCLs recorded over a 4 ms sweep time. The beat signal was obtained with the same ridge-waveguide DFB QCL used for the frequency-noise measurements of section 4.2.2 and another similar device from the same fabrication run. The beams of the two QCLs were collimated, combined using a 50-50 beam-splitter and focused on a fast photodetector (1 GHz bandwidth).

The FWHM linewidth of the beat signal, which represents the convoluted linewidth of the two QCLs, is on the order of 1 MHz. The inset of Figure 4.12 shows the FWHM linewidth of one QCL calculated from the experimental frequency-noise spectrum using the formalism described in Chapter 2 [66] as a function of the observation time. A linewidth of 550 kHz

is found for an observation time of 4 ms, which is in very good agreement with the beat signal spectrum.

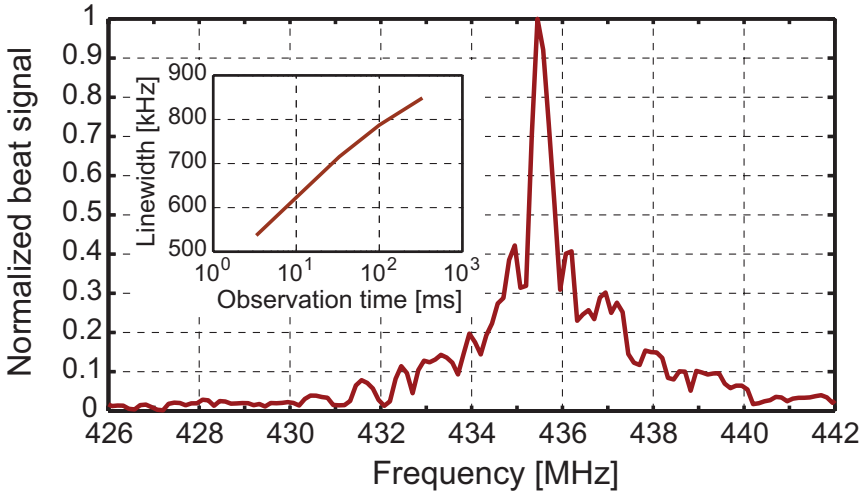

Figure 4.12: Heterodyne beat signal (FWHM linewidth of 1 MHz) between two identical room-temperature 4.6 µm distributed-feedback QCLs (4 ms sweep time). Inset: FWHM linewidth calculated from the frequency noise spectrum versus observation time.

4.3.4 Schawlow-Townes linewidth

The intrinsic linewidth, or Schawlow-Tones limit given by Eq. 4.3 [55, 59], is directly related to the laser white frequeny-noise component S_w by $\Delta\nu_{ST} = \pi S_w$ [62].

$$\Delta\nu_{ST} = \frac{v_g^2 h\nu n_{sp}\alpha_{tot}\alpha_m(1+\alpha^2)}{4\pi P_0} \tag{4.3}$$

As mentioned in Chapter 3, the linewidth enhancement factor α is close to zero in QCLs and notably lower than in other semiconductor lasers (typical value in the range 2-10 [135]). Theoretical considerations about the intrinsic linewidth in QCLs have also led to the modified Schawlow-Townes formula introduced by Yamanishi and co-workers [136].

The Schawlow-Townes linewidth can be computed from Eq. 4.3 where the total losses α_{tot} (mirror and waveguide losses) and the mirror losses α_m must be known. While the total losses can be straightforwardly determined in a Fabry-Perot laser, this is not the case in a DFB laser as the

reflectivity along the entire grating (α_{DFB}) has to be accounted for. In order to estimate the total losses in our DFB, its threshold current was compared to the one of a similar Fabry-Perot device. Assuming similar waveguide losses $\alpha_{wg} = 4.5$ cm^{-1} in both cases (measured by the manufacturer on Fabry-Perot devices) and using typical values of the laser parameters provided by the manufacturer, the losses of the grating are estimated to $\alpha_{DFB} = 1.47$ cm^{-1}. The estimated losses are in good agreement with literature data [137] for a 9 µm QCL ($\alpha_{wg} = 6.7$ cm^{-1}, $\alpha_{DFB} = 0.7$ cm^{-1}).

Assuming a spontaneous emission coefficient $n_{sp} = 1$, an optical power $P_0 = 6$ mW and $\alpha = 0$, an intrinsic linewidth $\Delta\nu_{ST} = 380$ Hz is calculated. This result is on the order of the value obtained from the upper limit of white frequency-noise $S_w \approx 100$ Hz^2/Hz (see Figure 4.9), yielding an intrinsic linewidth $\Delta\nu_{ST} = \pi S_w = 320$ Hz, and similar to the intrinsic linewidth reported for a cryogenic QCL at 4.33 µm [51] and a room-temperature device at 4.36 µm [124].

4.4 Impact of the driving electronics

This section treats the impact of the driving electronics noise on the spectral properties of QCLs. As discussed before, sub-MHz linewidths can be achieved for QCLs in the 4-5 µm range. However, these results were obtained with low-noise current drivers (home-made solution of Section 4.1

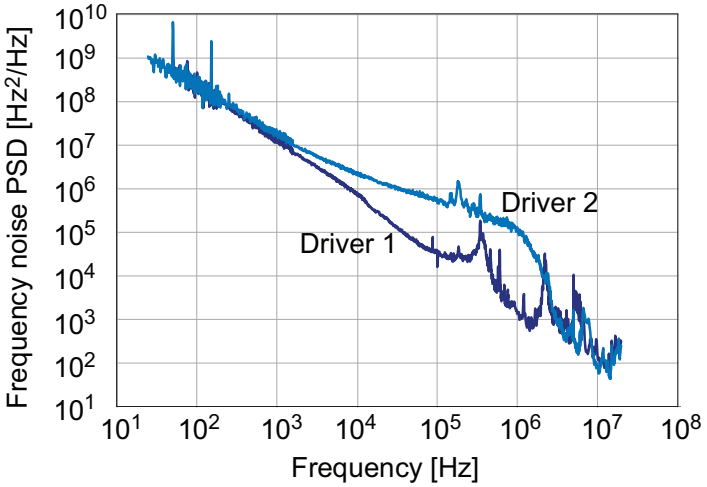

Figure 4.13: Frequency-noise PSD measured with different current-noise spectral densities of 350 pA/Hz$^{1/2}$ (Driver1) and 2 nA/Hz$^{1/2}$ (Driver2).

showing a current noise lower than 350 pA/Hz$^{1/2}$, labeled Driver1 here) and the picture is very different in case noisy electronics is used. As shown in Figure 4.13, when a noisier current is used to supply the QCL (modified interband laser diode controller with a current noise of $\approx$ 3nA/Hz$^{1/2}$, labeled Driver2), the additional noise induces fluctuations of the laser chip temperature, and therefore of the optical frequency. The white current noise is filtered by the dynamic response of the QCL (Chapter 3) with a tuning coefficient of 900 MHz/mA at low frequency, and results in an increase of the frequency-noise PSD. The thermal cut-off can be observed above a few hundreds kHz and both frequency-noise PSDs finally tend to the same value above 3 MHz.

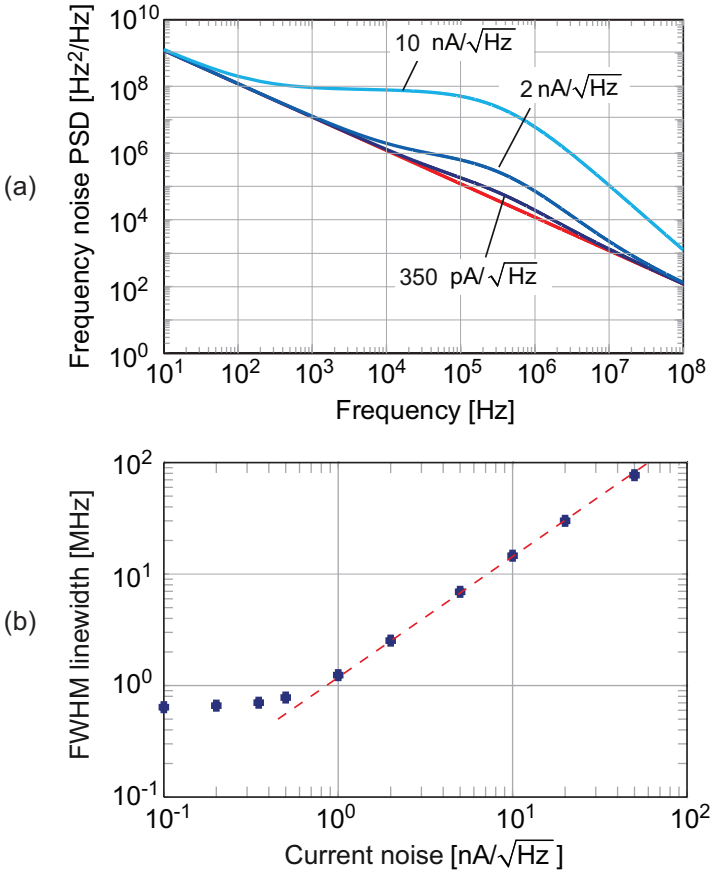

Figure 4.14: (a) Simulation of the laser frequency noise corresponding to different current noise spectral densities (white current noise is considered). The red curve represents the $1/f$ modeled frequency noise of the QCL. (b) Calculated laser linewidth (FWHM) as a function of the driver current noise spectral density.

The increase of the QCL frequency noise due to the current noise leads to a broadening of the laser linewidth. In the present case, the laser linewidth broadens from 550 kHz (Driver 1) to 2 MHz (Driver 2) for an observation time of 5 ms. While the linewidth broadening is rather moderate in that case, it can become dramatic for laser drivers with a higher current noise. Based on the formalism of Section 2.2.3 [66], the broadening of the QCL linewidth was calculated as a function of the current noise. The contribution of different levels of white current noise was added to the modeled $1/f$-like frequency noise PSD (10^7 Hz^2/Hz at 1 kHz) using a frequency tuning coefficient of 900 MHz/mA and a thermal cut-off frequency of 100 kHz. The results are shown in Figure 4.14 (a). These results are in good agreement with the experimental spectra of Figure 4.13.

The dependence of the FWHM linewidth on the current noise spectral density is shown in Figure 4.14 (b) for an observation time of 10 ms. While the linewidth is almost not affected for current noise densities lower than 1 nA/Hz$^{1/2}$, it drastically broadens for larger current noise, at a rate of 1.6 MHz/(nA/Hz$^{1/2}$). The calculated linewidth reaches for instance almost 100 MHz for a current noise density of 50 nA/Hz$^{1/2}$. These results illustrate how a noisy laser driver can deteriorate the linewidth of a QCL and show that great care must be taken if a narrow-linewidth emission is required.

4.5 State-of-the-art

4.5.1 Free-running mid-IR QCLs

A few other frequency noise measurements of QCLs in the 4-5 µm range have been reported in the literature and are listed in Table 4.2. Bartalini et al. reported the frequency noise and intrinsic linewidth of a distributed-feedback QCL operated at cryogenic temperature (85 K) and emitting at 4.33 µm [51] (supplied by Alpes Lasers). A gas cell filled with CO_2 was used as a frequency discriminator.

Then we reported the frequency-noise spectrum of DFB-QCLs operated at room-temperature [52] (outcome of this chapter). Surprisingly, the frequency noise of these two lasers was two orders of magnitude lower than the one of the cryogenic QCL of Ref. [51], leading to a one order of magnitude narrower linewidth.

Our observation of a sub-MHz free-running linewidths with room temperature devices was followed by a similar result reported by Bartalini

Ref	λ [µm]	Grating	T_{op} [K]	FWHM	Supplier
[51]	4.33	DFB	85	7 MHz	Alpes Lasers
[52]	4.55	DFB	277	0.6 MHz	Alpes Lasers
[124]	4.36	DFB	288	0.4 MHz	Hamamatsu
[138]	4.48-4.55	DFB	128-303	0.8 - 10 MHz	Alpes Lasers
[139]	4.5	EC		4 MHz	Daylight Solutions

Table 4.2: Overview of FWHM linewidths reported in literature for QCLs emitting in the 4-5 µm range ($\tau_{obs} = 1 - 10$ ms)

and co-workers for another DFB-QCL at 4.36 µm [124], also operated at room-temperature, but produced in this case by Hamamatsu Photonics. Figure 4.15 shows the frequency noise spectra of the three aforementioned DFB-QCLs in the Fourier frequency range from 10 Hz to 100 MHz. Except a few parasitic spikes of technical origin, all the spectra show a global trend that is governed by $1/f$ noise. The level of noise is very similar for the two room-temperature devices, but two orders of magnitude higher for the cryogenic QCL. At higher frequencies, the three lasers seem to reach a similar white frequency noise floor.

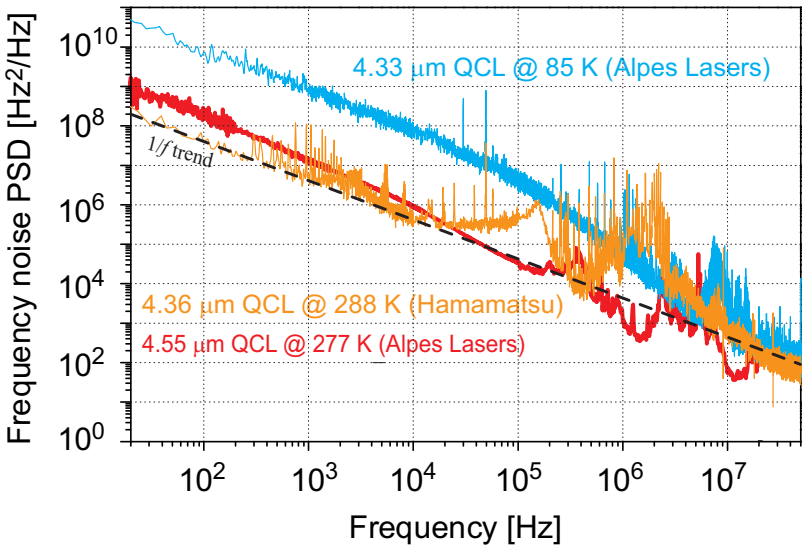

Figure 4.15: Frequency-noise PSD of different mid-IR distributed QCLs in the 4-5 µm range [51, 52, 124].

Despite the large difference of frequency-noise suggesting a possible important influence of temperature on the spectral properties of QCLs, it is at that point difficult to draw conclusions based on these results and take into consideration the intrinsic differences between the devices. The influence of other parameters such as the dimensions, design and fabrication process cannot be ruled out. The temperature dependence of the frequency noise using a single QCL was investigated in a broad temperature range and is described in the next chapter.

Besides single-mode distributed-feedback QCLs, the frequency-noise properties of an external cavity QCL (EC-QCL) at 4.5 μm were also investigated using spectral analysis of the beat signal between the QCL and an optical frequency comb [139,140]. As for the previous results, $1/f$ noise was found to dominate the noise processes. The associated linewidth of 4 MHz is significantly broader than the best results obtained with distributed-feedback QCLs.

4.5.2 Comparison to interband laser diodes

Spectral properties of interband DFB laser diodes have been extensively investigated in the near-IR spectral region during the 80's, and especially for CW AlGaAsP DFB lasers emitting in the telecom bands at 1.3 and 1.5 μm. Although early measurements have shown linewidths ranging from $\approx$ 10 MHz [141, 142] up to more than 100 MHz [143], DFB lasers diodes at 1.3 and 1.5 μm with sub-MHz linewidths have been reported in numerous studies [119, 144–148].

The effect of various parameters of the lasers on the spectral properties was studied. The linewidth of multiple quantum-well (MQW) InGaAsP diode lasers was for instance shown to broaden with the number of quantum wells [147]. Sub-MHz linewidhts were also demonstrated using gratings with strong coupling constants κL [148] and nonuniform current injection [146]. The effect of the grating location in DBR laser diodes was investigated and yielded linewidths ranging from below 1 MHz up to 15 MHz [149]. More recently, the spectral properties of high-power semiconductor lasers diodes at 1310 nm [150], 1064 nm [151] and 974 nm [152] were reported and showed again emission linewidths in the MHz range.

$1/f$ noise was also found to be the source of linewidth broadening in interband semiconductor lasers [60, 61]. Several correlation measurements between intensity and frequency fluctuations have been carried out [153–156] and will be discussed in details in Chapter 5.

Regarding mid-IR interband semiconductor lasers, spectral properties of lead salt lasers were also investigated in the past, and the results are generally much less promising than near-IR lasers diodes and mid-IR QCLs. Linewidths ranging from a few MHz up to 500 MHz were measured for a set of Pb-salt lasers emitting in the 8 to 9 µm spectral region [157]. The linewidth was reported to drastically vary from device to device and showed an important dependence on the operating conditions. In addition, up to 25 MHz linewidths were reported for others PbSnTe laser diodes at 5.4 µm [158] and 7.9 µm [159], respectively. Moreover, the mechanical vibrations due to the required cryo-coolers were found to lead to further linewidth broadening, well beyond the inherent properties of the lasers [160, 161].

According to the above considerations and outcomes of the experiments presented in this chapter, room-temperature QCLs are not only more convenient to use than lead-salt lasers at cryogenic temperature, but they also show much better spectral properties when operated in proper conditions, and therefore represent a very interesting source of light in the mid-IR for high-precision measurements applications. Last but not least, it is also important to emphasize the fact that the spectral properties of QCLs reported in this chapter can compete with state-of-the-art results obtained from interband semiconductor laser diodes emitting in the telecom band.

It is also instructive to add that some methods aiming at reducing frequency noise in near-IR laser diodes have been implemented using compact or integrated passive elements. A first method consists in self-injection locking of the laser emission frequency to a high quality factor whispering gallery mode resonator. An emission linewidth as narrow as 200 Hz was demonstrated with a 1550 nm DFB laser diode using optical feedback from a high-Q CaF_2 microresonator [162]. Excellent spectral properties in the kHz range at 1542 nm were also achieved using a long planar waveguide Bragg reflector separated from the semiconductor gain media [163]. Both techniques yielded excellent performances, are extremely compact and their extension to QCLs might lead to very interesting prospects.

Chapter 5

Origin of frequency instabilities in mid-IR QCLs

This chapter discloses various measurements and results aiming at gaining a better understanding on the frequency noise generation processes in QCLs, as well as the influence of operating conditions and devices parameters on the frequency instabilities.

In a first phase, the effect of temperature, laser structure and thermal resistance on the spectral properties of single-mode mid-IR QCLs is assessed. Frequency-noise of a couple of devices with different structures and dimensions was measured over a broad temperature range. In a second phase, noise processes at the electrical level are investigated in order to gain a deeper insight about the frequency noise generation mechanisms.

5.1 Temperature dependence of frequency-noise

A surprising outcome of Chapter 4 is that room temperature devices [52, 124] showed a considerable reduction of two orders of magnitude in terms of frequency noise power spectral density (PSD) compared to a cryogenic QCL operating at a close wavelength [51]. All these works dealing with frequency noise of QCLs at different temperatures were carried out with different devices, making difficult the assessment of the impact of temperature because of the possible influence of other parameters such as the different designs, dimensions and fabrication processes of the lasers. In contrast to previous works, frequency-noise of a single QCL was investigated from room temperature down to cryogenic temperature. We were therefore able to measure for the first time the frequency noise of the same device over a wide temperature range from 128 K to 303 K.

5.1.1 Experimental setup

Frequency noise measurements were performed the same way as in Chapter 4 and Refs. [50–52, 124, 164] with the QCLs tuned to the side of a molecular absorption line acting as a frequency-to-intensity converter, also referred to as a frequency discriminator. The output radiation of the laser was collimated and traversed a 1 cm long gas cell filled with pure carbon monoxide (CO) at a nominal pressure of ≈ 20 mbar. The transmitted light was detected with an HgCdTe photodiode (Kolmar Technologies MPV11). After amplification, the output voltage fluctuations were analyzed with a Fast-Fourier Transform (FFT) analyzer. The measured slope of the absorption line around the laser operating point was used to convert the recorded detector voltage into laser frequency noise. The main purpose of the study was to explore the temperature dependence of low-frequency flicker noise of the laser. For this reason, the measurements were restricted to Fourier frequencies below 100 kHz.

The laser used in this first experiment is a buried-heterostructure DFB-QCL, emitting at 4.55 µm. The QCL was mounted epi-side up in a cryostat so that stable and controlled operation was achieved from 128 K to 303 K, with threshold currents i_{th} ranging from 75 mA to 120 mA. The operating current spanned from 110 mA to 180 mA with an optical output power in the 10-20 mW range. The low-noise current source developed at TU-Darmstadt (see Section 4.1) was used to drive the laser, which has a

sufficiently low current noise so that its contribution to the QCL frequency noise was negligible in the considered frequency range. The laser temperature could not be lowered below 128 K because of the increasing voltage across the QCL at low temperature, which exceeds the compliance voltage of the low-noise current driver ($\approx$ 15 V).

All frequency-noise measurements were performed approximately 50% above the threshold current, i.e. for drive currents $i_0 \approx 1.5\ i_{th}$. The operating current and temperature were therefore carefully selected in order to tune the laser wavelength to a CO absorption line. A QCL showing a good coverage of CO R-branch all over the temperature range was selected, in order to be able to match a transition at each operating temperature. Different ro-vibrational transitions ranging from R(15) to R(24) were used with weakening absorption as the laser temperature was lowered, as shown in Figure 5.1. From ≈ 2200 cm^{-1} at room temperature, which lies close to the center of CO R-branch, the laser frequency shifts up to ≈ 2230 cm^{-1} at low temperature. At the same time, the absolute absorption and the slope of the frequency discriminator decrease.

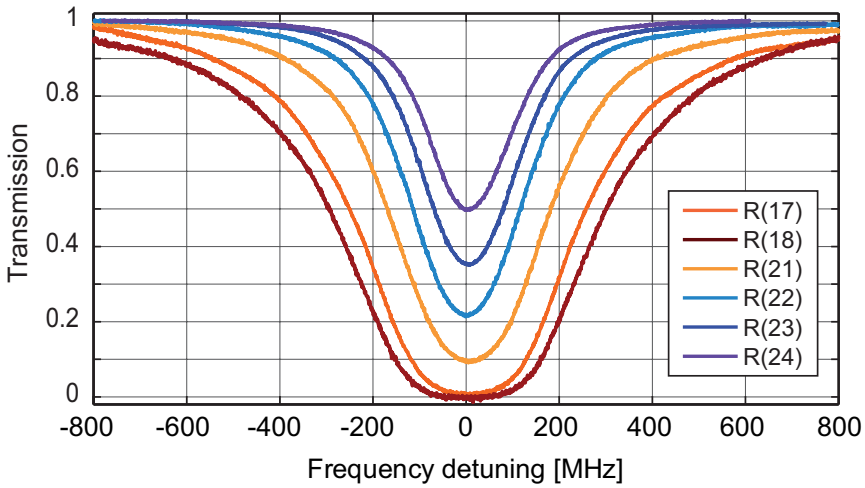

Figure 5.1: Transmission spectra corresponding to various ro-vibrational transitions in the R-branch of the fundamental ($0 \rightarrow 1$) CO vibrational band (20 mbar of pure CO through 1 cm pathlength).

For a proper determination of the laser frequency noise, the discriminator slope needs to be accurately determined for each CO absorption line. As in Chapter 4, the frequency axes of the spectra were carefully calibrated at each respective temperature using a Fabry-Perot analyzer.

The QCL emission spectrum was also measured with a Fourier Trans-

form Infrared (FTIR) spectrometer over the entire temperature range, in order to check that the laser was always operated singlemode without any mode hop. All frequency noise measurements were performed under these conditions, with the same lasing mode analyzed from room temperature down to cryogenic temperature.

5.1.2 Frequency-noise spectra

Typical frequency noise spectra measured in the study are shown in Figure 5.2 for different temperatures of 128 K, 155 K, 178 K, 223 K, 263 K, and 283 K. As in previous works, $1/f$ (or flicker) noise is observed from low frequencies up to 100 kHz at each temperature. While the frequency noise spectra are almost unchanged in the high temperature range (201-283 K), the noise strongly increases at lower temperature and is enhanced by almost two orders of magnitude in terms of PSD at 128 K.

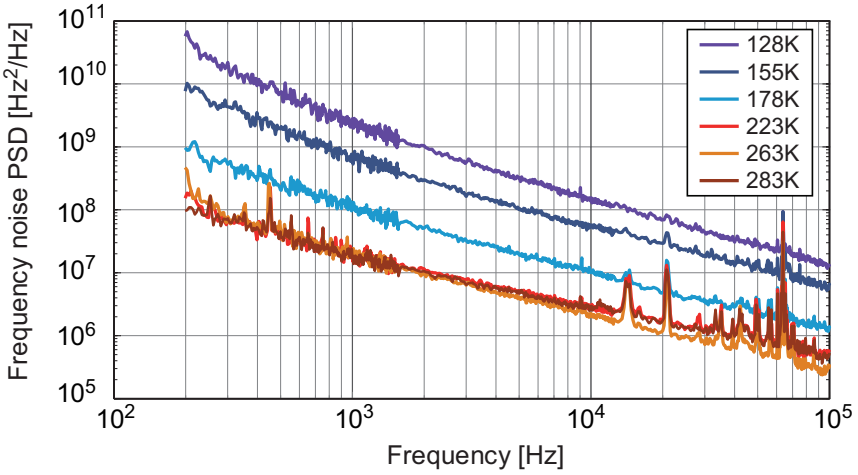

Figure 5.2: Frequency noise PSD of a 4.55 µm buried heterostructure DFB-QCL measured at different temperatures ranging from 128 K to 283 K. The laser operating current is in the range 120-180 mA and was adjusted to $i_0/i_{th} \approx 1.5$ at each temperature.

Although all the measurements were initially performed at $i_0/i_{th} \approx 1.5$, the dependence of frequency noise upon drive current was also investigated. As the laser frequency needs to be always tuned to a particular CO transition for the frequency noise measurements, the drive current could not be simply changed at a fixed heat-sink temperature. However, a small temperature decrease of only 1 K is sufficient to keep the laser tuned to

a transition when the current is increased by about 10 mA. Owing to the low threshold current of our laser, it is possible to change the i_0/i_{th} ratio whereas the temperature excursion remains small, in the range of a few Kelvins. No significant dependence on the drive current was found for different values of i_0/i_{th} ranging from ≈ 1.2 to ≈ 1.8. All over the temperature range, no influence of the drive current onto the laser frequency noise was observed beyond the measurement uncertainty, which is by the way negligible compared to the strong noise increase observed at low temperature. However, owing to the relatively low current threshold of this QCL, the current excursions between $1.2i_{th}$ and $1.8i_{th}$ are relatively small in that case (e.g. 120 mA to 180 mA at 283 K) and we will see later that the picture can be different over a broader range of currents.

The frequency noise PSD at a Fourier frequency of 3 kHz, S_{3kHz} is shown as a function of temperature in Figure 5.3. From the experimental data, two different regimes are observed for the temperature dependence of frequency noise, with a transition around 200 K. Above 200 K, the frequency noise PSD is almost independent of temperature, at a level slightly below 10^8 Hz^2/Hz. On the other hand, the laser frequency noise drastically increases when the temperature is lowered below 200 K, with an exponential dependence with respect to temperature, $S_{3kHz} \approx 2 \cdot 10^{12}\ e^{0.06T}$. A level of $7 \cdot 10^8$ Hz^2/Hz is reached at 128 K.

These results are comparable to previous data reported at corresponding temperatures for different QCLs emitting at close wavelengths. At room-temperature, the data are on the same order as the results obtained in Chapter 4 with a ridge-waveguide QCL from Alpes Lasers SA emitting at the same wavelength ($T = 277$ K, $i_0 = 350$ mA) [52] as well as to the values reported for a different QCL from Hamamatsu Photonics emitting at a slightly shorter wavelength of 4.36 µm ($T = 288$ K, $i_0 = 776$ mA) [124]. The same agreement applies at cryogenic temperature even though we could not reach the temperature used with the cryogenic 4.33 µm QCL of Ref. [51] ($T = 85$ K, $i_0 = 219$ mA). At this point, it is important to emphasize the fact that frequency noise is reported here as a function of the cryostat or laser heat-sink temperature, but the actual temperature in the laser active region is higher due to thermal dissipation. As a consequence, the internal temperature of our device is very likely closer to the heat-sink temperature than for the cryogenic QCL of Ref. [51], because of the lower operating current. If the noise was plotted in Figure 5.3 as a function of the internal temperature, the value of the cryogenic QCL would become closer to our point at the lowest temperature.

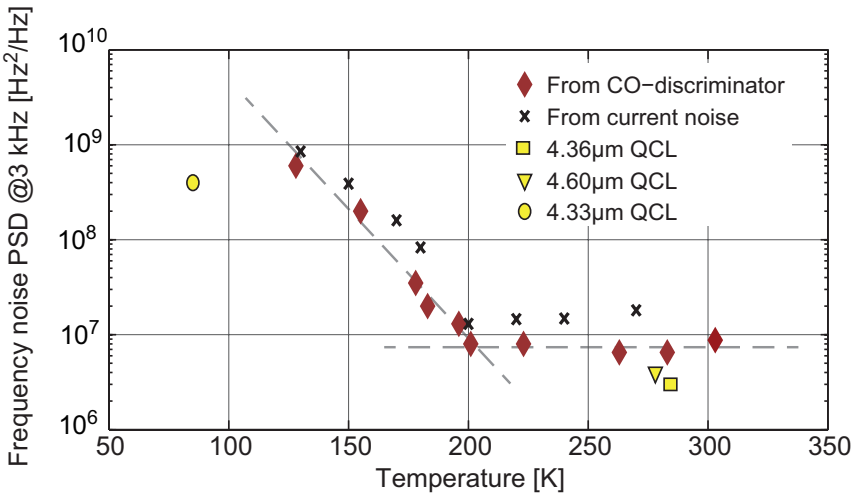

Figure 5.3: Temperature dependence of the frequency noise PSD of a buried-heterostructure QCL measured at 3 kHz Fourier frequency (red diamonds). The black crosses represent the noise measured on the voltage across the laser, converted into an equivalent frequency. The yellow markers represent published values of frequency noise obtained with different QCLs at 4.33 µm [51], 4.6 µm [52] and 4.36 µm [124].

5.1.3 Linewidth

Figure 5.4 shows the corresponding laser FWHM linewidth computed from the frequency noise spectra using the formalism presented in Chapter 2. From ≈ 770 kHz at high temperature, the linewidth follows the frequency noise increase and broadens up to ≈ 10 MHz at 128 K (at 5 ms observation time).

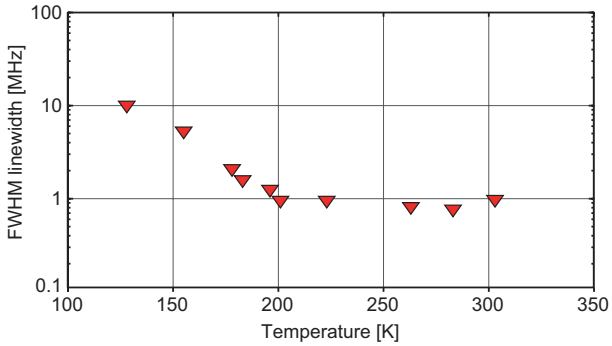

Figure 5.4: Calculated linewidth as a function of temperature (5 ms observation time).

5.1.4 Electrical noise conversion

In order to have a deeper insight into the frequency noise increase at temperatures below 200 K, the voltage noise across the QCL was measured as a function of temperature. The measured voltage noise PSD was converted into current noise using the corresponding laser differential resistance. Typical spectra are shown in Figure 5.5. First of all, it is important to emphasize that this noise denotes the same $1/f$ nature as the measured frequency noise and also shows a drastic increase at temperatures below 200 K. It is important to note here that the noise of the current driver ($\approx$ 350 pA/Hz$^{1/2}$) lies well below and does not contribute to the current noise reported here.

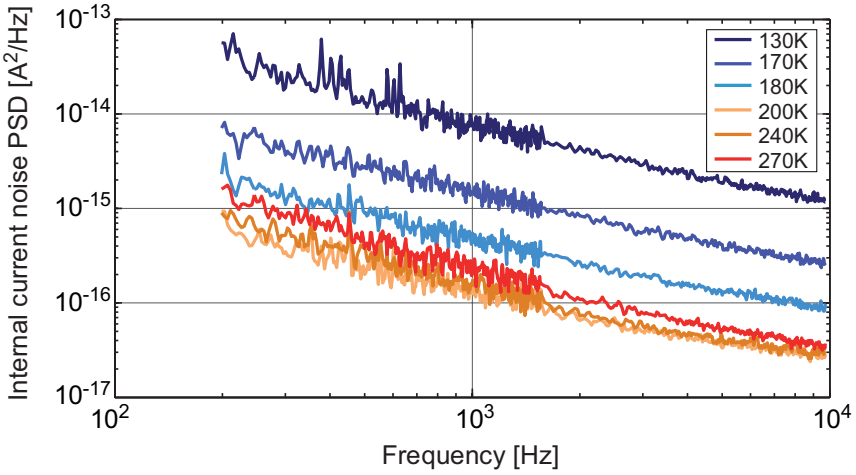

Figure 5.5: Current-noise spectra from 128 K to 283 K obtained from the voltage noise measured across the QCL and the differential resistance.

In order to evaluate the impact of the internal electrical noise to the laser frequency noise, the resulting electrical power fluctuations were calculated and transformed into equivalent frequency noise taking into account the corresponding power tuning rate measured at each temperature. The 3 kHz component of the frequency noise calculated from the measured electrical power fluctuations was extracted and is also displayed in Figure 5.3 for comparison with the optically measured frequency noise, and both curves are in very good agreement.

This important observation tends not only to explain that the higher frequency noise present at low temperature is due to an increase of internal electrical fluctuations, but gives also a more general clue that frequency

noise in QCLs is governed by internal electrical noise intrinsic to these devices. The good agreement between the optically measured and calculated frequency-noise levels suggests that frequency instabilities in free-running QCLs result from internal electrical noise, inducing temperature variations and subsequent refractive index fluctuations of the DFB grating. The temperature fluctuations ΔT scale with the electrical power ΔP dissipated in the laser through the thermal resistance R_{th}, and therefore with the measured electrical noise:

$$\Delta\nu \propto \Delta T = R_{th}\Delta P \tag{5.1}$$

The assumption that frequency noise results from internal current fluctuations intrinsic to the devices, which was made through the analysis of frequency-noise dynamics in QCLs [126], seems to be confirmed by the presented results. The transition in the slope of the frequency noise spectra from $1/f$ to $1/f^2$ also observed above a few hundred kilohertz in Sections 4.3.1 and 4.3.2 strengthens the hypothesis.

Moreover, while the slope transition was at some extent hidden by RF spikes in the spectra presented in Chapter 4, an additional measurement was carried out above 100 kHz with a buried-heterostructure de-

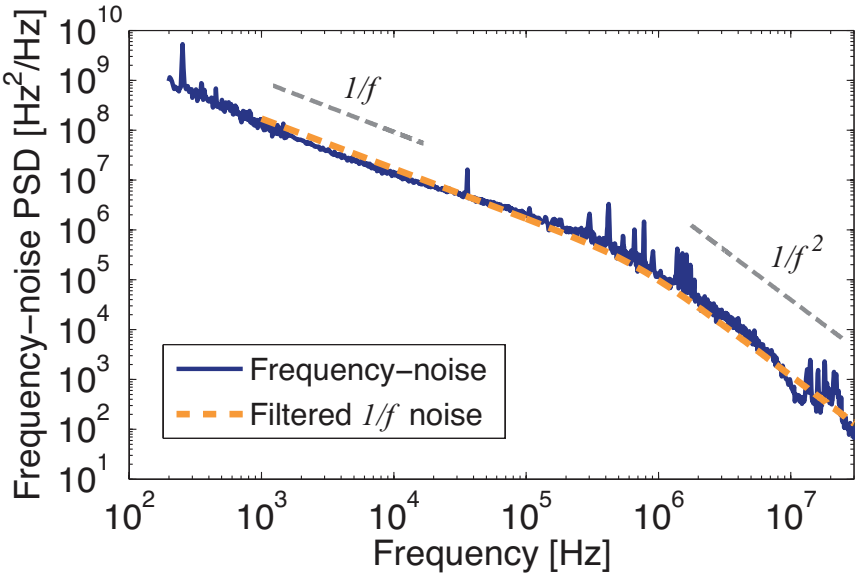

Figure 5.6: Frequency-noise PSD of a buried-heterostructure QCL (solid line). The dashed line shows pure $1/f$ low-pass filtered with a cut-off frequency $f_c = 600$ kHz.

vice (sbcw4210). Great care was taken in order to avoid high-frequency noise from the current supply. The frequency-noise PSD is shown in Figure 5.6, along with low-pass filtered pure $1/f$ noise (cut-off frequency $f_c = 600$ kHz).

A clear transition to $1/f^2$ can ben observed in that case above a few hundred kilohertz, as reported in Ref. [126]. Moreover, the cut-off frequency f_c is in good agreement with the thermal cut-off frequency of the active region, referred to as f_1, that was measured and presented in Chapter 3. The combination of this observation and the observed temperature dependence discussed above tends to show that frequency instabilities in QCLs result from the conversion of electrical power fluctuations into temperature variations, which are filtered through the thermal dynamics in the laser chip.

5.2 Effect of the thermal resistance

Two buried-heterostructure DFB QCLs of the same process but of different lengths L were measured in order to assess the impact of the laser thermal resistance, which is assumed to be the key for the conversion of electrical power fluctuations into frequency noise. For identical geometries, the thermal resistance is indeed inversely proportional to the length of the devices.

The thermal resistance R_{th} of each device was experimentally determined from the power tuning and temperature tuning coefficient $\beta_P = \Delta\nu/\Delta P$ and $\beta_T = \Delta\nu/\Delta T$, respectively (Eq. 5.2). The waveguide length of the first device, BH-QCL1 is $L = 3$ mm and a thermal resistance $R_{th} = 9$ K/W was deduced from the tuning coefficient at 300 K (same QCL used for the measurements of Section 5.1). The waveguide length of the second device, BH-QCL2, is 1.75 mm and yields a thermal resistance $R_{th} = 16$ K/W, which is almost twice the value of BH-QCL1.

$$R_{th} = \beta_P \cdot \beta_T^{-1} = \left(\frac{\Delta\nu}{\Delta P}\right) \cdot \left(\frac{\Delta\nu}{\Delta T}\right)^{-1} \tag{5.2}$$

Frequency-noise measurements were performed in the same way as in Section 5.1 and the frequency-noise PSD at 3 kHz is reported in Figure 5.7 as a function of temperature. Whereas the noise level of BH-QCL1 is $S_{3kHz} \approx 9 \cdot 10^6$ Hz^2/Hz in the upper part of the temperature measurement

range, the frequency-noise PSD at 3 kHz of BH-QCL2 is roughly four times higher and reaches $\approx 3 \cdot 10^7$ Hz^2/Hz.

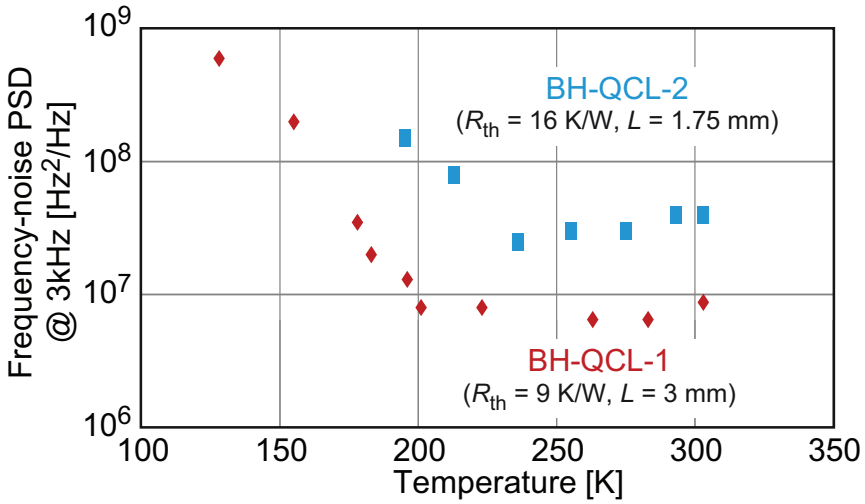

Figure 5.7: Frequency noise PSD at 3 kHz of two buried-heterostructure QCLs of different lengths L and thermal resistances R_{th} as a function of temperature.

This observation tends to confirm the assumption that the magnitude of $1/f$ frequency-noise $S_{1/f}$ scales with the inverse of the thermal resistance R_{th} (Eq. 5.3), as stated in Section 5.1.

$$S_{1/f} \propto \left(\frac{1}{R_{th}}\right)^2 \tag{5.3}$$

Moreover, the frequency-noise PSD increases in the lower part of the temperature range, as for the buried-heterostructure device of the previous section, and a slightly different transition temperature around 225 K is observed. This value is in good agreement with the electrical noise measurements of this device, which will be disclosed and discussed later in Section 5.5.

It is also important to emphasize that the magnitude of temperature and therefore frequency fluctuations depends on the level of electrical noise as well. However, the voltage noise of both devices was measured to be on the same order of magnitude, despite the different lengths L and current densities and enables a fair comparison of the effect of the thermal resistances only.

5.3 Buried-heterostructure vs. ridge QCLs

Whereas the first noise measurements over temperature were performed with a buried-heterostructure QCL, the characterization of ridge-waveguide QCLs is presented in this section in order to assess the impact of the structure, and try to understand the fundamental or structural nature of the temperature behavior observed in the last sections with two different buried-heterostructure devices.

5.3.1 Frequency-noise spectra

As for the measurements of Section 5.1, the QCLs were mounted in a cryostat in order to perform measurements from ≈ 90 K up to ≈ 300 K. Frequency-noise spectra at the two ends of the temperature range are shown in Figure 5.8. Apart from some technical noise above ≈ 30 kHz attributed to the electrical connectivity of the cryostat, the frequency-noise PSD at 250 K is in good agreement with the one of Chapter 4, obtained with the same QCL mounted on a Peltier cooler and operated at 283 K.

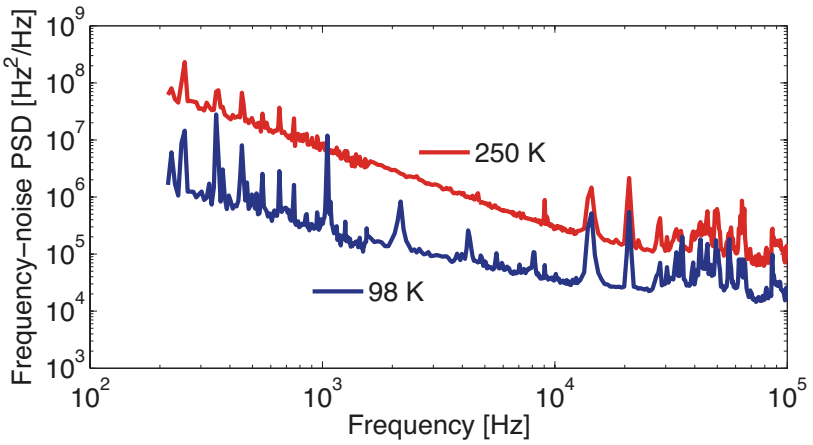

Figure 5.8: Frequency-noise PSD of a 4.6 µm ridge-waveguide QCL measured at 98 K and 250 K.

However, at lower temperatures this device shows a fundamentally different behavior than the one reported with the buried-heterostructure QCL. The frequency-noise spectrum at 98 K is indeed roughly one order of magnitude lower than the value at room-temperature, and in contrast to the buried-heterostructure devices no steep increase of noise is observed at low temperature.

The frequency-noise PSD at 3 kHz, S_{3kHz} is reported in Figure 5.9 as a function of temperature with more temperature values, along with the data of the buried-heterostructure QCL of Section 5.1. In this case, the temperature dependence is fundamentally different and no strong transition is observed around 200 K. Instead, the frequency-noise of the ridge-waveguide QCL monotonously decreases when the temperature is lowered, and finally reaches a value of $\approx 10^5$ Hz^2/Hz at 100 K. A second ridge-waveguide QCL from the same fabrication run was also measured and yielded very similar results over the same temperature range.

5.3.2 Electrical noise and comparison

As for the buried-heterostructure QCL, the equivalent frequency-noise of the ridge-waveguide device calculated from the electrical power fluctuations is shown in Figure 5.9. The voltage noise as well as the laser tuning coefficients were indeed measured at each temperature and used to calculate the expected level of frequency fluctuations.

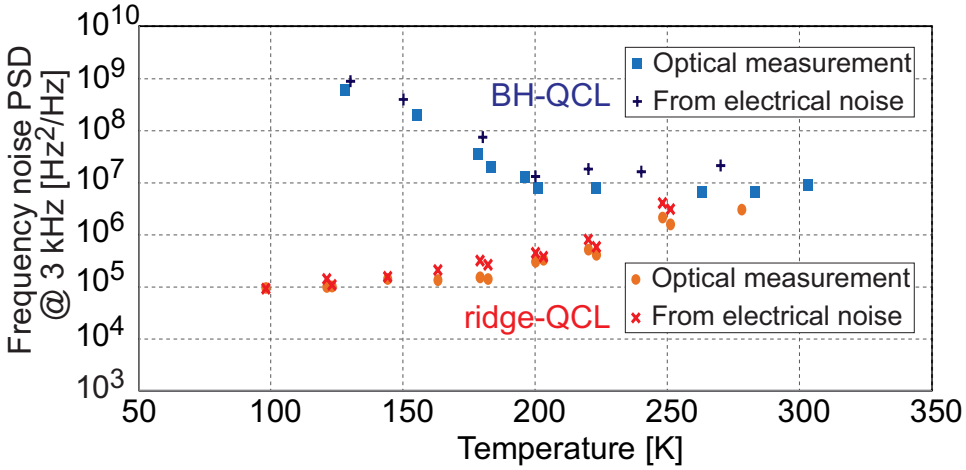

Figure 5.9: Comparison between ridge-waveguide and buried-heterostructure devices. Frequency noise optically measured using the molecular discriminator and calculated from the electrical power fluctuations are both shown.

In contrast to the buried-heterostructure device and as shown in Figure 5.10, the electrical noise across the ridge-waveguide QCL monotonously decreases with decreasing temperature. The data are shown here for the same operating conditions as for the frequency-noise measurements, and

therefore at different drive currents in each case. The dependence of electronic noise upon drive current and temperature will be discussed in details in Section 5.5.

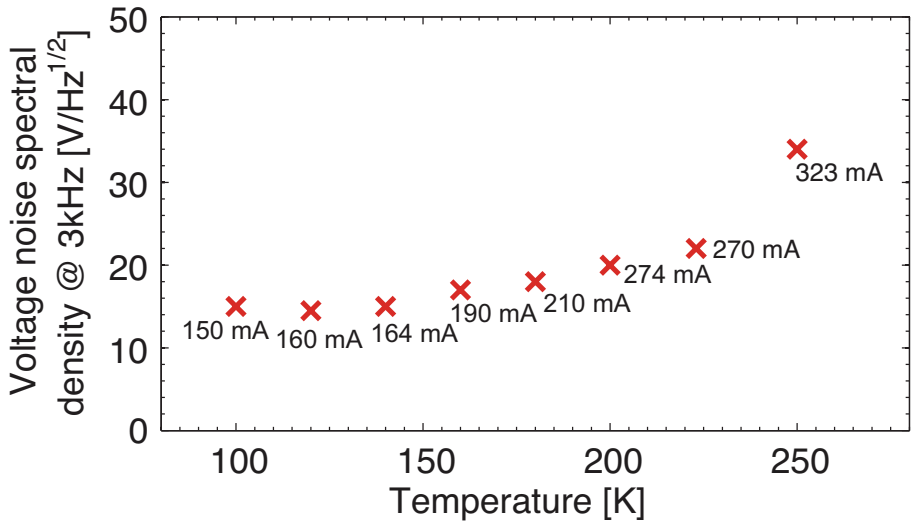

Figure 5.10: Voltage noise measured across a ridge-waveguide QCL at the same operating conditions as for frequency-noise measurements.

The voltage noise spectral density is approximately 2-3 times lower at 100 K than at room temperature, which explains part of the lower frequency noise at low temperature. A same observation applies to the power tuning coefficient, which is about two times lower at 95 K because of the lower thermal resistance (see Chapter 3). From a value of 45 MHz/mW at 250 K, the power tuning coefficient $\beta_P = \Delta\nu/\Delta P$ drops to 20 MHz/mW at 100 K. The combined effect of the lower electrical power fluctuations and lower tuning coefficient explains the difference of one order of magnitude in terms of frequency noise PSD.

Despite the different temperature dependence, another important outcome to point out is that a very good agreement is again found between the electrically and optically measured noise, as for the buried-heterostructure QCL of Section 5.1. This observation suggests that the relationship between electrical and frequency fluctuations is not limited to buried heterostructure devices, and strengthens the confidence in the ability to determine the spectral purity of a QCL from electrical noise measurements only.

5.4 Voltage and frequency noise correlation

According to the findings of the last sections, i.e. observed relation between voltage and frequency fluctuations in different kinds of QCL structures as a function of temperature, this section aims at exploring in greater detail the causality between fluctuations at the electronic level and frequency instabilities. For that purpose, the experimental setup shown in Figure 5.11 was used in order to simultaneously monitor and record both the fluctuations of the voltage $\Delta V(t)$ and optical frequency $\Delta\nu(t)$ around their static values, V_0 and ν_0 respectively.

The voltage fluctuations $\Delta V(t)$ were measured using an AC-coupled high-impedance voltage preamplifier (Signal Recovery Model 5113, 1 MHz bandwidth, 4 nV/Hz$^{1/2}$ input-referred noise). A relatively high gain of 60 dB was used in order to amplify the small voltage fluctuations into a sufficiently strong signal and avoid any contribution from the acquisition system. Regarding the optical frequency fluctuations $\Delta\nu(t)$, they were measured using the same setup described in Chapter 4, with the QCL frequency tuned to the flank of an absorption line of CO. Both signals were then filtered with identical active analog filters (same low-pass and high-pass cut-off frequencies) and sampled with a fast digital oscilloscope.

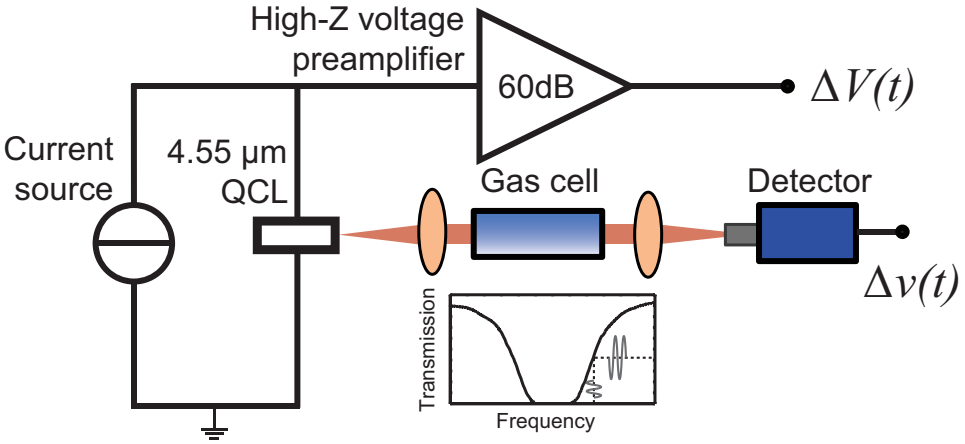

Figure 5.11: Noise correlation measurement setup. Both frequency fluctuations $\Delta\nu(t)$ and voltage fluctuations $\Delta V(t)$ are monitored at the same time.

5.4.1 Time-domain measurements

The experiment was carried out at different time scales and with two devices, namely a ridge-waveguide (sbcw2689) and a buried-heterostructure QCL (sbcw4210). Figure 5.12 (a) shows a zoom over 200 ms on the normalized time series of voltage and optical frequency fluctuations measured in a 1 kHz bandwidth. From the data set, the linear correlation coefficient ρ between frequency and voltage fluctuations was computed.

The correlation coefficient of two independent random variables X and Y is defined as the covariance of both time series σ_{xy} normalized by the product of the variance of each sample, σ_x and σ_y:

$$\rho = \frac{\sigma_{xy}}{\sigma_x \sigma_y} = \frac{\sum_{i=1}^{n} (x_i - \bar{x}) \cdot (y_i - \bar{y})}{\sqrt{\sum_{i=1}^{n} (x_i - \bar{x})^2} \cdot \sqrt{\sum_{i=1}^{n} (y_i - \bar{y})^2}} \tag{5.4}$$

The correlation coefficient ranges from -1 to 1 and gives a quantitive measurement of the linear dependence of the two random variables. Figure 5.12 (b) shows the value of the correlation coefficient as a function of the lag between the two time series calculated over the 10^5 samples of the data set. A high degree of correlation of $\rho = 0.9$ is obtained at zero lag.

Identical measurements were performed with a buried-heterostructure device, and are shown at a shorter time scale in Figure 5.13 (a) over 2.5 ms

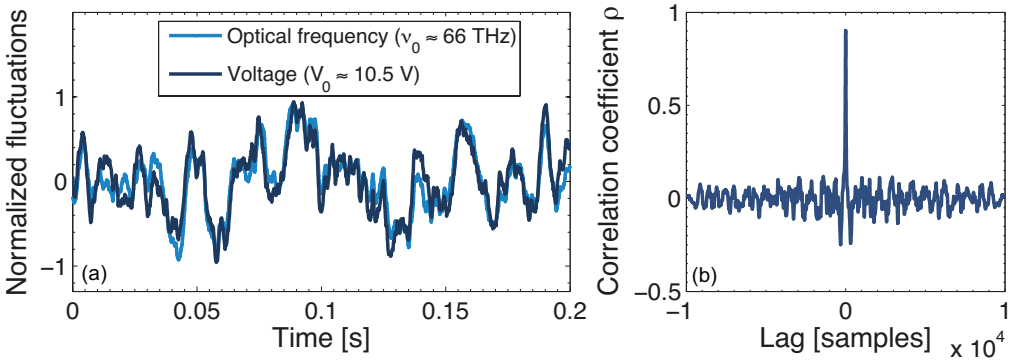

Figure 5.12: (a) Time evolution of the normalized frequency and voltage fluctuations of a ridge-waveguide QCL in a 1 kHz bandwidth. (b) Correlation coefficient between voltage and frequency as a function of the lag between the two time series.

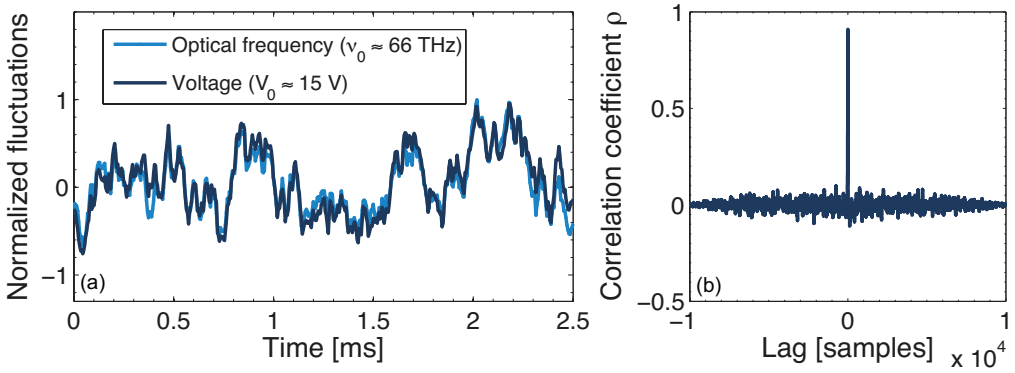

Figure 5.13: (a) Time evolution of the normalized frequency and voltage fluctuations of a buried-heterostructure QCL in a 10 kHz bandwidth. (b) Correlation coefficient between voltage and frequency as a function of the lag between the two time series.

in a 10 kHz bandwidth. A correlation coefficient of $\rho = 0.9$ was also obtained for this device (Figure 5.13 (b)).

Figures 5.14 and 5.15 show density plots of the whole data sets of normalized voltage and optical frequency as a function of each other for the ridge-waveguide and buried-heterostructure device, respectively. The correlation between the two physical quantities is clearly graphically illustrated in both cases.

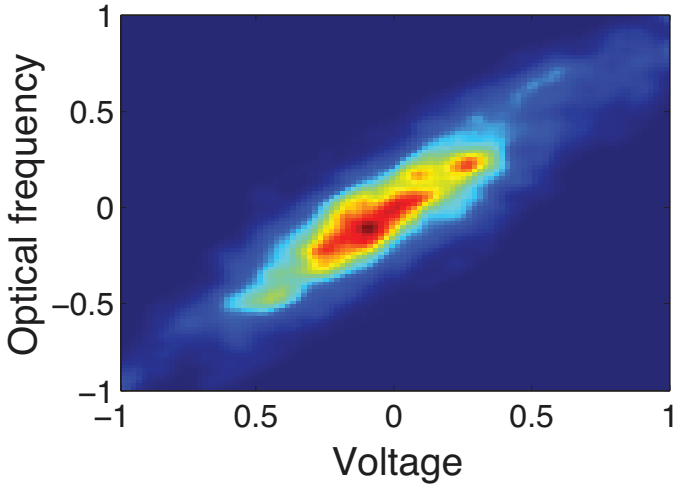

Figure 5.14: Normalized distribution of frequency fluctuations as a function of voltage fluctuations (10^4 samples over 2 s in a 1 kHz bandwidth) yielding a linear correlation coefficient $\rho = 0.9$.

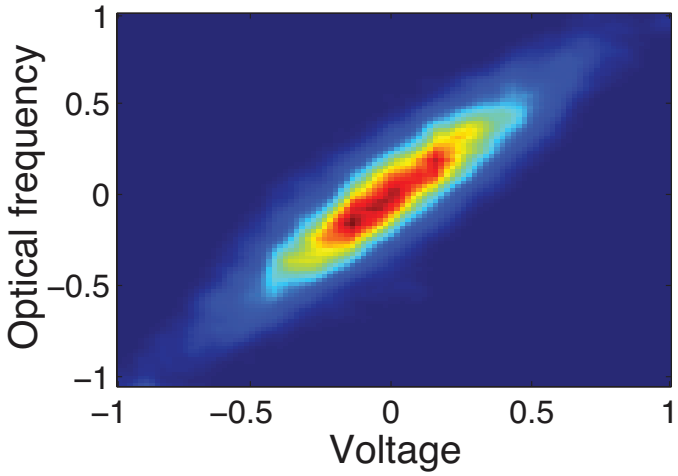

Figure 5.15: Normalized distribution of frequency fluctuations as a function of voltage fluctuations (10^4 samples over 25 ms in a 10 kHz bandwidth) yielding a linear correlation coefficient $\rho = 0.9$.

5.4.2 Frequency-domain cross spectrum

The normalized cross-spectrum, or coherency spectrum, is a correlation assessment tool in the frequency domain, which yields a quantitative value of coherence as a function of the Fourier frequency f. For two random variables X and Y, it is given by the cross power spectrum of the two variables S_{xy}, normalized by the product of each power spectrum S_x and S_y [165]:

$$\gamma(f) = \frac{S_{xy}(f)}{\sqrt{S_x(f)S_y(f)}} \tag{5.5}$$

Although the coherency spectrum can be directly measured with certain advanced dual-channel FFT analyzers, the cross-spectrum S_{xy} was measured here with a single-channel FFT analyzer using the spectrum of the sum and difference of X and Y, and can be written as $S_{xy} = (S_{x+y} - S_{x-y})/4$. The normalized cross-spectrum of optical frequency and voltage fluctuations is shown in Figure 5.16.

The data confirm the results from the previous section, and a relatively high degree of coherence on the order of ≈ 0.8 is observed. More important is that the spectrum is flat over the entire frequency range. While the time-domain measurements were performed in narrower bandwidths, this frequency domain measurement is limited by the FFT analyzer bandwidth

and shows a high degree of coherence for all Fourier frequencies up to 100 kHz.

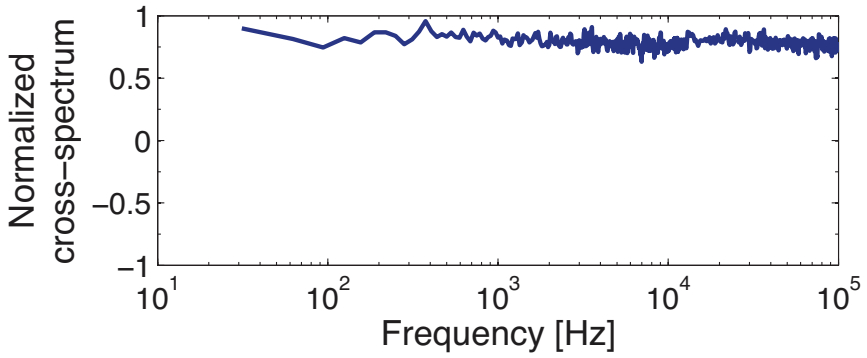

Figure 5.16: Normalized cross-power spectrum (Eq. 5.5) of voltage and optical frequency fluctuations.

5.5 Voltage noise

A clear correlation between electronic and optical frequency fluctuations has been observed and it was demonstrated that the spectral purity of QCLs can be assessed from electrical noise measurements. However, the origin and dependence of these voltage -or current- fluctuations upon device parameters and operating conditions were not discussed so far. A couple of additional experiments were carried out in view of gaining a better understanding of the noise generation phenomena and possibly identifying device parameters responsible for noise generation.

5.5.1 Buried-heterostructure device

First of all, the voltage noise properties of a second buried-heterostructure QCL (BH-QCL2, Section 5.2) were investigated in order to verify the strong increase of noise at low temperature observed with the first device in Section 5.1. Typical voltage noise spectra measured directly across the QCL are shown in Figure 5.17 at the two extreme values of the temperature range for a same drive current of 250 mA. As for the previous results, the voltage noise PSD is found to be approximately two orders of magnitude lower at room temperature.

At this point it is important to remind that these fluctuations are intrinsically generated in the semiconductor chip. The contribution of the driver current white noise i_n to the measurement is indeed given by $R_d \cdot i_n \approx 10\ \Omega \cdot 1\ \mathrm{nA/Hz^{1/2}} = 10\ \mathrm{nV/Hz^{1/2}}$ (where R_d is the QCL differential resistance) and lies at least one order of magnitude below the measured quantities in the considered frequency range, as shown by the dashed line in Figure 5.17.

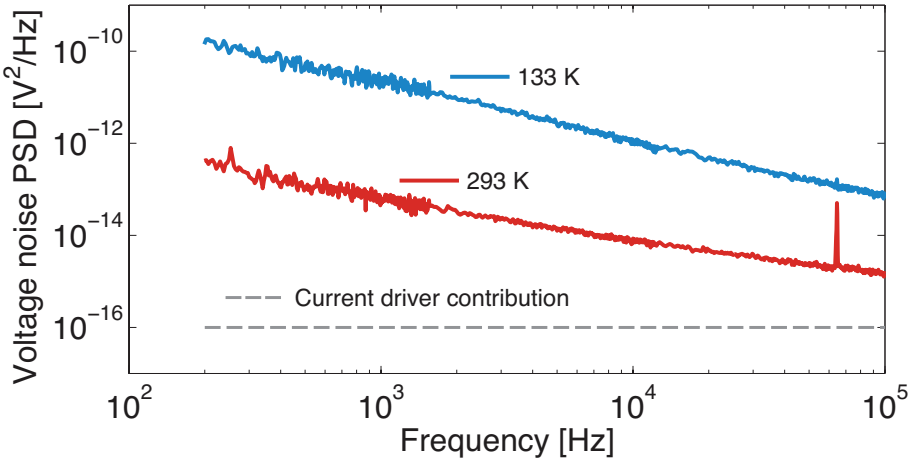

Figure 5.17: Voltage noise PSD of a buried-heterostructure QCL at 133 K and 250 K ($i_0 = 250$ mA). The noise is intrinsically generated in the QCL structure and higher than the contribution of the current driver noise floor (dashed line, considering $R_d = 10\ \Omega$ and $i_n = 1\ \mathrm{nA}/\sqrt{\mathrm{Hz}}$).

Voltage noise spectra were then systematically measured at intermediate temperatures ranging from 130 K to 293 K and various drive currents from 100 mA up to 250 mA (50 mA steps). Results are disclosed in Figure 5.18 as a function of the heat-sink temperature. As for the first results obtained with BH-QCL1, the voltage noise is relatively flat at high temperatures but strongly increases when the temperature is lowered. In this case, the transition temperature is on the order of 225 K, which is slightly higher than the one observed with the first buried-heterostructure device.

These results tend to confirm the temperature dependence observed with the first laser and rule out the possibility of an isolated device-related effect. It is also important to highlight the fact that the transition temperature is in good agreement with the one reported for the temperature dependence of the frequency-noise of this device (Figure 5.7).

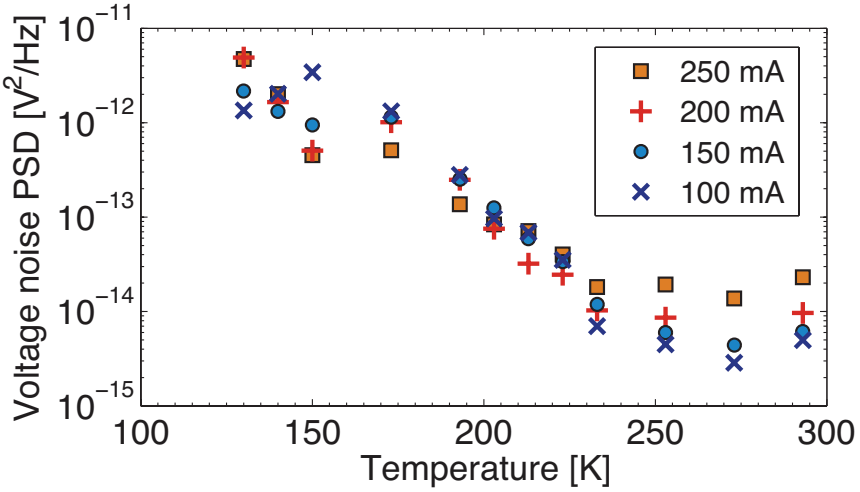

Figure 5.18: Voltage noise PSD at 3 kHz of a buried-heterostructure QCL as a function of the heat-sink temperature and at various drive currents.

5.5.2 Ridge-waveguide QCL

Figure 5.19 shows the voltage noise PSD at 3 kHz of a ridge-waveguide QCL measured from 100 K up to 280 K at various drive currents. As reported before (see Figure 5.10), no abrupt transition is observed in the low temperature range, but in this case the voltage noise monotonously decreases when the temperature is lowered. Depending on the magnitude of the drive current, up to one order of magnitude separates the value of voltage noise PSD between the extreme values of the temperature range. Moreover, the level of noise is lower than what was obtained with buried-heterostructure devices.

Up to that point, the heat-sink temperature was considered. However, as the drive current is increased, the active region temperature T_A also increases because of Joule heating and therefore differs from the heat-sink temperature. It results that the drive current and active region temperature are not independent. In order to decouple these two parameters, T_A was calculated using the electrical and thermal characteristics of the device:

$$T_A = T_0 + U_0 i_0 R_{th} \tag{5.6}$$

where T_0 is the temperature of the heat-sink, U_0 the QCL voltage, i_0 the drive current, and R_{th} the thermal resistance of the laser.

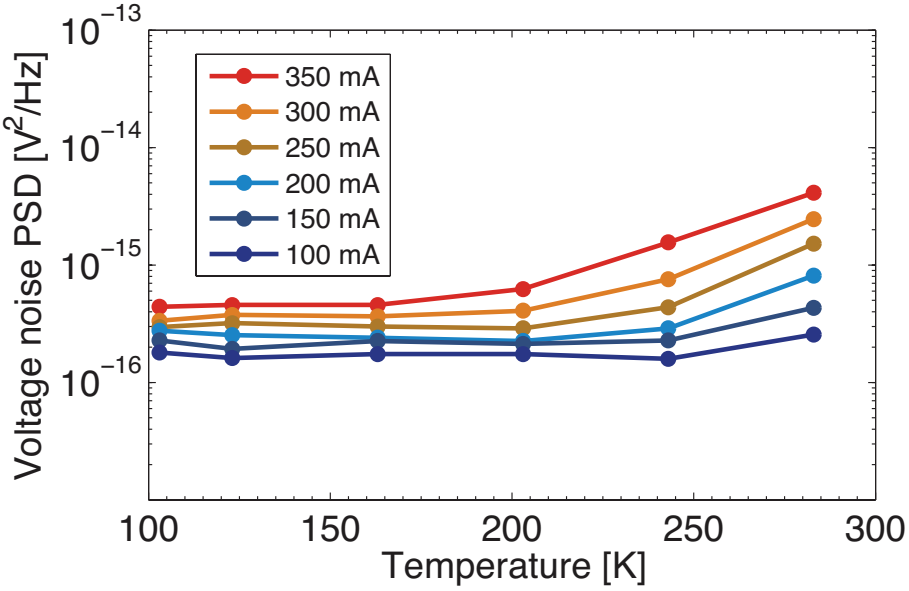

Figure 5.19: Voltage noise PSD at 3 kHz of a ridge-waveguide QCL as a function of the heat-sink temperature and at various drive currents.

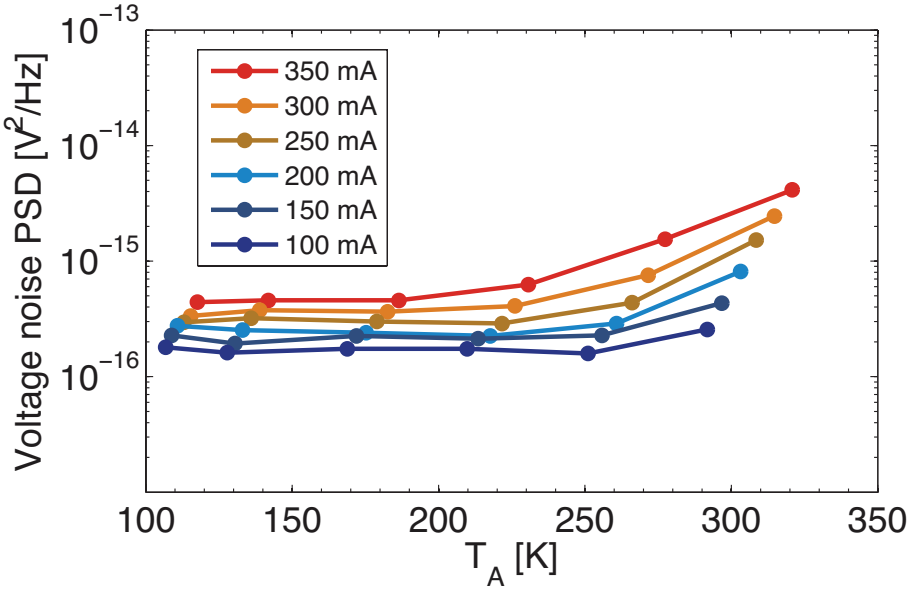

Figure 5.20: Voltage noise PSD at 3 kHz of a ridge-waveguide QCL as a function of the active region temperature T_A.

The voltage noise PSD at 3 kHz is reported in Figure 5.20 as a function of the active region temperature T_A. Despite a temperature difference of

up to 40 K between the heat-sink and the active region, and apart from spreading the data points over temperature, the obtained curves are not fundamentally different from the ones reported at constant heat-sink temperature. However, these data enable the voltage-noise PSD to be assessed as a function of the drive current at equal active region temperatures T_A. The dependence of the voltage noise PSD S_V on the drive current at constant active region temperatures of 130 K and 290 K is shown in Figure 5.21. In both cases the voltage noise PSD S_V is proportional to the square of the injection current and a very good agreement is found between the data point and a quadratic fit of the form $S_V(I) = a \cdot I^2 + b$.

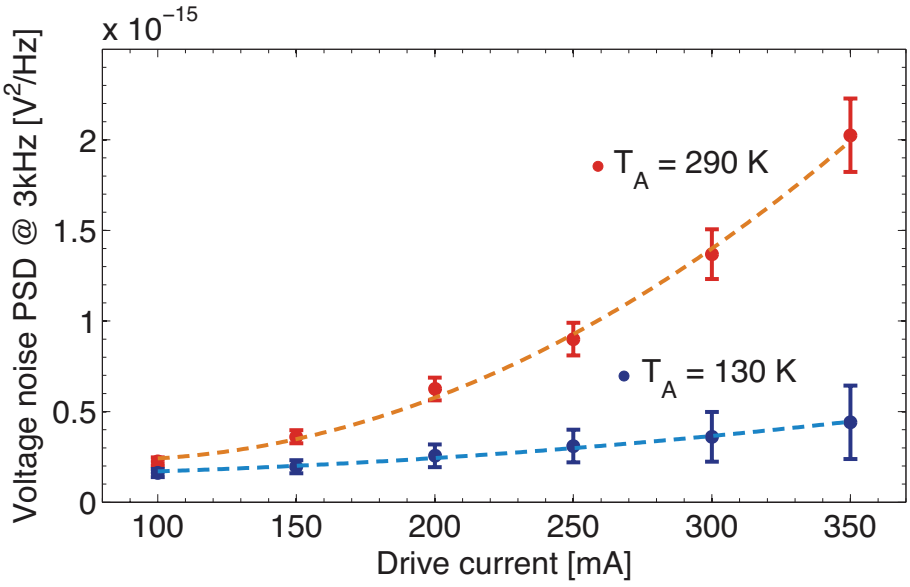

Figure 5.21: Voltage noise PSD at 3 kHz of a ridge-waveguide QCL versus drive current for fixed active region temperature T_A of 130 K and 290 K. Dashed lines: quadratic fit. Error bars: uncertainty of extrapolation.

5.5.3 Discussion and outlook

From the voltage noise measurements presented in this section, several observations can be drawn about the origin of electronic fluctuations in QCLs. First of all, it is interesting to explore and discuss in more detail the observed increase of noise at low-temperature in the buried-heterostructure QCLs. A similar temperature dependence of the magnitude of $1/f$ noise

was indeed observed in silicon Schottky diodes [166]. Low-frequency electronic noise of silicide/silicon Schottky diodes was investigated over a wide temperature range ($50-350$ K) and revealed an increase of electronic noise at low temperature. As for the buried-heterostructure QCLs, several silicide/Si diodes made out of different material systems, including $CoSi_2$/Si, Pd_2Si/Si, PtSi/Si and IrSi/Si, showed a drastic increase of electronic noise around a similar temperature transition of 200 K, and independently of the metal used for the silicide formation. A similar increase of 2-3 orders of magnitude was found between room-temperature and 100 K. In that study, the increase of noise at low temperature was observed when the thermal energy k_BT of the carriers became smaller than the standard deviation of the Schottky barrier potential distribution and was attributed to the spatial inhomogeneities of the Schottky barrier heights.

Although the material systems, device dimensions and current densities are very different than the ones of mid-IR QCLs and a direct comparison seems to some extent difficult, a similar phenomenology might be the cause of the noise increase observed at low temperature in buried-heterostructure devices. It is interesting to note that the magnitude of current noise reported for the Schottky diodes of Ref. [166] is several orders of magnitude lower than the noise measured in the buried-heterostructure QCLs, and the Schottky contacts of these devices can so far only be considered as a candidate for the origin of electronic noise. Spatial inhomogeneities of other potential barriers at the heterojunctions, interface states or traps could indeed lead to similar effects.

Flicker noise in InGaAs/AlAs/InAs resonant tunneling diodes was also studied as a function of temperature (77-293 K) in Ref. [167,168], and also represents an interesting point of comparison to our measurements. First of all, in that case no increase of noise was reported at low temperature. On the contrary, the current noise in these resonant tunneling diodes rather slightly decreases when the temperature is lowered, and the current noise PSD at 77 K was reported to be roughly one order of magnitude lower than at room-temperature. This behavior is somewhat reminiscent of the results obtained with the ridge-waveguides devices, for which no abrupt temperature transitions were observed, despite the presence of Schottky contacts. The possible contribution of the latter at low temperature in the measured buried-heterostructure QCLs might be therefore related to a specificity of the fabrication process. It is difficult to conclude whether the different temperature dependences observed between the ridge-waveguide and buried heterostructure devices are related to the process, or to physical effects due to the structural differences, such as trapping of carriers in the

insulating InP regrowth similarly to effects occurring in the oxide gate of silicon MOSFET transistors [93].

It is also instructive to compare the magnitude of current noise in the InGaAs/AlAs/InAs resonant tunneling diodes of Ref. [167] to our results. In that case, low-frequency $1/f$ noise was attributed to conductance fluctuations because of current tunneling fluctuations due to trapping of carriers at the heterointerfaces which modulate the barrier potential. For the QCLs studied in this chapter, the current noise can be inferred from the measured voltage noise PSD S_V and the differential resistance R_d and is on the order of $S_I = S_V/R_d^2 = 10^{-17}$ A^2/Hz. The levels of current noise reported for the resonant tunneling diodes of Ref. [167] are on the order of 10^{-19} A^2/Hz at 3 kHz Fourier frequency. Although two orders of magnitude separate the two values, it is interesting to note that the resonant tunneling diodes consisting of one single quantum well and a voltage bias of 0.3 V were used for the noise measurements. On the other hand, QCLs are composed of 25-30 cascaded stages of active quantum wells and injectors, which therefore significantly increases the number of layers and heterojunction interfaces. Assuming uncorrelated processes, the noise PSD of each tunneling junction would add up and in the end the magnitude of noise observed in QCLs seems similar to the one reported for the resonant tunneling diodes of Ref. [167], if scaled by the number of layers and heterojunctions. Moreover, the argument of tunneling current fluctuations due to barrier potential fluctuations is strengthened by the observation of discrete switching events in GaAs/AlGaAs resonant tunneling diodes, attributed to traps located in the barrier [169].

Finally, one must point out the dependence in I^2 of the noise PSD in Figure 5.21 at fixed active region temperature. First of all, it is interesting to mention that the voltage noise does not seem to show a different behavior below and above current threshold and suggests that it is governed by electronic transport and not affected by laser operation. Secondly, a I^2 dependence has been observed in the past, with the resonant tunneling diodes of Ref. [167], with Schottky contacts, but also in homogenous semiconductors. It is indeed a characteristic of the Hooge model (see Chapter 2), which describes $1/f$ noise in semiconductor as a bulk effect due to carriers mobility fluctuations [88, 91]. Although the total noise can be governed by different physical mechanisms, the contribution of bulk effects in QCLs is very likely not the most important one. Flicker noise in homogenous semiconductors was indeed reported in the past for thin films with small cross-sections and high resistances [170, 171], which is quite different from the configuration in QCLs.

Systematic measurement of a large number of devices with different characteristics would probably be required in order to establish a clear link between QCLs designs and electrical noise. The study of a similar design varying the number of periods and layers would for instance reveal interesting information about the contribution of tunneling current to the total noise. It was for instance shown that the number of quantum wells can impact the spectral linewidth of near-IR semiconductor laser diodes [147]. Preliminary voltage noise measurements were performed on a wider set of different QCLs emitting at 8 µm. While it is at this point too early to draw definitive conclusions, a few interesting observations can be made.

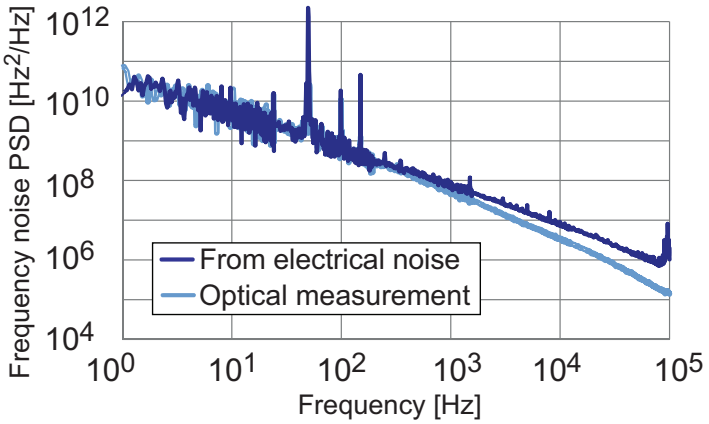

Figure 5.22: Frequency-noise PSD of an 8 µm QCL from optical and electrical measurements.

First of all, Figure 5.22 shows the frequency noise PSD spectrum of a 8 µm DFB QCL optically measured using a N_2O molecular absorption line and calculated from the voltage noise measured across the laser, as in Section 5.3.2. An excellent agreement is again found between the two measurement methods. A constant coefficient was used to transform voltage noise into equivalent frequency-noise and the slight divergence between the two curves observed above a few kilohertz is very likely due to the thermal cut-off, as in Section 5.3.2.

Figure 5.23 shows the voltage noise PSD at 3 kHz of several 8 µm DFB QCLs of various processes and of different dimensions as a function of the normalized current $(I - I_{th})/(I_{roll} - I_{th})$, where I_{th} is the threshold current and I_{roll} the roll-over current. The different laser parameters considered here are mainly the lengths and widths of the waveguides, and are indicated in Table 5.1. QCL-1035, QCL-1037 and QCL-1045 are ridge-waveguide devices and all the others are based on buried structures.

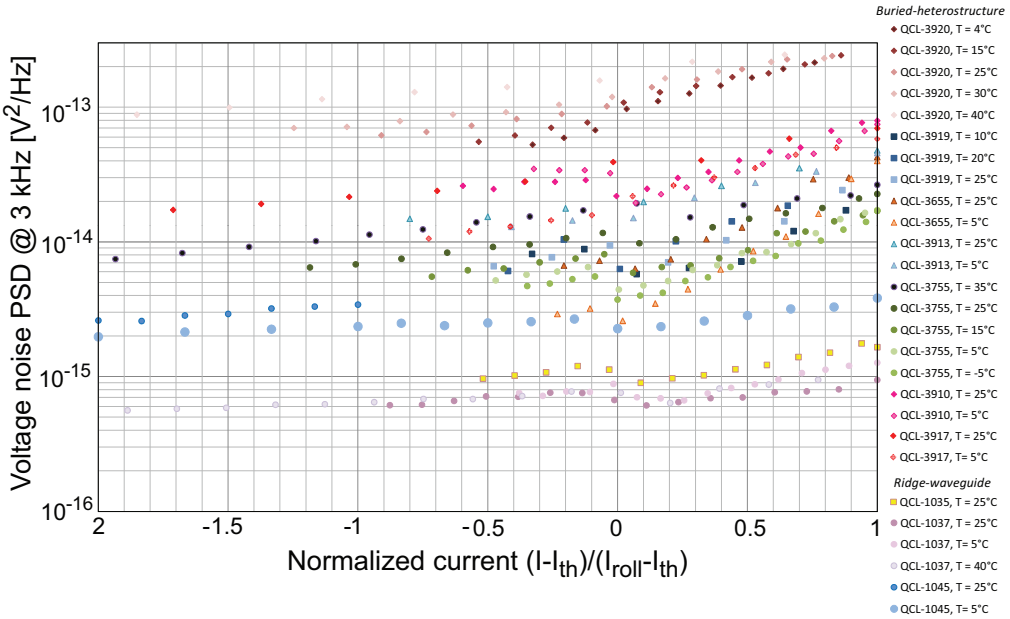

Figure 5.23: Voltage noise PSD at 3 kHz of a wide set of 8 µm DFB QCLs of different processing and waveguide dimensions.

QCL	Processing	Length [mm]	Width [µm]
3920	BH	1.5	6.5
3910	BH	1.5	9.5
3917	BH	1.5	9.5
3919	BH	1.5	12.5
3755	BH	1.5	12.5
3655	BH	2.25	12.5
3913	BH	3	7.5
1035	Ridge	1.5	14
1037	Ridge	1.5	14
1045	Ridge	1.5	9

Table 5.1: Main parameters of the 8 µm buried-heterostructure (BH) and ridge-waveguide (RW) QCLs.

First of all, it is interesting to notice that almost three orders of magnitude separate the best lasers from the worst ones. Moreover as already seen with the 4.6 µm QCLs, ridge-waveguides devices (lower curves of Figure 5.23) systematically tend to show a lower voltage noise than their buried-heterostructure counterparts.

Finally, the voltage noise (average value of the different temperatures) at a normalized current $(I - I_{th})/(I_{roll} - I_{th}) = 0.5$ is shown in Figure 5.24 as a function of the widths, lengths, and surfaces of the devices. While the length shows a large dispersion of the data, these preliminary results tend to suggest a possible impact of the width of the waveguide on the noise properties.

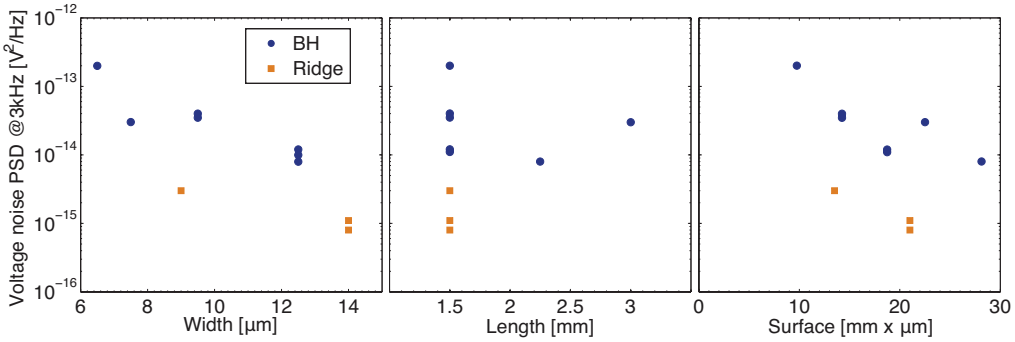

Figure 5.24: Voltage noise PSD at 3 kHz (average value of the different temperatures) as a function of the widths, lengths and surfaces of the 8 µm QCLs for a normalized current $(I - I_{th})/(I_{roll} - I_{th}) = 0.5$.

Chapter 6

Towards all-electrical linewidth narrowing

This chapter treats a novel approach aiming at reducing the frequency-noise and narrowing the linewidth of QCLs. Based on the conclusions of Chapter 5, i.e. that frequency-noise in DFB QCLs arises from electrical power fluctuations due to the electronic transport in the devices, the possibility of reducing the frequency-noise using the voltage noise across the device only has been assessed.

In contrast to conventional active frequency-stabilization methods that generally make use of optical frequency references, the voltage fluctuations across the QCL are sensed in the scheme presented here, in order to generate a correction signal that is fed back to the device, without measuring the actual fluctuations of the optical frequency. A reduction of 90% of the frequency-noise PSD is demonstrated. The main motivation behind this study resides in the integration potential of the method, which could lead to an extremely compact and all-electrical stabilization scheme.

6.1 Frequency-stabilization of QCLs

To date, linewidth narrowing of QCLs and mid-IR lasers has been carried out in various experiments and using different stabilization methods. These methods can be sorted out in different categories:

1. A first approach consists in using a frequency-sensitive element such as a high-finesse optical cavity [172], a Doppler-limited [173] molecular resonance or a Doppler-free molecular resonance [102] in order to sense the fluctuations of the QCL frequency and generate an error-signal that is usually fed back to the QCL injection current.

2. A second method consists in phase-locking the QCL radiation to a stable frequency reference. Phase-locking of QCLs to a 2 µm Thulium fiber comb [43], to a visible Ti:sapphire comb through difference frequency generation (DFG) in a nonlinear crystal [174] and to a 9 µm CO_2 laser [175] has been accomplished.

3. Finally, optical injection locking of a Fabry-Perot QCL using a tooth of a stabilized mid-IR optical frequency-comb generated through difference frequency generation (DFG) was also demonstrated [176].

Frequency-noise as well as emission linewidths can be reduced by several orders of magnitude using such techniques. As shown in Table 6.1, the kHz level is often achieved.

Ref.	Method	Device	λ	Linewidth
[172]	High-finesse FP cavity	Cryo-QCL	8.5 µm	1 kHz
[177]	Doppler-limited NO	Cryo-QCL	8.5 µm	12 kHz
[102]	Sub-Doppler CO_2	RT QCL	4.33 µm	1 kHz
[174]	Phase-lock to OFC	RT QCL	4.33 µm	1 kHz
[175]	Phase-lock to CO_2 laser	Cryo-QCL	9.2 µm	1 kHz
[43]	Phase-lock to Tm OFC	RT QCL	9.1 µm	25 kHz
[176]	Injection locking to OFC	RT FP-QCL	4.33 µm	20 kHz

Table 6.1: State-of-the-art of QCL frequency-stabilization using Fabry-Perot (FP) cavities, molecular absorption lines and optical frequency combs (OFC) (observation time $\tau_0 \approx 1-10$ ms). RT: room temperature.

Linewidth narrowing of other kinds of mid-IR lasers was also investigated. Frequency-stabilization of a 3.39 μm HeNe laser to a CH_4 line [178] and phase-locking of a CO_2 laser at 10 μm to a remote near-IR ultra-stable laser through a 43 km stabilized optical fiber link have been demonstrated [179], leading to linewidths below 100 Hz in both cases.

6.2 Voltage stabilization scheme

In contrast to conventional methods described in the previous section, the stabilization scheme presented and investigated here does not rely on any direct measurement of the optical frequency, but only of the voltage fluctuations across the laser chip.

The principle of the stabilization scheme is illustrated in Figure 6.1. The voltage fluctuations across the laser chip, which is here driven with a low-noise current source, are used as an error signal in a feedback loop. They are amplified by a broadband amplifier and then by a proportional-integral (PI) controller, and the resulting signal is used to apply fast temperature corrections to the laser chip in order to stabilize the voltage. The actuator used to achieve a fast control of the laser temperature, as well as alternate solutions, will be discussed later.

A somehow similar approach aiming at using the voltage noise across a near-infrared laser-diode in order to implement an electrical feedback and reduce the laser phase noise was proposed [156], but never demonstrated to the best of our knowledge.

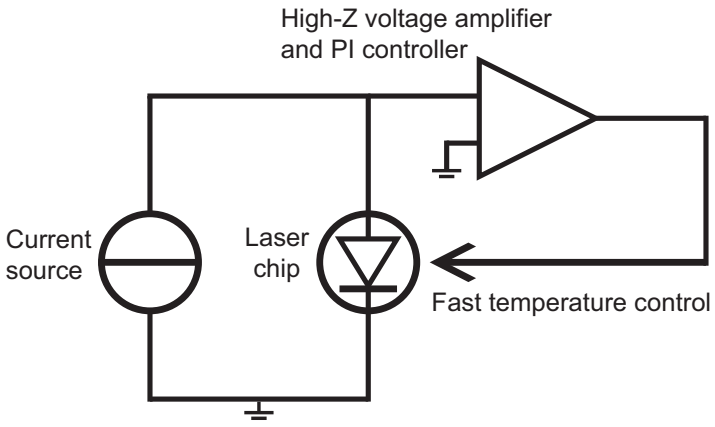

Figure 6.1: Voltage-noise stabilization principle.

6.2.1 Experimental setup

The laser used in this experiment is a 4.55 µm buried heterostructure DFB QCL provided by Alpes Lasers (sbcw4210). The stabilization scheme is shown in Figure 6.2. The QCL is mounted on a Peltier-cooler operated at 20°C and an output power of 10 mW is obtained at an injection current of 260 mA (I_{th}=220 mA).

A low-noise current source is used to drive the QCL with a current noise lower than 1 nA/$\sqrt{\text{Hz}}$ in order to avoid any linewidth broadening resulting from technical noise (see Chapter 4 and [164]). In these conditions, the contribution of the injection current noise to the frequency-noise is negligible and the fluctuations of the QCL frequency are intrinsic to the device.

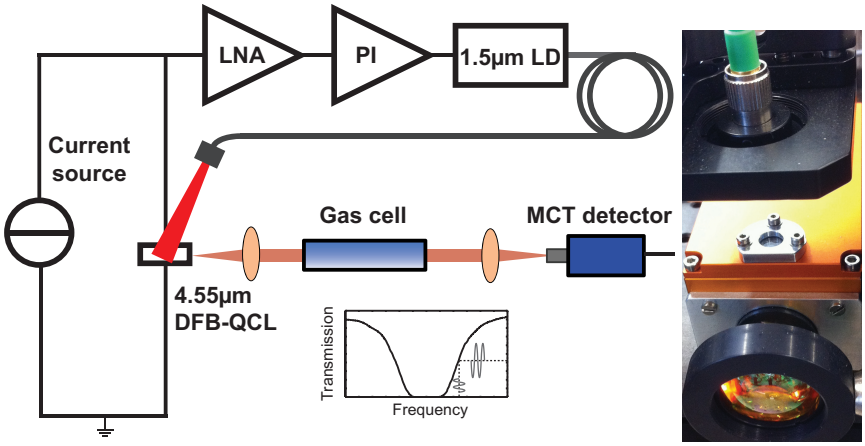

Figure 6.2: Experimental setup. The voltage noise across the QCL is amplified by a low-noise high-Z voltage-amplifier, processed through a PI controller and fed back to the QCL temperature using a fiber-coupled 1550 nm laser diode illuminating the top of the QCL chip. At the same time, the optical frequency of the QCL is analyzed using a ro-vibrational absorption line of carbon-monoxide acting as a frequency-to-intensity converter.

In the stabilization scheme presented here, the voltage noise across the QCL is sensed and used to apply fast corrections to the QCL internal temperature. The voltage fluctuations are first amplified by a high-impedance low-noise voltage preamplifier (specified bandwidth of 1 MHz and gain of 60 dB) and then by a proportional-integral (PI) controller in order to generate a correction signal.

The fast control of the QCL temperature is implemented here with a 1.55 µm diode laser (6 mW output power) illuminating the top of the QCL chip. A small fraction of the near-IR radiation on the order of 10% is indeed absorbed by the upper layers of the QCL structure, which produces a localized heating. By modulating the output power of the near-IR laser diode, the temperature of the QCL active region is therefore also modulated. As it will be shown later, a modulation bandwidth of several hundreds of kHz can be achieved using this technique.

The correction signal generated from the voltage fluctuations is sent to the modulation input of the 1550 nm laser driver in order to act on the temperature of the QCL and stabilize its voltage. As shown in Figure 6.3, at fixed current the voltage across the QCL depends on temperature ($\approx$ 10 mV/K for the present QCL) and the loop therefore stabilizes the voltage by acting on the QCL temperature and on the associated electrical conductivity. It is important to note that the stabilization of the QCL voltage is independent of the injection current, which is kept constant.

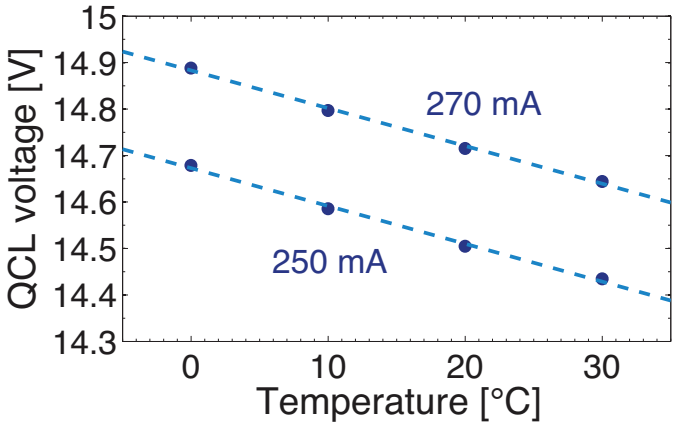

Figure 6.3: QCL voltage as a function of temperature for injection currents of 250 mA and 270 mA. A linear fit (dashed line) yields a coefficient of ≈10 mV/K.

Fast all-optical wavelength-modulation of a cryogenic Fabry-Perot QCL was also demonstrated using front-facet illumination with a femtosecond Ti:sapphire laser [180,181]. In this case, a different mechanism was responsible for the QCL frequency shift, which was not thermal but attributed to the generation of free carriers.

At the same time, the optical frequency of the QCL is monitored and analyzed using a 10 cm gas cell filled with pure carbon-monoxide (CO) at

a pressure of 2 mbar. As shown in Figure 6.2 and in a similar manner as in Chapter 4 and in Refs. [52, 124, 125], the QCL frequency is tuned to the flank of the absorption line, which acts as a frequency-to-intensity converter. At this point, the fluctuations of the laser frequency are converted into intensity fluctuations that are detected with a fast thermoelectrically-cooled photodiode (100 MHz bandwidth).

6.3 Experimental results

Figure 6.4 shows simultaneous recordings of both the QCL voltage and relative optical frequency versus time (in a 10 kHz bandwidth), first in free-running and then locked conditions. When the feedback loop is inactive ($t < 2$ ms), a clear correlation between the fluctuations of the QCL voltage and optical frequency can be observed. It is important to remind that the contributions of the current-driver noise are negligible and the fluctuations reported in Figure 6.4 are generated in the QCL structure itself.

Once activated ($t > 2$ ms), the feedback loop efficiently reduces the voltage noise (error signal) by acting on the temperature of the QCL. At the same time, a significant reduction of the fluctuations of the optical frequency is also observed.

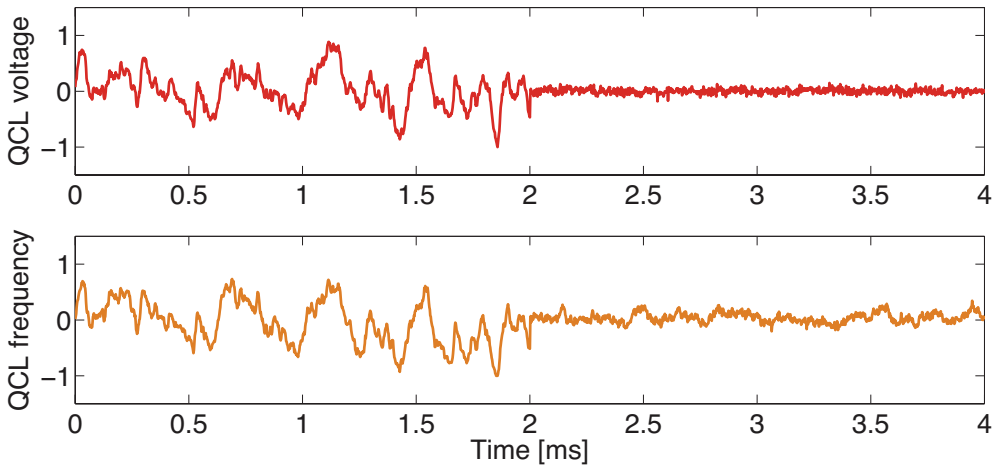

Figure 6.4: Simultaneous recordings of the QCL voltage and frequency, in unlocked ($t < 2$ ms) and locked ($t > 2$ ms) conditions within a 10-kHz bandwidth.

6.3.1 Voltage noise

Figure 6.5 shows the voltage noise across the QCL, measured after the pre-amplifier and divided by its gain ($G = 60$ dB). The voltage noise is efficiently reduced by up to 30 dB from low Fourier frequencies up to 10 kHz. From a value of $2.25 \cdot 10^{-14}$ V^2/Hz (150 nV/$\sqrt{\text{Hz}}$) at a Fourier frequency of 3 kHz, the voltage noise is reduced down to $2.5 \cdot 10^{-17}$ V^2/Hz (5 nV/$\sqrt{\text{Hz}}$), and stays above the input voltage-noise of the preamplifier of 4 nV/$\sqrt{\text{Hz}}$ ($1.6 \cdot 10^{-17}$ V^2/Hz).

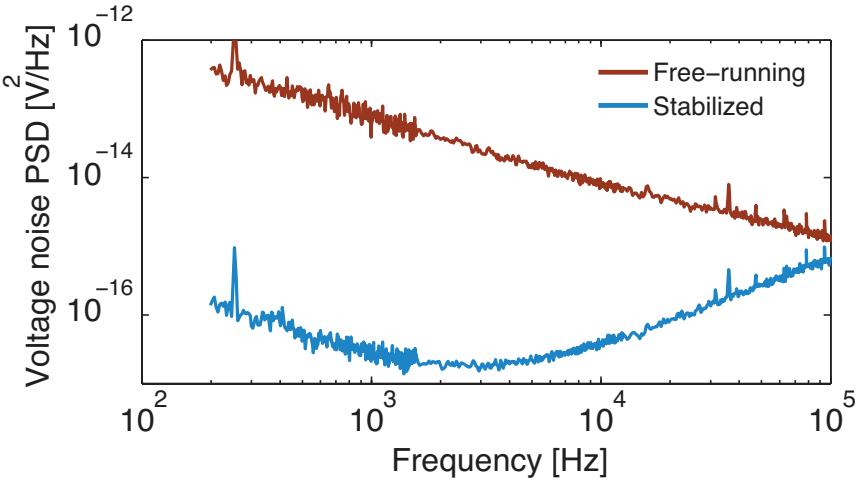

Figure 6.5: Comparison of the voltage noise PSD when the locking scheme is enabled and disabled.

6.3.2 Frequency noise and linewidth

In terms of frequency-noise PSD, a 10 dB reduction is achieved within the bandwidth of the control loop, which is about 300 kHz in the present case from the observed servo bump (Figure 6.6). From 10^7 Hz^2/Hz at a Fourier frequency of 10 kHz, the level of frequency-noise decreases to 10^6 Hz^2/Hz. From the frequency-noise PSD, the full width at half maximum (FWHM) linewidth is estimated to be narrowed from 2 MHz down to 700 kHz over a 10 ms timescale using the formalism presented in Section 2.2.3 [66].

Whereas the improvement might appear modest at first glance compared to the linewidth narrowing achievable with high-finesse cavities or molecular resonances presented in the first section of this chapter, one must

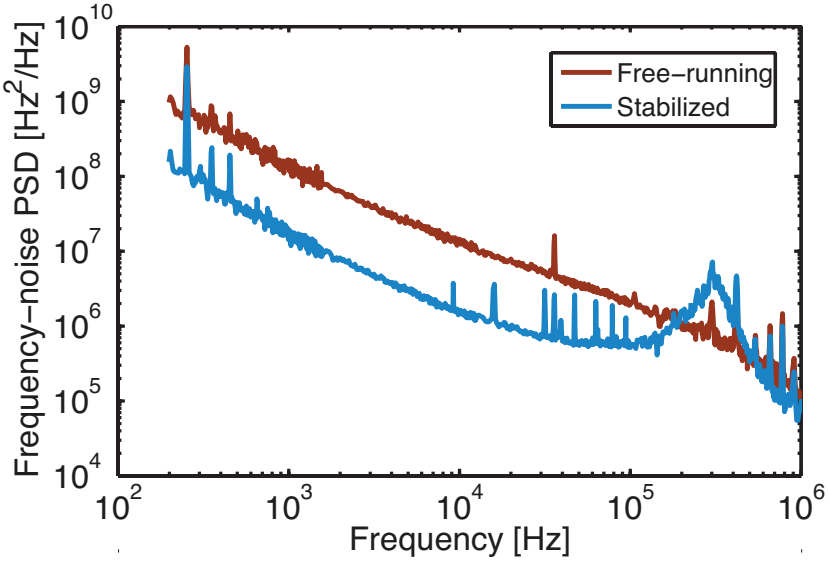

Figure 6.6: Frequency noise PSD of the free-running and stabilized QCL. The bump observed at 300 kHz corresponds to the servo-bump of the feedback loop.

highlight that in this case the frequency noise reduction is achieved without any frequency reference and optical detection and has the potential to be completely electrically integrated and very compact. The possibility of integration of the scheme will be discussed later in more details.

6.3.3 Effect of external laser and intensity noise

It was verified that the near-IR laser light that illuminates the QCL does not degrade its free-running spectral properties. As shown in Figure 6.7 no change of the frequency noise PSD was observed when the near-IR beam illuminates the QCL (lock off) compared to the noise observed in absence of near-IR illumination.

Moreover, the intensity noise of the QCL was measured in each configuration (unlocked, locked and without NIR illumination) by detuning the laser from the absorption line and is reported in Figure 6.7. In each case the contribution of intensity noise lays several orders of magnitude below the frequency-noise and does not affect any of the measurements. The noise of the detector itself (QCL beam blocked) is also shown and does not limit the measurement in the considered frequency range.

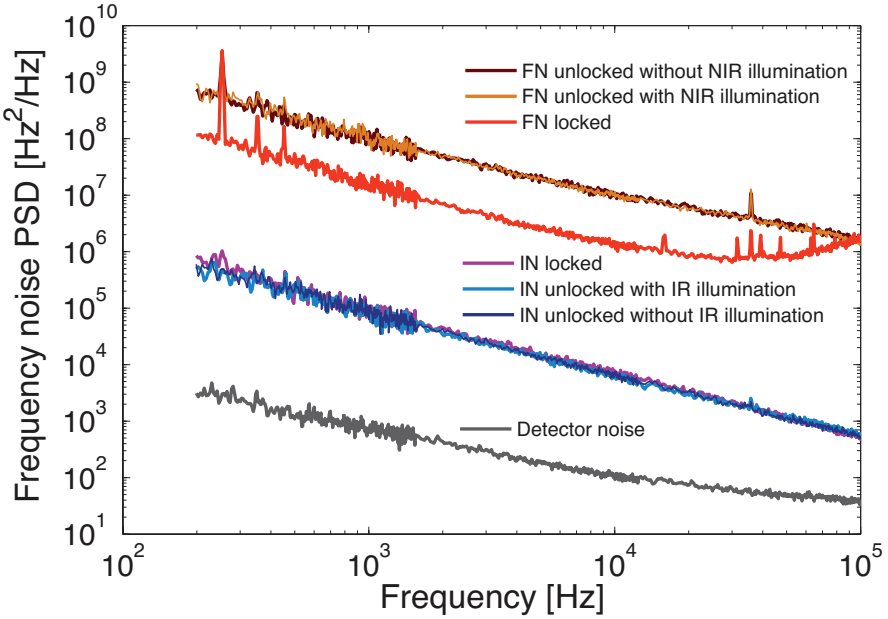

Figure 6.7: Upper traces: locked and free-running frequency noise (FN) PSD with and without NIR illumination. Middle traces: intensity noise (IN) (expressed in equivalent frequency-noise) in locked and unlocked regime and without NIR illumination. Lower trace: contribution of the detector noise.

6.3.4 Modulation and loop bandwidths

The servo-bump in the frequency-noise PSD (Figure 6.6) indicates that a loop bandwidth on the order of 300 kHz is achieved, which is on the same order of magnitude as obtained in Ref. [102] for the stabilization of a QCL to a sub-Doppler molecular transition.

The dynamic responses in magnitude and phase of the QCL voltage and optical frequency to a modulation of the intensity of the near-IR radiation are plotted in Figure 6.8. The effect of the near-IR laser driver and voltage-preamplifier was taken into account so that the dynamic responses reflect the thermal response of the QCL itself. The measurement reveals modulation bandwidths of a few hundreds of kHz.

The frequency responses are governed by the thermal dynamics in the QCL structure. A slight roll-off is indeed observed in the magnitude diagram above 100 Hz. This behavior is similar to the one reported and modeled for ridge-waveguide continuous-wave DFB QCLs under direct current

modulation and attributed to the thermal dynamics in the QCL structure (see Chapter 3).

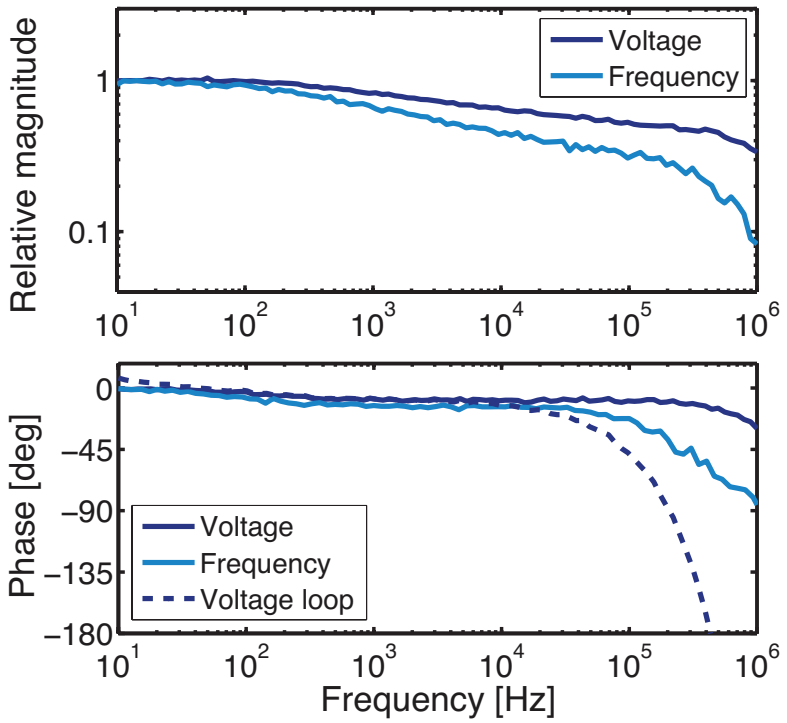

Figure 6.8: Dynamic response of the QCL voltage and optical frequency when the intensity of the near-IR radiation illuminating the QCL is modulated. Dashed line: combined phase response of the QCL, voltage preamplifier and near-IR laser driver.

The phase response of the QCL voltage combined with the other elements of the loop (voltage preamplifier and near-IR laser driver) is also shown (dashed line) in Figure 6.8. Above 100 kHz, an important additional phase-shift is introduced by both the current driver of the near-IR laser and the voltage-preamplifier, despite specified bandwidths of 1 MHz and flat magnitude responses. The phase-shift becomes close to -180° at 300 kHz (dashed line in the phase response of Fig 6.8, which is consistent with the obtained feedback-loop bandwidth. The bandwidth limitation is therefore not exclusively due to the QCL thermal response and a faster feedback loop (close to 1 MHz) could probably be obtained by using a voltage-preamplifier and a current driver for the NIR laser introducing a lower phase-shift above 100 kHz.

6.4 Limitations

As shown in Section 6.3.1, the voltage noise and therefore also the fluctuations of the electrical power dissipated in the QCL are efficiently reduced by the feedback-loop in the considered frequency range as shown in Figure 6.5. However, residual $1/f$ frequency-noise is still clearly observed both in the time domain (Figure 6.4) and in the PSD (Figure 6.6). This residual noise can be attributed neither to the intensity noise of the QCL which is orders of magnitude lower, nor to the noise of the current driver which would set a white frequency-noise floor of about 10^6 $\mathrm{Hz}^2/\mathrm{Hz}$.

Moreover, it was checked that no cross-talk builds up in the injection current within the bandwidth of the feedback loop. First of all, Figure 6.9 shows the voltage drops U_{QCL} across the QCL and U_R measured across a 20 Ω serial resistor for a 15 kHz modulation of the near-IR external illumination. The serial resistor yields an image of the current delivered by the driver $i_0 = U_R/20\ \Omega$, and it is clear from the measurement that the external near-IR illumination modulates the load (here the QCL) but does not affect the drive current.

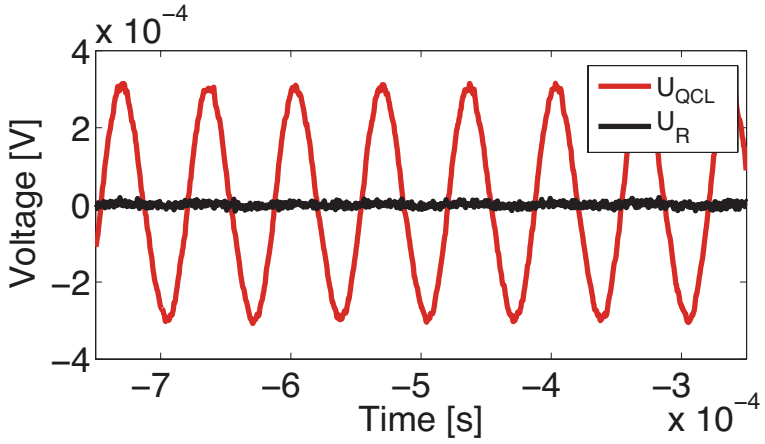

Figure 6.9: Measured voltage across the QCL and a 20 Ω serial resistor for a 15 kHz modulation of the near-IR external illumination.

Figure 6.10 shows the current noise spectral density measured through the 20 Ω serial resistor when the feedback loop was enabled and disabled. The measured spectra are identical (as shown by their ratio in the inset of Figure 6.10) and correspond to the 1 $\mathrm{nA}/\sqrt{\mathrm{Hz}}$ noise floor of the current driver (QCL500, see Section 4.1.4). This measurement confirms that the injection current is as expected independent of the locking scheme and that,

in other words, the current driver delivers a stable current independently of the variations of the electrical load in the considered frequency-range.

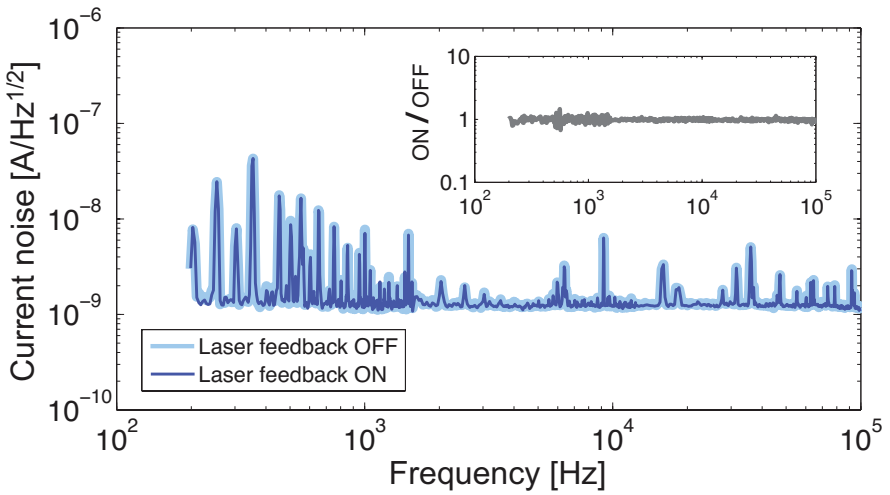

Figure 6.10: Current-noise PSD measured across a serial resistor in locked and free-running conditions. In both cases the current-noise corresponds to the noise floor of the current driver (1 nA/$\sqrt{Hz}$). Inset: ratio of the current-noise PSD when the loop is enabled and disabled.

The residual frequency noise probably reveals the contribution of other noise sources and the occurrence of residual temperature fluctuations, although the average electrical power dissipated in the device is stabilized. These residual temperature instabilities could arise from fluctuations of the intra-cavity optical power dissipated by the waveguide losses. Another possible explanation might be related to the fact that the sensed voltage is an average image of the electronic transport all along the QCL active region, whereas the temperature corrections are applied on top of the structure and can lead to an inhomogeneous temperature distribution in the active region. Frequency noise can be produced locally in the active region through local temperature fluctuations, whereas the voltage is a global measurement of the noise throughout the QCL active region and can very likely not completely describe the noise generation processes. This observation agrees with the correlation coefficient of 0.9 which was experimentally measured in free-running regime between voltage and frequency fluctuations (see Chapter 5) and tends to confirm that the two quantities are not entirely correlated.

6.5 Outlook

In this chapter, frequency-noise reduction of a mid-IR DFB QCL without using any optical frequency reference was studied and demonstrated. In the presented scheme, the voltage noise across the QCL is sensed and fed back to the active region temperature via a NIR laser diode illuminating the top of the QCL, which compensates the fluctuations of the electrical power dissipated in the structure. The optical frequency of the QCL was analyzed at the same time using a molecular absorption line and a reduction of one order of magnitude of the frequency-noise PSD was achieved within the loop bandwidth.

Although an external near-IR laser beam was used for this proof-of-concept experiment, the fast control of the QCL temperature could be potentially implemented with an integrated element placed close to the active region, such as a micro-heater. The main requirement on this element would be a sufficient temperature modulation bandwidth (on the order of a few hundred kHz) in order to counteract the fast frequency fluctuations of the QCL. Frequency tuning of a DBR laser diode at 1550 nm by resistive heating was for instance demonstrated in Ref. [182] with an integrated p-doped InP resistor. A response time on the order of 500 µs was reported, which would be probably too slow for efficient noise reduction of a QCL. Nevertheless, the results of Chapter 3 yielded modulation bandwidths on the order of a few hundred kilohertz for direct current modulation, and therefore suggest that a micro-heater with similar dimensions as the typical active region of a QCL (cross-section of $\approx$ 5 x 10 μm^2) would very likely meet the requirements.

Moreover, frequency tuning of multi-section near-IR DFB laser diodes has been demonstrated using multiple independent electrodes on a same laser chip [118,119]. A similar approach could be implemented in QCLs in order to sense the voltage fluctuations and independently apply the corrections on different electrodes of a same device. It is worthwhile to note that a three-terminal QCL with electrical modulation of the complex refractive index has already been demonstrated [183] and a similar approach could potentially be used for applying the corrections. These different possible technical implementations of the temperature feedback have the potential to lead to all-electrical active linewidth narrowing of QCLs.

Stabilization of the voltage fluctuations independently of the drive current was considered so far in the work presented in this chapter. However, our observations suggest that frequency instabilities result from electrical

power fluctuations in the semiconductor chip, and stabilizing directly this latter quantity might lead to frequency-noise reduction as well. In other words, instead of stabilizing the voltage at fixed current, it might be interesting to drive the laser at constant electrical power P_{QCL}. For that purpose, both the instantaneous current and voltage would have to be measured and multiplied to assess the electrical power (see Eq. 6.1).

Constant power circuits are commonly used in battery chargers and LCD displays in order to compensate slow variations of the electrical resistivity and commercial integrated circuits for that purpose are available (e.g. MAX4210 from Maxim Integrated). However, the power fluctuations in the case of QCLs are fast and several orders of magnitude separate the weak but fast fluctuations from the large DC values. Sophisticated electronics would be required in order to extract a usable error signal. Nevertheless, a possible approach aiming at generating an error signal directly proportional to the fluctuations of the electrical power is presented here, and based on the scheme shown in Figure 6.11.

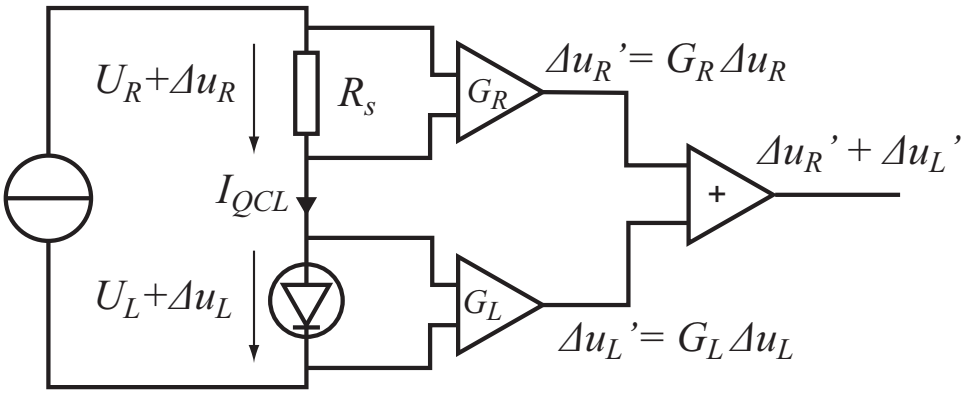

Figure 6.11: Electrical power stabilization scheme using a serial resistor R_s in order to drive the laser at constant electrical power.

The instantaneous electrical power dissipated in the QCL chip P_{QCL} is given by the product of the instantaneous voltage and current:

$$\begin{aligned} P_{QCL} = U_{QCL} \cdot I_{QCL} &= \Big(U_L + \Delta u_L\Big) \cdot \Big(\frac{U_R + \Delta u_R}{R_s}\Big) \\ &= \frac{1}{R_s}\Big(U_L U_R + U_L \Delta u_R + U_R \Delta u_L + \Delta u_L \Delta u_R\Big) \end{aligned} \tag{6.1}$$

where the current I_{QCL} flowing in the QCL is measured with a serial resis-

tor R_s. Neglecting the 2^{nd} order term $\Delta u_L \Delta u_R$, the instantaneous variations of the electrical power can be written as:

$$\Delta P_{QCL} = \frac{1}{R_s}\Big(U_L \Delta u_R + U_R \Delta u_L\Big) \tag{6.2}$$

If the serial resistor is chosen so that its voltage drop equals the one across the QCL, i.e. $U_R = U_L = U$, the variation of the electrical power is then simply proportional to the sum of the voltage fluctuations measured across the laser and the serial resistor:

$$\Delta P_{QCL} = \frac{U}{R_s}\Big(\Delta u_R + \Delta u_L\Big) \tag{6.3}$$

In this configuration ($G_R = G_L = 1$), the total AC voltage drop $\Delta u_R + \Delta u_L$ is proportional to the electrical power fluctuations and could therefore be used in a very simple way as an error signal in order to correct fast electrical power variations in the QCL through the injection current, without any external actuator.

However, the condition $U_L = U_R$ can be challenging to achieve. A possible way of overcoming this limitation would consist in amplifying the voltage fluctuations across the laser and the sense resistor with well-chosen gains. In case different gains G_L and G_R are used, the amplified voltage fluctuations can be written as $\Delta u'_L = G_L \cdot \Delta u_L$ and $\Delta u'_R = G_R \cdot \Delta u_R$. The electrical power fluctuations in the QCL given by Eq. 6.2 become:

$$\Delta P_{QCL} = \frac{1}{R_s}\Big(U_L \frac{\Delta u'_R}{G_R} + U_R \frac{\Delta u'_L}{G_L}\Big) \tag{6.4}$$

If the gains are chosen so that $\dfrac{U_L}{G_R} = \dfrac{U_R}{G_L} = C$, then a very simple expression for the electrical power is found:

$$\Delta P_{QCL} = \frac{C}{R_s}\Big(\Delta u'_R + \Delta u'_L\Big) \tag{6.5}$$

As for Eq. 6.3, the fluctuations of the electrical power are then simply given by the sum of the amplified voltages $\Delta u'_R$ and $\Delta u'_L$, and could be used to drive the QCL at constant electrical power by acting on the drive current. Either technique has the potential to drive the laser at constant power and possibly lead to frequency-noise reduction.

Finally, it is worth noticing that in spite of different underlying physical mechanisms, correlation between frequency and voltage noise was also observed in interband semiconductor lasers [153–156]. All the discussion and outcomes presented in this chapter might therefore be possibly applied to other kinds of semiconductor lasers and trigger new developments of low-noise and compact integrated light sources.

Chapter 7

Conclusion and outlook

In the course of this thesis, the spectral properties of single-mode distributed feedback (DFB) quantum cascade lasers (QCLs) emitting in the mid-IR spectral region were investigated. The experimental results presented in this thesis allowed a better understanding of the underlying mechanisms of optical frequency instabilities. As a result, novel and innovative methods aiming at quantifying and improving the spectral purity of DFB QCLs from electrical measurements were demonstrated. Among other results, a compact active stabilization scheme yielding 90% reduction of the frequency-noise power spectral density without making use of any optical frequency reference was demonstrated, which will be certainly interesting for the development of future low-noise compact semiconductor laser sources.

A first important outcome of the work lies in the characterization of frequency noise of different single-frequency QCLs in the mid-IR spectral region. Considering a low-noise injection current is used to drive the lasers, excellent spectral properties have been observed in free-running QCLs. We reported for instance one of the lowest level of frequency noise in the $4-5$ µm range and a corresponding linewitdh of $\approx$ 550 kHz at room-temperature (1 ms observation time), which represents a quality factor (Q-factor) higher than 10^8, when compared to the 66 THz optical carrier. On the other hand, a drastic linewidth broadening occurs if noisy electronics is used. We demonstrated that a current noise lower than 1 nA/Hz$^{1/2}$ is generally required to reach the intrinsic properties of QCLs. The realization of a low-noise current driver able to deliver a stable current and a sufficiently high output voltage required to bias the cascaded structure of QCLs was also studied in this thesis. A current noise value of 350 pA/Hz$^{1/2}$

was achieved and is still state-of-the-art today.

A number of experiments and results aiming at shedding light on the underlying sources of frequency instabilities in QCLs were then disclosed and discussed. A striking difference was found between buried-heterostructure and ridge-waveguide QCLs at low temperature, suggesting different noise mechanisms between the distinct processing of these devices. Despite better noise performances for the ridge-waveguide lasers, in a general manner it was shown that DFB QCLs at room-temperature benefit from excellent spectral properties, i.e. linewidths of 1 MHz and below, and can compete with state-of-the-art interband laser diodes in the near-IR. The latter observation is of prime importance since the development of real-world application relies on devices working at room temperature and requiring no cryogenic cooling.

The frequency noise increase observed at low temperature in buried heterostructure QCLs was found to follow a similar trend than the electrical noise properties. This outcome led to the more general interpretation that frequency instabilities in QCLs are generated through fast temperature changes due to fluctuations of the dissipated electrical power in the devices. Measurements of the frequency tuning dynamics indeed showed that the active region of DFB QCLs is governed by a thermal response of up to a few hundreds of kilohertz, and are therefore subject to temperature fluctuations within this bandwidth. From this discussion, an important and experimentally verified conclusion is that a low thermal resistance is required for low frequency-noise QCLs in order to minimize the impact of electrical power fluctuations on the average temperature of the active region, and therefore on the laser emission frequency.

Further measurements of the correlation between fluctuations of the optical frequency and electrical power were performed and confirmed, both in the time and frequency domains, a high level of correlation ($\rho = 0.9$) between the two quantities within the QCLs thermal bandwidth. All these observations led to a new and very simple method for assessing the spectral properties of QCL only from electrical measurements combined to specific physical parameters of the devices. This method enables a simple and fast testing of QCLs noise properties in a systematic manner.

Voltage noise in a couple of devices was investigated as a function of the operating conditions and showed different interesting outcomes. In addition to a drastic increase of noise below $\approx$ 200 K observed in two buried-heterostructure devices at 4.55 µm, the measured ridge-waveguide QCLs tend to benefit from lower electrical noise even at room-temperature,

and therefore better spectral properties. This observation might suggest an advantage of ridge-waveguide over buried-heterostructure devices in terms of electrical noise, because of the possible appearance of parasitic junctions between the active region or the cladding layers and the regrowth of intrinsic InP. Despite preliminary results obtained with a larger set of 8 µm DFB QCLs tend to confirm a higher noise in buried structures, one must remind the important impact of the crystal quality and fabrication processes on low-frequency $1/f$ noise. The investigation of leakage currents and noise properties of p-i-n InP junctions as well as in buried-heterostructure QCLs of different dimensions and different surface to volume ratios would probably bring interesting clues about the structural impact on noise generation.

In addition to investigating the spectral purity of mid-IR QCLs as well as the link between the noise of the optical frequency and fluctuations at the electrical level, a novel frequency stabilization only based on voltage noise measurements was presented. A reduction of 90% of the frequency noise was experimentally demonstrated using this method. The basic principle consists in generating a correction signal from the voltage noise across the laser and in feeding it back to the laser temperature. As the scheme does not involve any optical frequency reference, it has the potential to be highly integrated.

While external near-IR laser illumination was used in the proof-of-concept experiment, a few possible tracks to follow in order to obtain a all-electrical scheme were proposed. It includes for instance the use of a micro-heater close to the laser active region or a multiple electrode QCL design in order to independently measure the voltage fluctuations and apply corrections. In a general manner, all the results presented in this thesis open the way to new developments of compact low-noise single-frequency light sources based on integrated active stabilization techniques and optimized laser structures. This work could also possibly apply to other laser systems and trigger new advances in the field of narrow-linewidth integrated monochromatic light sources.

Bibliography

[1] J. Faist, F. Capasso, D. L. Sivco, C. Sirtori, A. L. Hutchinson, and A. Y. Cho, "Quantum cascade laser," *Science*, vol. 264, pp. 553–556, Apr. 1994. PMID: 17732739.

[2] M. Troccoli, D. Bour, S. Corzine, G. Hofler, A. Tandon, D. Mars, D. J. Smith, L. Diehl, and F. Capasso, "Low-threshold continuous-wave operation of quantum-cascade lasers grown by metalorganic vapor phase epitaxy," *Applied Physics Letters*, vol. 85, no. 24, pp. 5842–5844, 2004.

[3] J. Faist, F. Capasso, C. Sirtori, D. L. Sivco, J. N. Baillargeon, A. L. Hutchinson, S.-N. G. Chu, and A. Y. Cho, "High power midinfrared (λ-5 μm) quantum cascade lasers operating above room temperature," *Applied Physics Letters*, vol. 68, pp. 3680–3682, June 1996.

[4] J. Faist, C. Gmachl, F. Capasso, C. Sirtori, D. L. Sivco, J. N. Baillargeon, and A. Y. Cho, "Distributed feedback quantum cascade lasers," *Applied Physics Letters*, vol. 70, no. 20, pp. 2670–2672, 1997.

[5] C. Gmachl, J. Faist, J. Bailargeon, F. Capasso, C. Sirtori, D. L. Sivco, S. N. G. Chu, and A. Y. Cho, "Complex-coupled quantum cascade distributed-feedback laser," *IEEE Photonics Technology Letters*, vol. 9, no. 8, pp. 1090–1092, 1997.

[6] M. Beck, D. Hofstetter, T. Aellen, J. Faist, U. Oesterle, M. Ilegems, E. Gini, and H. Melchior, "Continuous wave operation of a mid-infrared semiconductor laser at room temperature," *Science*, vol. 295, pp. 301–305, Jan. 2002. PMID: 11786637.

[7] B. Hinkov, A. Bismuto, Y. Bonetti, M. Beck, S. Blaser, and J. Faist, "Singlemode quantum cascade lasers with power dissipation below 1 W," *Electronics Letters*, vol. 48, no. 11, pp. 646–647, 2012.

[8] A. Lyakh, R. Maulini, A. Tsekoun, R. Go, and C. K. N. Patel, "Tapered 4.7 μm quantum cascade lasers with highly strained active region composition delivering over 4.5 watts of continuous wave optical power," *Optics Express*, vol. 20, p. 4382, Feb. 2012.

[9] A. Kosterev, G. Wysocki, Y. Bakhirkin, S. So, R. Lewicki, M. Fraser, F. Tittel, and R. F. Curl, "Application of quantum cascade lasers to trace gas analysis," *Applied Physics B*, vol. 90, pp. 165–176, Feb. 2008.

[10] C. Patel, "Continuous-wave laser action on vibrational-rotational transitions of CO2," *Physical Review*, vol. 136, pp. A1187–A1193, Nov. 1964.

[11] J. F. Butler, A. R. Calawa, R. J. P. Jr, T. C. Harman, A. J. Strauss, and R. H. Rediker, "PbTe diode laser," *Applied Physics Letters*, vol. 5, no. 4, pp. 75–77, 1964.

[12] J. Meyer, C. A. Hoffman, F. J. Bartoli, and L. Ram-Mohan, "Type −II quantum−well lasers for the mid−wavelength infrared," *Applied Physics Letters*, vol. 67, no. 6, pp. 757–759, 1995.

[13] J. G. Kim, L. Shterengas, R. U. Martinelli, and G. L. Belenky, "High-power room-temperature continuous wave operation of 2.7 and 2.8 μm In (Al)GaAsSb/GaSb diode lasers," *Applied Physics Letters*, vol. 83, pp. 1926–1928, Sept. 2003.

[14] K. Mansour, Y. Qiu, C. Hill, A. Soibel, and R. Yang, "Mid-infrared interband cascade lasers at thermoelectric cooler temperatures," *Electronics Letters*, vol. 42, no. 18, pp. 1034–1035, 2006.

[15] W. Bewley, J. Nolde, D. Larrabee, C. Canedy, C. S. Kim, M. Kim, I. Vurgaftman, and J. Meyer, "Interband cascade laser operating cw to 257 K at λ=3.7 μm," *Applied Physics Letters*, vol. 89, no. 16, pp. 161106–161106–3, 2006.

[16] W. W. Bewley, C. L. Canedy, C. S. Kim, M. Kim, C. D. Merritt, J. Abell, I. Vurgaftman, and J. R. Meyer, "Continuous-wave interband cascade lasers operating above room temperature at $\lambda = 4.7$-5.6 μm," *Optics Express*, vol. 20, pp. 3235–3240, Jan. 2012.

[17] D. Richter, A. Fried, B. P. Wert, J. G. Walega, and F. K. Tittel, "Development of a tunable mid-IR difference frequency laser source

for highly sensitive airborne trace gas detection," *Applied Physics B*, vol. 75, pp. 281–288, Sept. 2002.

[18] S. Sanders, R. Lang, L. Myers, M. Fejer, and R. Byer, "Broadly tunable mid-IR radiation source based on difference frequency mixing of high power wavelength-tunable laser diodes in bulk periodically poled LiNbO3," *Electronics Letters*, vol. 32, no. 3, pp. 218–219, 1996.

[19] S. Haidar, K. Miyamoto, and H. Ito, "Generation of tunable mid-IR (5.5-9.3 μm) from a 2-μm pumped ZnGeP2 optical parametric oscillator," *Optics Communications*, vol. 241, pp. 173–178, Nov. 2004.

[20] R. S. RF Kazarinov, "Possibility of the amplification of electromagnetic waves in a semiconductor with a superlattice," *Soviet Physycs. Semiconductors*, vol. 5, no. 4, pp. 707–709, 1971.

[21] J. Faist, *Quantum Cascade Lasers*. Oxford University Press, Mar. 2013.

[22] B. S. Williams, "Terahertz quantum-cascade lasers," *Nature Photonics*, vol. 1, pp. 517–525, Sept. 2007.

[23] J. Faist, M. Beck, T. Aellen, and E. Gini, "Quantum-cascade lasers based on a bound-to-continuum transition," *Applied Physics Letters*, vol. 78, no. 2, pp. 147–149, 2001.

[24] D. Hofstetter, M. Beck, T. Aellen, and J. Faist, "High-temperature operation of distributed feedback quantum-cascade lasers at 5.3 μm," *Applied Physics Letters*, vol. 78, pp. 396–398, Jan. 2001.

[25] D. Hofstetter, J. Faist, M. Beck, A. Muller, and U. Oesterle, "Demonstration of high-performance 10.16 μm quantum cascade distributed feedback lasers fabricated without epitaxial regrowth," *Applied Physics Letters*, vol. 75, no. 5, pp. 665–667, 1999.

[26] T. Aellen, S. Blaser, M. Beck, D. Hofstetter, J. Faist, and E. Gini, "Continuous-wave distributed-feedback quantum-cascade lasers on a peltier cooler," *Applied Physics Letters*, vol. 83, no. 10, pp. 1929–1931, 2003.

[27] H. Kogelnik and C. Shank, "Coupled-wave theory of distributed feedback lasers," *Journal of Applied Physics*, vol. 43, no. 5, pp. 2327–2335, 1972.

[28] G. Luo, C. Peng, H. Le, S. S. Pei, W.-Y. Hwang, B. Ishaug, J. Um, J. N. Baillargeon, and C. H. Lin, "Grating-tuned external-cavity quantum-cascade semiconductor lasers," *Applied Physics Letters*, vol. 78, no. 19, pp. 2834–2836, 2001.

[29] R. Maulini, M. Beck, J. Faist, and E. Gini, "Broadband tuning of external cavity bound-to-continuum quantum-cascade lasers," *Applied Physics Letters*, vol. 84, pp. 1659–1661, Mar. 2004.

[30] R. Maulini, D. A. Yarekha, J.-M. Bulliard, M. Giovannini, J. Faist, and E. Gini, "Continuous-wave operation of a broadly tunable thermoelectrically cooled external cavity quantum-cascade laser," *Optics Letters*, vol. 30, pp. 2584–2586, Oct. 2005.

[31] G. Wysocki, R. F. Curl, F. K. Tittel, R. Maulini, J. M. Bulliard, and J. Faist, "Widely tunable mode-hop free external cavity quantum cascade laser for high resolution spectroscopic applications," *Applied Physics B*, vol. 81, pp. 769–777, Oct. 2005.

[32] R. Maulini, A. Mohan, M. Giovannini, J. Faist, and E. Gini, "External cavity quantum-cascade laser tunable from 8.2 to 10.4 μm using a gain element with a heterogeneous cascade," *Applied Physics Letters*, vol. 88, no. 20, pp. 201113–201113–3, 2006.

[33] A. A. Kosterev and F. Tittel, "Chemical sensors based on quantum cascade lasers," *IEEE Journal of Quantum Electronics*, vol. 38, no. 6, pp. 582–591, 2002.

[34] K. Namjou, S. Cai, E. A. Whittaker, J. Faist, C. Gmachl, F. Capasso, D. L. Sivco, and A. Y. Cho, "Sensitive absorption spectroscopy with a room-temperature distributed-feedback quantum-cascade laser," *Optics Letters*, vol. 23, pp. 219–221, Feb. 1998.

[35] A. A. Kosterev, A. L. Malinovsky, F. K. Tittel, C. Gmachl, F. Capasso, D. L. Sivco, J. N. Baillargeon, A. L. Hutchinson, and A. Y. Cho, "Cavity ringdown spectroscopic detection of nitric oxide with a continuous-wave quantum-cascade laser," *Applied Optics*, vol. 40, pp. 5522–5529, Oct. 2001.

[36] R. Lewicki, G. Wysocki, A. A. Kosterev, and F. K. Tittel, "QEPAS based detection of broadband absorbing molecules using a widely tunable, cw quantum cascade laser at 8.4 um," *Optics Express*, vol. 15, pp. 7357–7366, June 2007.

[37] D. D. Nelson, B. McManus, S. Urbanski, S. Herndon, and M. S. Zahniser, "High precision measurements of atmospheric nitrous oxide and methane using thermoelectrically cooled mid-infrared quantum cascade lasers and detectors," *Spectrochimica Acta Part A: Molecular and Biomolecular Spectroscopy*, vol. 60, pp. 3325–3335, Dec. 2004.

[38] M. R. McCurdy, Y. Bakhirkin, G. Wysocki, R. Lewicki, and F. K. Tittel, "Recent advances of laser-spectroscopy-based techniques for applications in breath analysis," *Journal of Breath Research*, vol. 1, p. 014001, Sept. 2007.

[39] C. Shimamoto, I. Hirata, and K. Katsu, "Breath and blood ammonia in liver cirrhosis," *Hepato-gastroenterology*, vol. 47, pp. 443–445, Apr. 2000. PMID: 10791209.

[40] J. Manne, O. Sukhorukov, W. Jger, and J. Tulip, "Pulsed quantum cascade laser-based cavity ring-down spectroscopy for ammonia detection in breath," *Applied Optics*, vol. 45, pp. 9230–9237, Dec. 2006.

[41] B. W. M. Moeskops, H. Naus, S. M. Cristescu, and F. J. M. Harren, "Quantum cascade laser-based carbon monoxide detection on a second time scale from human breath," *Applied Physics B*, vol. 82, pp. 649–654, Mar. 2006.

[42] S. Bartalini, P. Cancio, G. Giusfredi, D. Mazzotti, P. De Natale, S. Borri, I. Galli, T. Leveque, and L. Gianfrani, "Frequency-comb-referenced quantum-cascade laser at 4.4 μm," *Optics Letters*, vol. 32, pp. 988–990, Apr. 2007.

[43] A. A. Mills, D. Gatti, J. Jiang, C. Mohr, W. Mefford, L. Gianfrani, M. Fermann, I. Hartl, and M. Marangoni, "Coherent phase lock of a 9 μm quantum cascade laser to a 2 μm thulium optical frequency comb," *Opt. Lett.*, vol. 37, p. 40834085, Oct. 2012.

[44] I. Galli, S. Bartalini, S. Borri, P. Cancio, D. Mazzotti, P. De Natale, and G. Giusfredi, "Molecular gas sensing below parts per trillion: Radiocarbon-dioxide optical detection," *Physical Review Letters*, vol. 107, p. 270802, Dec. 2011.

[45] S. Blaser, D. Hofstetter, M. Beck, and J. Faist, "Free-space optical data link using peltier-cooled quantum cascade laser," *Electronics Letters*, vol. 37, no. 12, pp. 778–780, 2001.

[46] F. Capasso, R. Paiella, R. Martini, R. Colombelli, C. Gmachl, T. Myers, M. S. Taubman, R. Williams, C. Bethea, K. Unterrainer, H. Y. Hwang, D. L. Sivco, A. Y. Cho, A. Sergent, H. Liu, and E. A. Whittaker, "Quantum cascade lasers: ultrahigh-speed operation, optical wireless communication, narrow linewidth, and far-infrared emission," *IEEE Journal of Quantum Electronics*, vol. 38, no. 6, pp. 511–532, 2002.

[47] R. Martini, C. Gmachl, J. Falciglia, F. G. Curti, C. G. Bethea, F. Capasso, E. Whittaker, R. Paiella, A. Tredicucci, A. Hutchinson, D. Sivco, and A. Cho, "High-speed modulation and free-space optical audio/video transmission using quantum cascade lasers," *Electronics Letters*, vol. 37, no. 3, pp. 191–193, 2001.

[48] R. Martini and E. A. Whittaker, "Quantum cascade laser-based free space optical communications," *Journal of Optical and Fiber Communications Reports*, vol. 2, pp. 279–292, Oct. 2005.

[49] T. Okoshi, K. Kikuchi, and A. Nakayama, "Novel method for high resolution measurement of laser output spectrum," *Electronics Letters*, vol. 16, no. 16, pp. 630–631, 1980.

[50] T. L. Myers, R. M. Williams, M. S. Taubman, C. Gmachl, F. Capasso, D. L. Sivco, J. N. Baillargeon, and A. Y. Cho, "Free-running frequency stability of mid-infrared quantum cascade lasers," *Optics letters*, vol. 27, no. 3, p. 170172, 2002.

[51] S. Bartalini, S. Borri, P. Cancio, A. Castrillo, I. Galli, G. Giusfredi, D. Mazzotti, L. Gianfrani, and P. De Natale, "Observing the intrinsic linewidth of a quantum-cascade laser: Beyond the Schawlow-Townes limit," *Physical Review Letters*, vol. 104, Feb. 2010.

[52] L. Tombez, J. Di Francesco, S. Schilt, G. Di Domenico, J. Faist, P. Thomann, and D. Hofstetter, "Frequency noise of free-running 4.6 μm distributed feedback quantum cascade lasers near room temperature," *Optics Letters*, vol. 36, pp. 3109–3111, Aug. 2011.

[53] G. Galzerano, A. Gambetta, E. Fasci, A. Castrillo, M. Marangoni, P. Laporta, and L. Gianfrani, "Absolute frequency measurement of a water-stabilized diode laser at 1.384 μm by means of a fiber frequency comb," *Applied Physics B*, vol. 102, pp. 725–729, Mar. 2011.

[54] S. Schilt, N. Bucalovic, L. Tombez, V. Dolgovskiy, C. Schori, G. Di Domenico, M. Zaffalon, and P. Thomann, "Frequency discriminators for the characterization of narrow-spectrum heterodyne beat signals: application to the measurement of a sub-hertz carrier-envelope-offset beat in an optical frequency comb," *The Review of scientific instruments*, vol. 82, p. 123116, Dec. 2011. PMID: 22225208.

[55] A. L. Schawlow and C. H. Townes, "Infrared and optical masers," *Physical Review*, vol. 112, pp. 1940–1949, Dec. 1958.

[56] F. Riehle, *Frequency Standards: Basics and Applications*. Wiley, Mar. 2006.

[57] D. Meschede, *Optics, Light and Lasers: The Practical Approach to Modern Aspects of Photonics and Laser Physics*. John Wiley & Sons, June 2008.

[58] C. Henry, R. Logan, and K. Bertness, "Spectral dependence of the change in refractive index due to carrier injection in GaAs lasers," *Journal of Applied Physics*, vol. 52, no. 7, pp. 4457–4461, 1981.

[59] C. Henry, "Theory of the linewidth of semiconductor lasers," *IEEE Journal of Quantum Electronics*, vol. 18, no. 2, pp. 259–264, 1982.

[60] M. O'Mahony and I. Henning, "Semiconductor laser linewidth broadening due to 1/f carrier noise," *Electronics Letters*, vol. 19, no. 23, pp. 1000–1001, 1983.

[61] M.-C. Amann, R. Hakimi, B. Borchert, and S. Illek, "Linewidth broadening by 1/f noise in wavelength-tunable laser diodes," *Applied Physics Letters*, vol. 70, no. 12, pp. 1512–1514, 1997.

[62] D. S. Elliott, R. Roy, and S. J. Smith, "Extracavity laser band-shape and bandwidth modification," *Physical Review A*, vol. 26, pp. 12–18, July 1982.

[63] P. Gallion and G. Debarge, "Quantum phase noise and field correlation in single frequency semiconductor laser systems," *IEEE Journal of Quantum Electronics*, vol. 20, no. 4, pp. 343–349, 1984.

[64] L. B. Mercer, "1/f frequency noise effects on self-heterodyne linewidth measurements," *Journal of Lightwave Technology*, vol. 9, no. 4, pp. 485–493, 1991.

[65] G. M. Stephan, T. T. Tam, S. Blin, P. Besnard, and M. Tetu, "Laser line shape and spectral density of frequency noise," *Physical Review A*, vol. 71, p. 043809, Apr. 2005.

[66] G. Di Domenico, S. Schilt, and P. Thomann, "Simple approach to the relation between laser frequency noise and laser line shape," *Applied Optics*, vol. 49, pp. 4801–4807, Sept. 2010.

[67] N. Bucalovic, V. Dolgovskiy, C. Schori, P. Thomann, G. Di Domenico, and S. Schilt, "Experimental validation of a simple approximation to determine the linewidth of a laser from its frequency noise spectrum," *Applied Optics*, vol. 51, pp. 4582–4588, July 2012.

[68] J. B. Johnson, "The schottky effect in low frequency circuits," *Physical Review*, vol. 26, pp. 71–85, July 1925.

[69] J. B. Johnson, "Thermal agitation of electricity in conductors," *Physical Review*, vol. 32, pp. 97–109, July 1928.

[70] B. A. Taft, B. M. Hickey, C. Wunsch, and D. J. Baker Jr., "Equatorial undercurrent and deeper flows in the central pacific," *Deep Sea Research and Oceanographic Abstracts*, vol. 21, pp. 403–430, June 1974.

[71] C. Wunsch, "Bermuda sea level in relation to tides, weather, and baroclinic fluctuations," *Reviews of Geophysics*, vol. 10, no. 1, p. 149, 1972.

[72] W. H. Matthaeus and M. L. Goldstein, "Low-frequency 1/f noise in the interplanetary magnetic field," *Physical Review Letters*, vol. 57, pp. 495–498, July 1986.

[73] R. F. Voss and J. Clarke, "1/f noise in music and speech," *Nature*, vol. 258, pp. 317–318, Nov. 1975.

[74] R. F. Voss and J. Clarke, "1/f noise in music: Music from 1/f noise," *The Journal of the Acoustical Society of America*, vol. 63, pp. 258–263, Jan. 1978.

[75] J. E. Cutting, J. E. DeLong, and C. E. Nothelfer, "Attention and the evolution of hollywood film," *Psychological Science*, Feb. 2010. PMID: 20424081.

[76] M. Kobayashi and T. Musha, "1/f fluctuation of heartbeat period," *IEEE Transactions on Biomedical Engineering*, vol. BME-29, no. 6, pp. 456–457, 1982.

[77] E. Novikov, A. Novikov, D. Shannahoff-Khalsa, B. Schwartz, and J. Wright, "Scale-similar activity in the brain," *Physical Review E*, vol. 56, pp. R2387–R2389, Sept. 1997.

[78] K. Linkenkaer-Hansen, V. V. Nikouline, J. M. Palva, and R. J. Ilmoniemi, "Long-range temporal correlations and scaling behavior in human brain oscillations," *The Journal of Neuroscience*, vol. 21, pp. 1370–1377, Feb. 2001. PMID: 11160408.

[79] D. L. Gilden, T. Thornton, and M. W. Mallon, "1/f noise in human cognition," *Science*, vol. 267, pp. 1837–1839, Mar. 1995. PMID: 7892611.

[80] B. Pellegrini, R. Saletti, P. Terreni, and M. Prudenziati, "$1/f^{\gamma}$ noise in thick-film resistors as an effect of tunnel and thermally activated emissions, from measures versus frequency and temperature," *Physical Review B*, vol. 27, pp. 1233–1243, Jan. 1983.

[81] M. A. Caloyannides, "Microcycle spectral estimates of 1/f noise in semiconductors," *Journal of Applied Physics*, vol. 45, no. 1, pp. 307–316, 1974.

[82] W. H. Press, "Flicker noises in astronomy and elsewhere," *Comments on Astrophysics*, vol. 7, pp. 103–119, 1978.

[83] I. Flinn, "Extent of the 1/f noise spectrum," *Nature*, vol. 219, pp. 1356–1357, Sept. 1968.

[84] J. J. Brophy, "Variance fluctuations in flicker noise and current noise," *Journal of Applied Physics*, vol. 40, no. 9, pp. 3551–3553, 1969.

[85] R. F. Voss and J. Clarke, "Flicker (1/f) noise: Equilibrium temperature and resistance fluctuations," *Physical Review B*, vol. 13, pp. 556–573, Jan. 1976.

[86] F. N. Hooge and A. M. H. Hoppenbrouwers, "1/f noise in continuous thin gold films," *Physica*, vol. 45, pp. 386–392, Dec. 1969.

[87] J. W. Eberhard and P. M. Horn, "Temperature dependence of 1/f noise in silver and copper," *Physical Review Letters*, vol. 39, pp. 643–646, Sept. 1977.

[88] F. N. Hooge, T. G. M. Kleinpenning, and L. K. J. Vandamme, "Experimental studies on 1/f noise," *Reports on Progress in Physics*, vol. 44, p. 479, May 1981.

[89] A. L. McWhorter, "1/f noise and germanium surface properties," in *Semiconductor Surface Physics*, pp. 207–228, R. H. Kingston, University of Pennsylvania, Philadelphia, 1957.

[90] F. N. Hooge, "1/f noise is no surface effect," *Physics Letters A*, vol. 29, pp. 139–140, Apr. 1969.

[91] F. N. Hooge, "1/f noise sources," *IEEE Transactions on Electron Devices*, vol. 41, no. 11, pp. 1926–1935, 1994.

[92] K. Hung, P.-K. Ko, C. Hu, and Y. Cheng, "A unified model for the flicker noise in metal-oxide-semiconductor field-effect transistors," *IEEE Transactions on Electron Devices*, vol. 37, no. 3, pp. 654–665, 1990.

[93] L. Vandamme, X. Li, and D. Rigaud, "1/f noise in MOS devices, mobility or number fluctuations?," *IEEE Transactions on Electron Devices*, vol. 41, no. 11, pp. 1936–1945, 1994.

[94] G. Abowitz, E. Arnold, and E. Leventhal, "Surface states and 1/f noise in MOS transistors," *IEEE Transactions on Electron Devices*, vol. 14, no. 11, pp. 775–777, 1967.

[95] E. Milotti, "1/f noise: a pedagogical review," *arXiv:physics/0204033*, Apr. 2002.

[96] A. Balandin, S. V. Morozov, S. Cai, R. Li, K. Wang, G. Wijeratne, and C. Viswanathan, "Low flicker-noise GaN/AlGaN heterostructure field-effect transistors for microwave communications," *IEEE Transactions on Microwave Theory and Techniques*, vol. 47, no. 8, pp. 1413–1417, 1999.

[97] T. Roy, E. X. Zhang, Y. S. Puzyrev, X. Shen, D. M. Fleetwood, R. D. Schrimpf, G. Koblmueller, R. Chu, C. Poblenz, N. Fichtenbaum, C. S. Suh, U. K. Mishra, J. S. Speck, and S. T. Pantelides, "Temperature-dependence and microscopic origin of low frequency

1/f noise in GaN/AlGaN high electron mobility transistors," *Applied Physics Letters*, vol. 99, no. 20, p. 203501, 2011.

[98] G. Liu, S. Rumyantsev, M. S. Shur, and A. A. Balandin, "Origin of 1/f noise in graphene multilayers: Surface vs. volume," *Applied Physics Letters*, vol. 102, p. 093111, Mar. 2013.

[99] A. A. Balandin, "Low-frequency 1/f noise in graphene devices," *Nature Nanotechnology*, vol. 8, pp. 549–555, Aug. 2013.

[100] G. P. Agrawal, *Fiber-Optic Communication Systems*. John Wiley & Sons, Oct. 2010.

[101] X. Cui, C. Lengignon, W. Tao, W. Zhao, G. Wysocki, E. Fertein, C. Coeur, A. Cassez, L. Croize, W. Chen, Y. Wang, W. Zhang, X. Gao, W. Liu, Y. Zhang, and F. Dong, "Photonic sensing of the atmosphere by absorption spectroscopy," *Journal of Quantitative Spectroscopy and Radiative Transfer*, vol. 113, pp. 1300–1316, July 2012.

[102] F. Cappelli, I. Galli, S. Borri, G. Giusfredi, P. Cancio, D. Mazzotti, A. Montori, N. Akikusa, M. Yamanishi, and S. Bartalini, "Sub-kilohertz linewidth room-temperature mid-infrared quantum cascade laser using a molecular sub-Doppler reference," *Optics letters*, vol. 37, no. 23, p. 48114813, 2012.

[103] M. S. Vitiello, T. Gresch, A. Lops, V. Spagnolo, G. Scamarcio, N. Hoyler, M. Giovannini, and J. Faist, "Influence of InAs, AlAs delta layers on the optical, electronic, and thermal characteristics of strain-compensated GaInAs/AlInAs quantum-cascade lasers," *Applied Physics Letters*, vol. 91, p. 161111, Oct. 2007.

[104] A. Lops, V. Spagnolo, and G. Scamarcio, "Thermal modeling of GaInAs/AlInAs quantum cascade lasers," *Journal of Applied Physics*, vol. 100, p. 043109, Aug. 2006.

[105] C. Evans, V. Jovanovic, D. Indjin, Z. Ikonic, and P. Harrison, "Investigation of thermal effects in quantum-cascade lasers," *IEEE Journal of Quantum Electronics*, vol. 42, no. 9, pp. 859–867, 2006.

[106] J. M. Supplee, E. A. Whittaker, and W. Lenth, "Theoretical description of frequency modulation and wavelength modulation spectroscopy," *Applied Optics*, vol. 33, pp. 6294–6302, Sept. 1994.

[107] S. Kobayashi, Y. Yamamoto, M. Ito, and T. Kimura, "Direct frequency modulation in AlGaAs semiconductor lasers," *IEEE Journal of Quantum Electronics*, vol. 18, no. 4, pp. 582–595, 1982.

[108] G. Jacobsen, H. Olesen, F. Birkedahl, and B. Tromborg, "Current/frequency-modulation characteristics for directly optical frequency-modulated injection lasers at 830 nm and 1.3 μm," *Electronics Letters*, vol. 18, no. 20, p. 874, 1982.

[109] S. Yamazaki, K. Emura, M. Shikada, M. Yamaguchi, and I. Mito, "Realisation of flat FM response by directly modulating a phase tunable DFB laser diode," *Electronics Letters*, vol. 21, no. 7, p. 283, 1985.

[110] S. Murata, I. Mito, and K. Kobayashi, "Frequency modulation and spectral characteristics for a 1.5 μm phase-tunable DFB laser," *Electronics Letters*, vol. 23, no. 1, pp. 12–14, 1987.

[111] R. Schimpe, J. Bowers, and T. Koch, "Characterisation of frequency response of 1.5 um InGaAsP DFB laser diode and InGaAs PIN photodiode by heterodyne measurement technique," *Electronics Letters*, vol. 22, no. 9, pp. 453–454, 1986.

[112] T. Koch and J. Bowers, "Nature of wavelength chirping in directly modulated semiconductor lasers," *Electronics Letters*, vol. 20, no. 25, pp. 1038–1040, 1984.

[113] J. Buus, *Single Frequency Semiconductor Lasers*. SPIE Press, Jan. 1991.

[114] V. S. Vavilov, "Handbook on the physical properties of Ge, Si, GaAs and InP," *Physics-Uspekhi*, vol. 39, p. 757, July 1996.

[115] G. Clark, L. O. Heflinger, and C. Roychoudhuri, "Dynamic wavelength tuning of single-mode GaAlAs lasers," *IEEE Journal of Quantum Electronics*, vol. 18, no. 2, pp. 199–204, 1982.

[116] K. Petermann, *Laser Diode Modulation and Noise*. Springer, Jan. 1991.

[117] S. Adachi, *Physical Properties of III-V Semiconductor Compounds*. John Wiley & Sons, Nov. 1992.

[118] Y. Yoshikuni and G. Motosugi, "Multielectrode distributed feedback laser for pure frequency modulation and chirping suppressed amplitude modulation," *Journal of Lightwave Technology*, vol. 5, no. 4, pp. 516–522, 1987.

[119] S. Ogita, Y. Kotaki, M. Matsuda, Y. Kuwahara, H. Onaka, H. Miyata, and H. Ishikawa, "FM response of narrow-linewidth, multielectrode $\lambda/4$ shift DFB laser," *IEEE Photonics Technology Letters*, vol. 2, no. 3, pp. 165–166, 1990.

[120] T. Aellen, R. Maulini, R. Terazzi, N. Hoyler, M. Giovannini, J. Faist, S. Blaser, and L. Hvozdara, "Direct measurement of the linewidth enhancement factor by optical heterodyning of an amplitude-modulated quantum cascade laser," *Applied Physics Letters*, vol. 89, no. 9, pp. 091121–091121–3, 2006.

[121] J. v. Staden, T. Gensty, W. Elser, G. Giuliani, and C. Mann, "Measurements of the alpha factor of a distributed-feedback quantum cascade laser by an optical feedback self-mixing technique," *Opt. Lett.*, vol. 31, p. 25742576, Sept. 2006.

[122] R. Paiella, R. Martini, F. Capasso, C. Gmachl, H. Y. Hwang, D. L. Sivco, J. N. Baillargeon, A. Y. Cho, E. A. Whittaker, and H. C. Liu, "High-frequency modulation without the relaxation oscillation resonance in quantum cascade lasers," *Applied Physics Letters*, vol. 79, p. 2526, Oct. 2001.

[123] M. Imai and K. Kawakita, "Measurement of direct frequency modulation characteristics of laser diodes by Michelson interferometry," *Applied Optics*, vol. 29, pp. 348–353, Jan. 1990.

[124] S. Bartalini, S. Borri, I. Galli, G. Giusfredi, D. Mazzotti, T. Edamura, N. Akikusa, M. Yamanishi, and P. De Natale, "Measuring frequency noise and intrinsic linewidth of a room-temperature DFB quantum cascade laser," *Optics Express*, vol. 19, pp. 17996–18003, Sept. 2011.

[125] M. S. Vitiello, L. Consolino, S. Bartalini, A. Taschin, A. Tredicucci, M. Inguscio, and P. De Natale, "Quantum-limited frequency fluctuations in a terahertz laser," *Nature Photonics*, vol. 6, pp. 525–528, Aug. 2012.

[126] S. Borri, S. Bartalini, P. C. Pastor, I. Galli, G. Giusfredi, D. Mazzotti, M. Yamanishi, and P. De Natale, "Frequency-noise dynamics

of mid-infrared quantum cascade lasers," *IEEE Journal of Quantum Electronics*, vol. 47, p. 984988, July 2011.

[127] M. S. Vitiello, G. Scamarcio, and V. Spagnolo, "Time-resolved measurement of the local lattice temperature in terahertz quantum cascade lasers," *Applied Physics Letters*, vol. 92, p. 101116, Mar. 2008.

[128] S. Huxtable, A. Shakouri, P. Abraham, Y.-J. Chiu, X. Fan, J. Bowers, and A. Majumdar, "Thermal conductivity of indium phosphide based superlattices," in *Eighteenth International Conference on Thermoelectrics, 1999*, pp. 594–597, 1999.

[129] S. Borri, S. Bartalini, P. D. Natale, M. Inguscio, C. Gmachl, F. Capasso, D. L. Sivco, and A. Y. Cho, "Frequency modulation spectroscopy by means of quantum-cascade lasers," *Applied Physics B*, vol. 85, pp. 223–229, Nov. 2006.

[130] K. Libbrecht and J. Hall, "A low-noise high-speed diode laser current controller," *Review of Scientific Instruments*, vol. 64, no. 8, pp. 2133–2135, 1993.

[131] C. J. Erickson, M. V. Zijll, G. Doermann, and D. S. Durfee, "An ultrahigh stability, low-noise laser current driver with digital control," *Review of Scientific Instruments*, vol. 79, p. 073107, July 2008.

[132] M. S. Taubman, "Low-noise high-performance current controllers for quantum cascade lasers," *Review of Scientific Instruments*, vol. 82, no. 6, p. 064704064704, 2011.

[133] L. Rothman, I. Gordon, A. Barbe, D. Benner, P. Bernath, M. Birk, V. Boudon, L. Brown, A. Campargue, J.-P. Champion, K. Chance, L. Coudert, V. Dana, V. Devi, S. Fally, J.-M. Flaud, R. Gamache, A. Goldman, D. Jacquemart, I. Kleiner, N. Lacome, W. Lafferty, J.-Y. Mandin, S. Massie, S. Mikhailenko, C. Miller, N. Moazzen-Ahmadi, O. Naumenko, A. Nikitin, J. Orphal, V. Perevalov, A. Perrin, A. Predoi-Cross, C. Rinsland, M. Rotger, M. imekov, M. Smith, K. Sung, S. Tashkun, J. Tennyson, R. Toth, A. Vandaele, and J. Vander Auwera, "The HITRAN 2008 molecular spectroscopic database," *Journal of Quantitative Spectroscopy and Radiative Transfer*, vol. 110, pp. 533–572, June 2009.

[134] E. Whiting, "An empirical approximation to the Voigt profile," *Journal of Quantitative Spectroscopy and Radiative Transfer*, vol. 8, pp. 1379–1384, June 1968.

[135] M. Osinski and J. Buus, "Linewidth broadening factor in semiconductor lasers: An overview," *IEEE Journal of Quantum Electronics*, vol. 23, no. 1, pp. 9–29, 1987.

[136] M. Yamanishi, T. Edamura, K. Fujita, N. Akikusa, and H. Kan, "Theory of the intrinsic linewidth of quantum-cascade lasers: Hidden reason for the narrow linewidth and line-broadening by thermal photons," *IEEE Journal of Quantum Electronics*, vol. 44, no. 1, pp. 12–29, 2008.

[137] A. Wittmann, Y. Bonetti, M. Fischer, J. Faist, S. Blaser, and E. Gini, "Distributed-feedback quantum-cascade lasers at 9 μm operating in continuous wave up to 423 K," *IEEE Photonics Technology Letters*, vol. 21, no. 12, pp. 814–816, 2009.

[138] L. Tombez, S. Schilt, J. Di Francesco, P. Thomann, and D. Hofstetter, "Temperature dependence of the frequency noise in a mid-IR DFB quantum cascade laser from cryogenic to room temperature," *Optics Express*, vol. 20, pp. 6851–6859, Mar. 2012.

[139] K. Knabe, P. A. Williams, F. R. Giorgetta, C. M. Armacost, S. Crivello, M. B. Radunsky, and N. R. Newbury, "Frequency characterization of a swept- and fixed-wavelength external-cavity quantum cascade laser by use of a frequency comb," *Optics Express*, vol. 20, pp. 12432–12442, May 2012. PMID: 22714230.

[140] K. Knabe, P. A. Williams, F. R. Giorgetta, C. M. Armacost, M. B. Radunsky, and N. R. Newbury, "Frequency characterization of an external-cavity quantum cascade laser at 4.5 μm using a frequency comb," in *Laser Applications to Chemical, Security and Environmental Analysis*, 2012.

[141] K. Kikuchi and T. Okoshi, "Dependence of semiconductor laser linewidth on measurement time: evidence of predominance of 1/f noise," *Electronics Letters*, vol. 21, no. 22, p. 1011, 1985.

[142] L. Westbrook, I. D. Henning, A. Nelson, and P. Fiddyment, "Spectral properties of strongly coupled 1.5 μm DFB laser diodes," *IEEE Journal of Quantum Electronics*, vol. 21, no. 6, pp. 512–518, 1985.

[143] D. Welford and A. Mooradian, "Output power and temperature dependence of the linewidth of single-frequency cw (GaAl)As diode lasers," *Applied Physics Letters*, vol. 40, no. 10, pp. 865–867, 1982.

[144] K. Kojima, K. Kyuma, and T. Nakayama, "Analysis of the spectral linewidth of distributed feedback laser diodes," *Journal of Lightwave Technology*, vol. 3, no. 5, pp. 1048–1055, 1985.

[145] R. Tkach and A. Chraplyvy, "Phase noise and linewidth in an InGaAsP DFB laser," *Journal of Lightwave Technology*, vol. 4, no. 11, pp. 1711–1716, 1986.

[146] Y. Kotaki, S. Ogita, M. Matsuda, Y. Kuwahara, and H. Ishikawa, "Tunable, narrow-linewidth and high-power $\lambda/4$-shifted DFB laser," *Electronics Letters*, vol. 25, no. 15, p. 990, 1989.

[147] S. Takano, T. Sasaki, H. Yamada, M. Kitamura, and I. Mito, "Sub-MHz spectral linewidth in 1.5 μm separate-confinement-heterostructure (SCH) quantum-well DFB LDs," *Electronics Letters*, vol. 25, no. 5, pp. 356–357, 1989.

[148] K. Uomi, S. Sasaki, T. Tsuchiya, M. Okai, M. Aoki, and N. Chinone, "Spectral linewidth reduction by low spatial hole burning in 1.5 μm multi-quantum-well $\lambda/4$-shifted DFB lasers," *Electronics Letters*, vol. 26, no. 1, p. 52, 1990.

[149] F. Kano, Y. Tohmori, Y. Kondo, M. Nakao, M. Fukuda, and K. Oe, "Spectral linewidth reduction (580 kHz) in structure-optimised 1.5 μm butt-jointed distributed bragg reflector lasers," *Electronics Letters*, vol. 25, no. 11, pp. 709–710, 1989.

[150] P. Doussiere, C.-L. Shieh, S. DeMars, and K. Dzurko, "Very high power 1310nm InP single mode distributed feed back laser diode with reduced linewidth," in *Proc. SPIE 6485*, vol. 6485, (San Jose, CA), pp. 64850G–64850G–8, 2007.

[151] S. Spiessberger, M. Schiemangk, A. Wicht, H. Wenzel, O. Brox, and G. Erbert, "Narrow linewidth DFB lasers emitting near a wavelength of 1064 nm," *Journal of Lightwave Technology*, vol. 28, no. 17, pp. 2611–2616, 2010.

[152] K. Paschke, S. Spieberger, C. Kaspari, D. Feise, C. Fiebig, G. Blume, H. Wenzel, A. Wicht, and G. Erbert, "High-power distributed bragg reflector ridge-waveguide diode laser with very small spectral linewidth," *Optics Letters*, vol. 35, pp. 402–404, Feb. 2010.

[153] A. Dandridge and H. Taylor, "Correlation of low-frequency intensity and frequency fluctuations in GaAlAs lasers," *IEEE Transactions on*

Microwave Theory and Techniques, vol. 30, no. 10, pp. 1726–1738, 1982.

[154] K. Kikuchi and T. Okoshi, "Measurement of spectra of and correlation between FM and AM noises in GaAlAs lasers," *Electronics Letters*, vol. 19, no. 20, p. 812, 1983.

[155] K. Kikuchi and T. Okoshi, "Estimation of linewidth enhancement factor of AlGaAs lasers by correlation measurement between FM and AM noises," *IEEE Journal of Quantum Electronics*, vol. 21, no. 6, pp. 669–673, 1985.

[156] E. Goobar, A. Karlsson, and S. Machida, "Measurements and theory of correlation between terminal electric noise and optical noise in a two-section semiconductor laser," *IEEE Journal of Quantum Electronics*, vol. 29, no. 2, pp. 386–395, 1993.

[157] J. Reid, D. T. Cassidy, and R. T. Menzies, "Linewidth measurements of tunable diode lasers using heterodyne and etalon techniques," *Applied Optics*, vol. 21, pp. 3961–3965, Nov. 1982.

[158] S. Lundqvist, J. Margolis, and J. Reid, "Measurements of pressure-broadening coefficients of NO and O3 using a computerized tunable diode laser spectrometer," *Applied Optics*, vol. 21, pp. 3109–3113, Sept. 1982.

[159] D. E. Jennings, "Calibration of diode laser spectra using a confocal etalon," *Applied Optics*, vol. 23, pp. 1299–1301, May 1984.

[160] D. E. Jennings and J. J. Hillman, "Shock isolator for diode laser operation on a closed cycle refrigerator," *Review of Scientific Instruments*, vol. 48, no. 12, pp. 1568–1569, 1977.

[161] R. L. Sams and A. Fried, "Microphone triggering circuit for elimination of mechanically induced frequency-jitter in diode laser spectrometers: implications for quantitative analysis," *Applied optics*, vol. 26, pp. 3552–3558, Sept. 1987. PMID: 20490102.

[162] W. Liang, V. S. Ilchenko, A. A. Savchenkov, A. B. Matsko, D. Seidel, and L. Maleki, "Whispering-gallery-mode-resonator-based ultranarrow linewidth external-cavity semiconductor laser," *Optics Letters*, vol. 35, pp. 2822–2824, Aug. 2010.

[163] K. Numata, J. Camp, M. A. Krainak, and L. Stolpner, "Performance of planar-waveguide external cavity laser for precision measurements," *Optics Express*, vol. 18, pp. 22781–22788, Oct. 2010.

[164] L. Tombez, S. Schilt, J. D. Francesco, T. Fhrer, B. Rein, T. Walther, G. D. Domenico, D. Hofstetter, and P. Thomann, "Linewidth of a quantum-cascade laser assessed from its frequency noise spectrum and impact of the current driver," *Applied Physics B*, vol. 109, pp. 407–414, Nov. 2012.

[165] P. Bloomfield, *Fourier Analysis of Time Series: An Introduction*. John Wiley & Sons, Apr. 2004.

[166] H. H. Gttler and J. H. Werner, "Influence of barrier inhomogeneities on noise at Schottky contacts," *Applied Physics Letters*, vol. 56, pp. 1113–1115, Mar. 1990.

[167] S.-H. Ng and C. Surya, "Studies of flicker noise in In0.53Ga0.47As/AlAs/InAs resonant tunneling diodes," *Solid-State Electronics*, vol. 35, pp. 1213–1216, Sept. 1992.

[168] S. Ng and C. Surya, "Theory and experiments on flicker noise in In0.53Ga0.47As/AlAs/InAs resonant tunneling diodes," *Journal of Applied Physics*, vol. 73, no. 11, pp. 7504–7508, 1993.

[169] S. Ng, C. Surya, E. Brown, and P. A. Maki, "Observation of random telegraph noise in resonant tunneling diodes," *Applied Physics Letters*, vol. 62, no. 18, pp. 2262–2264, 1993.

[170] X. Chen and M. Leys, "Study of 1/f noise in InP grown by CBE," *Solid-State Electronics*, vol. 39, pp. 1149–1153, Aug. 1996.

[171] X. Chen, M. Leys, and F. Ragay, "Low frequency noise in p+-GaAs with non-alloyed contacts," *Electronics Letters*, vol. 30, no. 7, pp. 600–601, 1994.

[172] M. S. Taubman, T. L. Myers, B. D. Cannon, R. M. Williams, F. Capasso, C. Gmachl, D. L. Sivco, and A. Y. Cho, "Frequency stabilization of quantum-cascade lasers by use of optical cavities," *Optics Letters*, vol. 27, pp. 2164–2166, Dec. 2002.

[173] R. M. Williams, J. F. Kelly, J. S. Hartman, S. W. Sharpe, M. S. Taubman, J. L. Hall, F. Capasso, C. Gmachl, D. L. Sivco, J. N.

Baillargeon, and A. Y. Cho, "Kilohertz linewidth from frequency-stabilized mid-infrared quantum cascade lasers," *Optics Letters*, vol. 24, pp. 1844–1846, Dec. 1999.

[174] I. Galli, M. Siciliani de Cumis, F. Cappelli, S. Bartalini, D. Mazzotti, S. Borri, A. Montori, N. Akikusa, M. Yamanishi, G. Giusfredi, P. Cancio, and P. De Natale, "Comb-assisted subkilohertz linewidth quantum cascade laser for high-precision mid-infrared spectroscopy," *Applied Physics Letters*, vol. 102, pp. 121117–121117–4, Mar. 2013.

[175] F. Bielsa, A. Douillet, T. Valenzuela, J.-P. Karr, and L. Hilico, "Narrow-line phase-locked quantum cascade laser in the 9.2 μm range," *Opt. Lett.*, vol. 32, p. 16411643, June 2007.

[176] S. Borri, I. Galli, F. Cappelli, A. Bismuto, S. Bartalini, P. Cancio, G. Giusfredi, D. Mazzotti, J. Faist, and P. De Natale, "Direct link of a mid-infrared QCL to a frequency comb by optical injection," *Optics Letters*, vol. 37, pp. 1011–1013, Mar. 2012.

[177] R. M. Williams, J. F. Kelly, J. S. Hartman, S. W. Sharpe, M. S. Taubman, J. L. Hall, F. Capasso, C. Gmachl, D. L. Sivco, J. N. Baillargeon, and A. Y. Cho, "Kilohertz linewidth from frequency-stabilized mid-infrared quantum cascade lasers," *Optics Letters*, vol. 24, pp. 1844–1846, Dec. 1999.

[178] S. M. Foreman, A. Marian, J. Ye, E. A. Petrukhin, M. A. Gubin, O. D. Mucke, F. N. C. Wong, E. P. Ippen, and F. X. Kartner, "Demonstration of a HeNe/CH4-based optical molecular clock," *Optics Letters*, vol. 30, pp. 570–572, Mar. 2005.

[179] B. Chanteau, O. Lopez, W. Zhang, D. Nicolodi, B. Argence, F. Auguste, M. Abgrall, C. Chardonnet, G. Santarelli, B. Darqui, Y. L. Coq, and A. Amy-Klein, "Mid-infrared laser phase-locking to a remote near-infrared frequency reference for high-precision molecular spectroscopy," *New Journal of Physics*, vol. 15, p. 073003, July 2013.

[180] G. Chen, C. Bethea, R. Martini, P. Grant, R. Dudek, and H. Liu, "High-speed all-optical modulation of a standard quantum cascade laser by front facet illumination," *Applied Physics Letters*, vol. 95, no. 10, pp. 101104–101104–3, 2009.

[181] G. Chen, R. Martini, S. Park, C. G. Bethea, I.-C. A. Chen, P. D. Grant, R. Dudek, and H. C. Liu, "Optically induced fast wavelength

modulation in a quantum cascade laser," *Applied Physics Letters*, vol. 97, p. 011102, July 2010.

[182] S. Woodward, U. Koren, B. Miller, M. Young, M. Newkirk, and C. Burrus, "A DBR laser tunable by resistive heating," *IEEE Photonics Technology Letters*, vol. 4, no. 12, pp. 1330–1332, 1992.

[183] J. Teissier, S. Laurent, C. Manquest, C. Sirtori, A. Bousseksou, J. R. Coudevylle, R. Colombelli, G. Beaudoin, and I. Sagnes, "Electrical modulation of the complex refractive index in mid-infrared quantum cascade lasers," *Optics Express*, vol. 20, p. 1172, Jan. 2012.

Remerciements

Je tiens à dédier des remerciements à différentes personnes ayant eu une implication directe ou indirecte et à différents degrés d'importance dans l'accomplissement de cette thèse de doctorat.

Mes premiers mots vont au Prof. Pierre Thomann, pour m'avoir donné l'opportunité de rejoindre le Laboratoire Temps-Fréquence afin d'y mener mon travail de doctorat.

Au même titre, je tiens à adresser mes plus sincères remerciements au Prof. Thomas Südmeyer pour avoir dirigé cette thèse et grandement contribué, de par son ouverture d'esprit, ses idées, sa passion pour la science et sa confiance, aux divers succès liés à ce travail ainsi qu'à mes aspirations futures.

Ce travail n'aurait sans doute pas sa forme actuelle sans le support et le dévouement de Stéphane Schilt, qui a toujours montré une attitude positive vis-à-vis de ce sujet de recherche et a su en tirer un maximum afin de le valoriser de la meilleure des manières.

Je ne saurais oublier Daniel Hofstetter, avec qui, les premiers résultats importants ont été obtenus. Sa connaissance et son expérience de la physique des semiconducteurs ont été d'une aide précieuse et indispensable. Je profite également de saluer l'aide très appréciée et de grande qualité fournie par Joab Di Francesco au début de ce travail.

Merci au Prof. Jérôme Faist et à Saverio Bartalini d'avoir accepté de faire partie du jury d'examen, pour leurs commentaires avisés, ainsi que pour l'intérêt porté à ce travail au travers de collaborations et discussions fructueuses qui ont participé à sa réussite.

Ces années passées au Laboratoire Temps-Fréquence n'auraient eu la même saveur sans l'ambiance agréable toujours maintenue par les nombreuses personnes que j'ai eu la chance de côtoyer: Danijela, Thejesh,

Mathieu, Florian, Renaud, Christoph, Gaetano, Alexander, Gianni, Christian, Kutan, Loic, Sargis, Clément, Clara, Bertrand, Martin, Maxim et Michael. Une pensée particulière va aux anciens locataires du bureau D17: Laurent, Nikola et Vladimir. Bonne chance aux nouveaux !

Il me tient également à coeur de relever l'importance de l'aide administrative fournie par Muriel Vallery d'une part, ainsi que son dévouement à maintenir une ambiance conviviale au sein du laboratoire. Merci également à Sandrine Gouinguené, notamment pour son aide précieuse de dernière minute.

Les choses auraient pu être bien compliquées sans l'aide experte et de grande qualité des techniciens et ingénieurs du Laboratoire Temps-Fréquence et des services techniques de l'Université: Christian Heche, Dominique Schenker, Thierry Delhove, Isidro Fernandez, André Cornu, Patrick Scherler et Marc Durrenberger. Je tiens à dédier un remerciement particulier à Daniel Varidel, qui ne s'est jamais découragé face aux nombreux circuit électroniques grillés, qu'il a toujours rapidement remplacés avec le sourire.

La possibilité de collaborer avec la société Alpes Lasers SA fût une chance particulière, et je tiens à remercier notamment Michel Rochat et Romain Terazzi pour les discussions toujours constructives. Je suis également particulièrement reconnaissant envers Stéphane Blaser pour ses explications expertes et les réponses qu'il a apportées à mes nombreuses questions.

Je ne saurais terminer sans exprimer ma reconnaissance à ma famille pour le cadre extrêmement favorable dont j'ai pu bénéficier, mes amis, Cosette, qui m'a toujours porté -et surtout supporté-, ainsi que toutes les personnes qui m'ont de près ou de loin convaincu et soutenu dans mes choix.

Une dernière pensée ira aux absents, dont la reconnaissance et la fierté seront toujours une source inépuisable de motivation.